Studies on Suppression of Competitive Hydrogen Evolution Reaction during Electrochemical Reduction of Carbon Dioxide

Yuxin Wu

September, 2021

Studies on Suppression of Competitive Hydrogen Evolution Reaction during Electrochemical Reduction of Carbon Dioxide

A dissertation submitted to

The Graduate School of Engineering Science

Osaka University

in partial fulfillment of the requirement for the degree of

Doctor of Philosophy in Science

BY

Yuxin Wu

September, 2021

Abstract

For the serious problem of excessive CO_2 emission, using CO_2 as an alternative carbon feedstock and transferring it to other valuable chemicals has been regarded as a prospective way. Among various methodologies for effectively reducing CO_2 emissions, the electrochemical CO_2 reduction reaction (CO_2RR) has attracted intensive attention because a high rate of CO_2 conversion is expected even at ambient temperature and pressure. Under common aqueous conditions, the hydrogen evolution reaction (HER) is inevitable, limiting efficiency and narrowing the applying condition of CO_2 reduction. There are two major methods to suppress the hydrogen evolution via changing the CO_2 transfer from liquid phase feed to gas phase or controllable synthesis of desirable catalysts with high densities of exposed active sites or crystal facet. In this thesis, we focused on the two methods carrying much effort to increase CO_2 reduction efficiency under a broader environment. In Chapter I, we comprehensively introduced the fundamental background and current research emphasis of CO_2 reduction, including catalyst modification and the application of gas diffusion electrode, and the meaning of our work in this field.

We introduced the gas diffusion electrode on CO_2 reduction field with a broader application range. Nickle-doped covalent triazine framework showed exceeding 60% CO faradic efficiency not only in alkaline or neutral electrolyte, but also in acidic condition even the pH is 2 by introduction of gas diffusion electrode (GDE) based electrolyzer. However, when using the plate electrode (PE) based cell, the FEs of CO exhibited only around 1.2% in the electrolyte with the same pH. To clarify the reason, we added the Zn (II) ions in the electrolyte to verify the local pH

change during the reduction process, which would precipitate on the electrode if the local pH increases to alkaline condition even the bulk pH is 2. The sediment was just founded on the surface of GDE, not on the PE, which confirmed our assumption, and the expansion of pH range is beneficial for considering secondary uses of CO_2RR products.

In Chapter III, we introduced the atomic Sn modification on Cu nanoparticles as the catalysts for CO_2 reduction. Low-coordinated Cu sites are likely active for the competing HER during CO_2 electrolysis. To hinder such low-coordinated Cu sites, we decorated Sn atoms with varied ratios, which is a kind of inert metal atom, in Cu nanoparticles via a simple wet-chemical method. Physical and theoretical characterization revealed that Sn atoms were preferentially located at low-coordinated sites when Sn is in low contents (below 1.5%). Compared with the pristine Cu catalyst, the Sn-modified Cu exhibited suppression of the hydrogen evolution and acceleration of CO evolution. After Sn atomic modification, the catalysts showed lower activity both for hydrogen evolution and CO_2 reduction via the first principle calculation target the adsorption strength of reaction intermediates. As a result, the activity of coordinatively-saturated Cu sites, which show favorable CO_2 reduction activity, was emphasized. The modification of trace foreign metals in metal nanoparticles may provide an avenue for the synthesis of selective electrocatalysts targeting various reactions.

Chapter IV introduced the direct electrodeposition of metal catalysts on gas diffusion electrodes. Direct electrodeposition on GDE surface shows many merits compared with the dip-coating of as-prepared catalyst powders on GDE, such as, the better uniformity, the controllable fabrication of specific exposed active site or crystal

facet, and the possibility of porous structure with more channels for reactants delivery. In this chapter, we successfully deposited porous Cu and Zn layers directed on GDE surface via adding different surfactants in the electrolyte and applying pulse current. The electrodeposited samples showed a much higher current density compared with the dip-coating samples. We also optimized the concentration of added surfactant and the program of pulse current method to modulate specific crystal facets with favorable activity toward CO_2RR compared with HER. The direct electrodeposition method is beneficial to regulating the structure and fabricating larger electrodes, which show much potential in scale-up industrial application.

In this paper, we focused on the suppression of hydrogen evolution during CO_2 electrolysis process and found several effective strategies, including changing the CO_2 transfer media from liquid to gas phase by introducing gas diffusion electrode, controllably preparing specific catalysts with suppression of HER-active sites or increment of favorable CO_2 reduction active sites, which expand the vision of the CO_2 reduction in practical application.

Contents

Chapter I General Introduction

Excessive emissions of carbon dioxide (CO_2) due to fossil fuel combustion and industry is becoming a serious obstacle to the sustainable development of society and the main reason for global warming. However, CO_2 is also an essential trace gas in Earth's atmosphere, which participates in the global carbon cycle with various plants, animals and microorganisms.[1] Based on above consideration, using CO_2 as an alternative carbon feedstock and transferring it to other valuable chemicals, which could create an artificial close carbon cycle, shows great potential of current research.[2-4] Up to now, many approaches, such as photochemical, thermochemical, electrochemical, and biological methods, have been devoted to the research of CO_2 reduction reaction (CO_2RR). Among above means, electroreduction of CO_2, which could power by other sustainable energy, such as nuclear, wind, solar and hydro energy,[5, 6] has been regarded as the most promising one with several merits over other competitors, including zero-emission, potential to high current and large-scale, product with high-value, wide range of electrolyzer design, as well as rational control of reaction process.[7, 8]

Despite current research had achieved many breakthroughs in elevated current density, extended catalyst range, and high-selectivity of sole product, the practical application of electrocatalytic CO_2RR is still in its infancy stage with many challenges.[9] First of all, the primary supply method of CO_2 in existent work is the soluble CO_2 in aqueous condition, with inevitable side reaction of hydrogen evolution and limited transfer rate due to the low solubility of CO_2 (~ 0.033M). In order to confine the rate of hydrogen evolution reaction (HER), the overwhelming majority of

CO_2 reduction are restricted in neutral or alkaline solutions with a lower concentration of protons. Furthermore, the current density range of several or dozens of milliampere per square centimeter (mA cm^{-2}) is urgent to increase to face the requirements for the scale-up production.

Besides the electrolyzer and system design, the catalyst itself also plays a vital role in the performance of CO_2RR process.[10] Many kinds of catalysts, including metals, metal compounds, carbonaceous materials and organics, have been devoted to the research of CO_2RR. One of a present hotspot is the atomic distribution of active metal centers on a supporting framework as substrate, which vastly increases the utilization efficiency of metal species and avoids some side reaction. Along with the single-atom catalysts, many factors of metallic catalysts also influence the performance of CO_2RR, such as the oxidative state, crystal orientation, morphology, particle size and alloying or hybrids with other metals, via modulation of the adsorption energy between active sites and the intermediates during reaction pathways.

Beyond these considerations, in this chapter, we introduce the background of electrocatalytic CO_2RR, including the fundamental mechanism and research method, major catalyst genres, and the optimized method to gain high efficiency and current density for CO_2RR in both catalysts modification and electrolyzer system upgrading field.

1.1. Electrocatalytic CO_2 reduction

1.1.1 Fundamental mechanism of CO_2 reduction

Electrochemical reduction of CO_2 is a multiple proton-electron assisted transfer process,[11, 12] which often occurs on the interface between electrode and electrolyte, and commonly could be simply divided into four stages:[6, 12] (1) the chemical adsorption of CO_2 molecule on the surface of electrode, (2) the activation of CO_2 molecule to the $CO_2^{\bullet-}$ radical, (3) multiple electron- or proton- associated transfer process to gain various products, and (4) products desorb from electrode surface and diffuse into electrolyte. The CO_2 activation is hard to drive due to the inert property of CO_2 molecule. As an endothermic process, CO_2 activation (equation (1-1)) requires a very negative potential (-1.9 V versus standard hydrogen electrode (SHE)) to form the $CO_2^{\bullet-}$ radical under equilibrium status.

$$CO_2 + e^- \rightarrow CO_2^{\bullet-} \qquad E_0 = -1.90\ V \tag{1-1}$$

In actual condition, it desires much more negative to startup compared to the ideal one, so an external bias is necessary on most occasions. However, the suitable catalysts, which could stabilize radicals via forming chemical bonds, exhibit a decreased redox potential.

Based on the number of transferred electrons involved in the reaction, the possible products including two-electron of carbon monoxide (CO) and formate ($HCOO^-$), 4-electron of formaldehyde (HCHO), 6-electron of methanol (CH_3OH), 8-electron of methane (CH_4), 12-electron of ethanol (CH_3CH_2OH) and ethylene (C_2H_4) and much more complex products. The half-reaction mentioned above, as well as the hydrogen evolution reaction, required equilibrium potentials from thermodynamic

aspect have been listed as below[13-15] (under the standard condition: 1 atmosphere pressure, 25 ℃, pH = 7, 1 M concentration, potential versus SHE):

$$CO_2 + 2H^+ + 2e^- \rightarrow CO \quad E_0 = -0.52\,V \tag{1-2}$$

$$CO_2 + 2H^+ + 2e^- \rightarrow HCOOH \quad E_0 = -0.61\,V \tag{1-3}$$

$$CO_2 + 4H^+ + 4e^- \rightarrow HCHO \quad E_0 = -0.51\,V \tag{1-4}$$

$$CO_2 + 6H^+ + 6e^- \rightarrow CH_3OH + H_2O \quad E_0 = -0.38\,V \tag{1-5}$$

$$CO_2 + 8H^+ + 8e^- \rightarrow CH_4 + 2H_2O \quad E_0 = -0.24\,V \tag{1-6}$$

$$2CO_2 + 12H^+ + 12e^- \rightarrow CH_3CH_2OH + 4H_2O \quad E_0 = -0.33\,V \tag{1-7}$$

$$2CO_2 + 12H^+ + 12e^- \rightarrow C_2H_4 + 4H_2O \quad E_0 = -0.34\,V \tag{1-8}$$

$$2H^+ + 2e^- \rightarrow H_2 \quad E_0 = -0.42\,V \tag{1-9}$$

The required potential for various products is concentrated in a narrow range, which makes a challenging problem for gaining target product with high selectivity. Moreover, in a common CO_2 electrolyzer, the aqueous electrolyte also provides the possibility of H_2 evolution, which is a strong rival for all CO_2 reduction pathways due to the similar potential window (equation (1-9)). Accordingly, rational design of suitable catalysts and electrolyzer systems with high selectivity to desirable product while suppressing unwanted chemicals is becoming an urgent issue of current research.

1.1.2 CO_2 performance evaluation

There are several parameters always been used to evaluate the performance of CO_2 reduction, which would be affected by the electrocatalysts, the used electrolyzer,

electrolyte, and measuring condition. Here, we introduce the most common parameters below:[16, 17]

(1) onset potential and overpotential (η). Considering the energy barrier that catalytic reaction needs to overcome, the actual applied potential need to be more negative than the thermodynamic potential under equilibrium condition. The potential that could trigger the reaction called onset potential, and the difference between onset potential and equilibrium potential is overpotential.

$$\eta = E - E_{eq} \tag{1-10}$$

Typically, the less overpotential means the less activation energy, and it mainly depended on the intrinsic property of catalyst, which could be used to identify the activity of catalysts.

(2) Faradaic efficiency (FE). Faradic efficiency indicates the ratio of consuming electrons producing target product to the sum supplying electrons by the external circuit.

$$FE = \frac{\alpha nF}{Q} \tag{1-11}$$

Where α is the number of transferred electrons, n is the amount moles of desired product, F is the Faraday constant (95485 C mol^{-1}), and Q is the total passed charge. FEs of different products present the selectivity for each product and affect by the solution concentration, temperature, applied potential, pH, *etc*.

(3) current density (j). Current density is the passed charge through the geometric surface area of working electrode in certain time under applied potential, express the reaction rate and the catalytic activity. Not only the total current density but the partial current density has also been presented in papers, which could indicate

the production rate for the specific product. Under certain potential, the partial current density of desired product is obtained by the multiplication of Faradaic efficiency of this product and the total current density, as shown below:

$$j_{partial} = j_{total} \times FE \quad (1\text{-}12)$$

(4) electrochemical surface area (ECSA). Besides the geometric area, the electrochemical surface area also needs to measure on some occasions, especially for the porous or hollow structure. The ECSA for a specific catalyst is calculated by the below equation:

$$ECSA = SRF \times A_{geo} \quad (1\text{-}13)$$

where SRF is the roughness factor gained from double-layer capacitance, A_{geo} is the geometric area of electrode.

(5) turnover frequency (TOF). Turnover frequency is defined as the number of the molecule produced per active sites per unit time. The catalyst with a high TOF value means it owns more active sites, leading better activity. The value means the ratio of the active sites producing target product (N_p) to the maximum possible active sites (N_c), as shown below:

$$TOF = \frac{N_p}{N_c} \quad (1\text{-}14)$$

1.1.3 Theoretical calculation

Electrochemical CO_2 reduction is a complex system, which involves many parameters that affect the final performance. Hence, it is almost impossible to investigate all aspects, from the electrode structure to the electrolyte types, just via experimental means. We also need to combine with the theoretical/computational

modelling, which could provide an efficient method to estimate the activity of catalysts and screen new catalysts.[18] Many researchers devoted to the studies of theoretical calculation in the past decades and published many papers in this field.[19, 20] Here, we introduced some advanced theoretical techniques widely used for CO_2RR.

(1) CHE model. As mentioned above, the CO_2RR is a multiple proton-electron associated transfer process, and the computational hydrogen electrode (CHE) model has been used to investigate the process.[19] To investigate the origin of the overpotential for oxygen reduction, Nørskov proposed the CHE model from a thermodynamic viewpoint,[21] then extend to various catalytic research, including hydrogen evolution,[22] oxygen evolution,[23, 24] nitrogen fixation,[25] and CO_2 reduction.[26-28]

CHE model can be described as below: the overall reaction on hydrogen electrode is

$$\frac{1}{2}H_2\ (g)\ \leftrightarrow H^+\ (aq) + \ e^- \qquad (1\text{-}15)$$

During the reaction, involved the adsorb atomic H*,

$$\frac{1}{2}H_2\ (g) \leftrightarrow H^*\ \leftrightarrow\ H^+(aq) + \ e^- \qquad (1\text{-}16)$$

According to the definition of standard hydrogen electrode, which means 300K, 1 atmospheric pressure, and pH = 0, the free energy of this reaction is zero. In other words, the Gibbs energy of $\frac{1}{2}H_2\ (g)$ and $H^+(aq) + \ e^-$ is equal, and defines the electrode potential $U = 0$. At applied potential, using the gas phase H_2 as the reference, the chemical potential of electron e^- has changed to $-eU$. So, we could

combine the Gibbs energy and applied potential of above reaction. Using equation (1-15) as an example, the Gibbs energy is:

$$\Delta \mathrm{G}\ (U) = -eU \tag{1-17}$$

For reaction (1-18), the free energy could be calculated based on density function theory (DFT) or search the handbook as equation (1-19):

$$\frac{1}{2} H_2\ (g) \leftrightarrow H^+ \tag{1-18}$$

$$\Delta G_0 = \Delta E + \Delta ZPE - T\Delta S \tag{1-19}$$

Where ΔE and ΔZPE is the difference of adsorption energy and zero-point energy of equation (1-18) via DFT calculation, ΔS is the entropy corrections. When the pH is not 0, the entropy of H^+ should be calibrated by

$$\Delta G\ (pH) = -kT \ln[H^+] \tag{1-20}$$

Equation (1-17) presented the free energy related applied potential of equation (1-15). Based on the definite potential of standard hydrogen electrode, a relation between DFT calculation and electrode potential has been established. Using this method, we could expand the calculation of potential-dependent free energy to extensive reaction systems.

Nørskov and co-workers first applied the CHE model in the research of converting CO_2 convert to C1 species (HCOOH, CO and CH_4) and HER mechanism, using Cu(211) surface as catalyst,[26] and proposed the lowest reaction pathway as shown in Figure 1-1. Using methane as an example, the production engaging *COOH, *CO, *CHO and *COH intermediates. And to drive the reaction, it required an external potential of -0.68V arisen from the pronation of the *CO to *CHO.

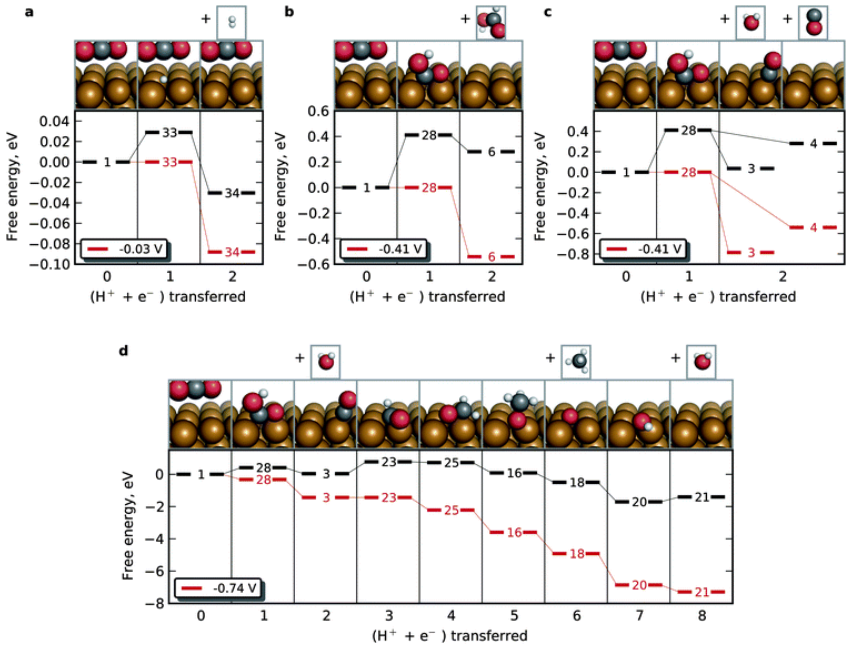

Figure 1-1. Calculated free energy diagram for the lowest energy pathway to (a) H_2, (b) HCOOH, (c) CO, and (d) CH_4.[26] In each diagram, the black (higher) pathway represents the free energy at 0 V vs. reversible hydrogen electrode (RHE), and the red (lower) pathway means that free energy at the indicated potential.

(2) Scaling relations and volcano plots. The binding energies of intermediates on catalyst surface can be calculated as above mentioned, so we could know the key intermediates during reaction process. From the calculated result of the methane production on Cu(211) facet, we could summarize that a catalyst with stronger interaction with *CHO but the same binding strength to *CO is beneficial for high activity toward CH_4 production. However, it is hard to modulate sole intermediate bonding without changing other radicals. Thus, we need a descriptor to compare the activity of various catalysts in a scaling relation of key reaction intermediates.[29] We could make a plot using the binding of a single intermediate as X-axis and the calculated overpotential for each step as Y-axis (Figure 1-2).[30] The lowest line

indicates the determining step of reaction required the highest overpotential. For different polycrystalline metal catalysts, the binding strength of *CO shows the trend of possible reaction pathway as a volcano-type plot. Thus, we could simplify the complicated process of finding suitable catalysts to search the catalyst with the binding energy of key intermediate close to the volcano apex.

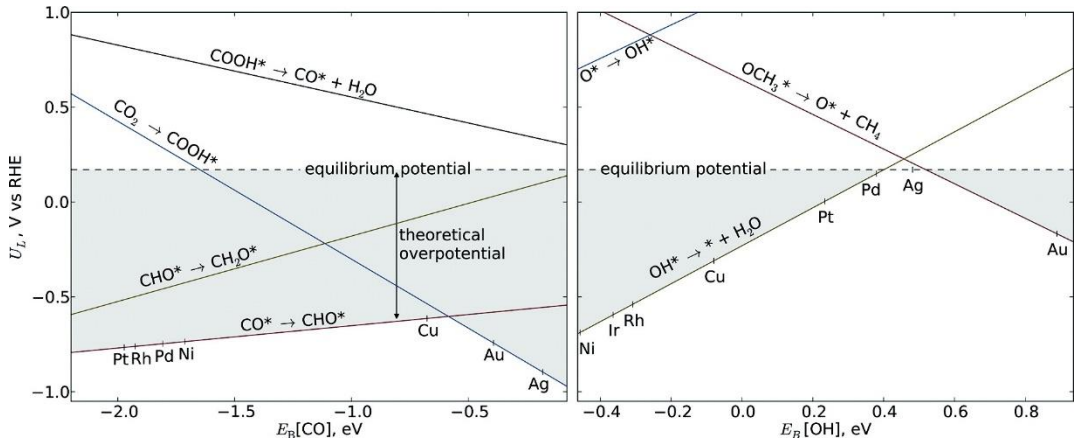

Figure 1-2. Limiting potential (U_L) for elementary proton-transfer steps on the surface of seven transition metals.[30]

1.2. CO_2 reduction catalysts

1.2.1 Classification of catalysts

(1) Metallic catalysts. The CO_2 activation has been regarded as the rate-determining step for CO_2 reduction.[31] Thus, the binding energy of key intermediate and the competitive H* radical is the key parameter to decide the activity and the final product. For the mono-metallic electrocatalysts, they could be divided into four genres,[32, 33] metals of Group I (*e.g.*, Au, Ag, Zn) have a strong bond with *COOH, which selectively reduce CO_2 to CO. Group II metals (*e.g.*, Sn, Hg, Pb, In) tend to produce formic acid due to the difficulty of binding the $CO_2^{\bullet-}$ intermediate. Group III,

which means only Cu, could convert CO_2 to high value-added hydrocarbons through *COH or *CHO intermediates. And the last one, Group IV metals (*e.g.*, Pt, Fe, Ni, Ti) favor the hydrogen evolution reaction in aqueous solution because they can strongly bind the *CO radical, leading the poisoning of sites.

Since Hori and co-workers investigated that copper is the only metal catalyst that could produce hydrocarbons and alcohols with a certain amount, it has been widely researched in CO_2 reduction field.[34, 35] The product distribution varies strongly based on the applied potential (Figure 1-3): under less negative potential, the main product is H_2, HCOOH and CO, while hydrocarbons (CH_4 and C_2H_4) started to yield under more negative potential.[34] Jaramillo's group extended the product range to 16 products of C1-C3 chemicals on polycrystalline Cu electrode with more sensitive identification and quantification characterization method, five of which are the first time been detected (ethylene glycol, glycolaldehyde, hydroxyacetone, acetone and glyoxal).[36]

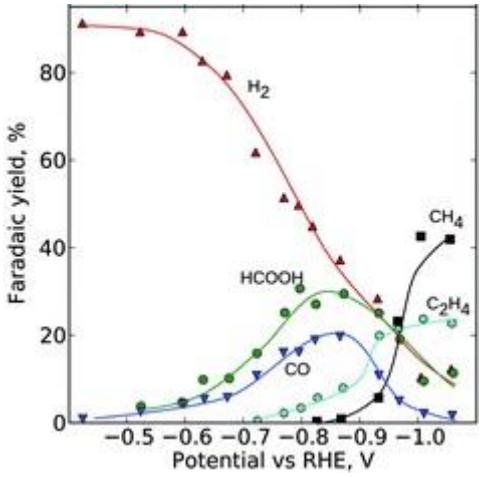

Figure 1-3. Product distribution as a function of the applied potential (versus RHE) in the electrochemical reduction of CO_2 at a copper electrode in 0.1 M $KHCO_3$.[26] The original data were adapted from Hori *et al.*[34]

The various product may be derived from some hypotheses: 1) different types of Cu sites on surface could induce different products; 2) highly-negative potential endow the capability of C-C coupling of two different C1 species originated from the same type site. C-C coupling is the key step for the formation of C2 product on Cu electrode, non-electrochemical mechanism of $*CH_2$ dimerization[37] and coupling between hydrogenated species (*CHO, $*CH_2O$) in an electrochemical environment[38] both effect in different conditions.

With the merit of low cost, Sn is a promising catalyst with high selectivity of converting CO_2 to formic acid since Hori *et al.* found that,[39] although the problems of high overpotential to achieve moderate current densities and low FE due to the competition with HER cannot be ignored.[40] CO has also been found as the possible product of CO_2 reduction on Sn electrode, and the lower pH of electrolyte favors the conversion of CO to formate.[41] Figure 1-4 shows the three possible pathways of forming formate and CO on the Sn electrode.

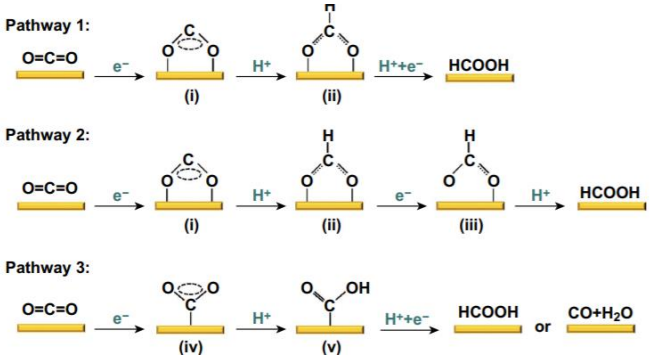

Figure 1-4. Possible reaction pathway for electrocatalytic CO_2RR on the Sn catalysts in aqueous solution.[40]

Transition metal compounds, including oxides, chalcogenides, carbides were found to be potential catalysts for electrocatalytic CO_2RR, but some of them validate

in a limited solvent range of organic solvents. Pb_2O electrode shows a tendency of converting CO_2 to HCOOH with 60% FE in $KHCO_3$ solution.[42] Beyond the toxic oxide of Pb_2O, Sn,[43] Ni,[44] and Ti[45] oxides, which are earth-abundant and low-toxic, also exhibit the potential for gaining syngas or C1 product (including CO, methanol). As for the transition metal chalcogenides (TMCs), in which chalcogenide here often refers to sulfides, selenides and tellurides, different edge sites perform different trends toward various products. As the widely researched catalysts in water splitting, Nørskov *et al.* simulated the activity on different edge sites of MoS_2, $MoSe_2$, and Ni-doped MoS_2 via DFT calculations.[46] Results confirm the bridging S or Se atoms tend to bond with *COOH and *CHO intermediates and promote subsequent reaction steps, while the edge sites of Mo atoms prefer the *CO intermediates, which is possible gaining hydrocarbons or alcohols. Inspired by this, Asadi *et al.* discovered the bulk MoS_2 with Mo-terminated edges exhibited a high current density (65 mA cm^{-2} at -0.764 V vs. RHE) with ~98% CO_2-to-CO FE and low overpotential (54 mV) in EMIM-BF_4 ionic liquid.[47] Kim *et al.* reported that the Mo_2C can catalyz CO_2 into CH_4 at lower applied potential (-0.55 V vs. RHE) compared to Cu electrocatalyst (-0.8 V vs. RHE), attributed by the OH* removal from surface.[48]

(2) Non-metallic catalysts. Noble metals, such as Pd, Au, Ag are the popular catalysts in CO_2 reduction field. Considering the high cost, renewable metal-free catalysts, especially carbon-based nanomaterials with high surface area, excellent conductivity and chemical stability, have been considered as attractive candidates. Carbon-based materials represent in different dimensions and structures, such as zero-dimensional quantum dots, one-dimensional carbon nanotubes or fibers (CNTs and CNFs), two-dimensional graphene, and three-dimensional porous carbon. Normally,

the pristine carbonaceous materials show mere activity toward CO_2 reduction, because the neutral carbon atoms are hard to activate CO_2 molecules. Thus, the most common method to modulate the chemical state of carbon atoms is introduction of doping atoms (B, N, P and S) during or after synthesis.

N-doped CNT[49] and graphene[50] exhibit the selectivity of CO_2 reduction to CO compared to the pristine ones. Different functionalized N atoms lower the activation energy by forming stronger bonds with intermediates, leading the improved activity in the sequence of quaternary-N, pyridinic-N and pyrrolic-N.[51] Wu *et al.* reported a nanometer-size N-doped graphene quantum dots catalyst that is capable of reducing CO_2 into multi-carbon hydrocarbons and oxygenates with high FEs, high current densities, and low overpotentials.[52] While the pristine graphene quantum dots and N-doped reduced graphene oxides primarily yield CO and $HCOO^-$. The high-density of exposed edge sites and the N dopants both grant the unprecedented activity and selectivity of carbon-based materials.

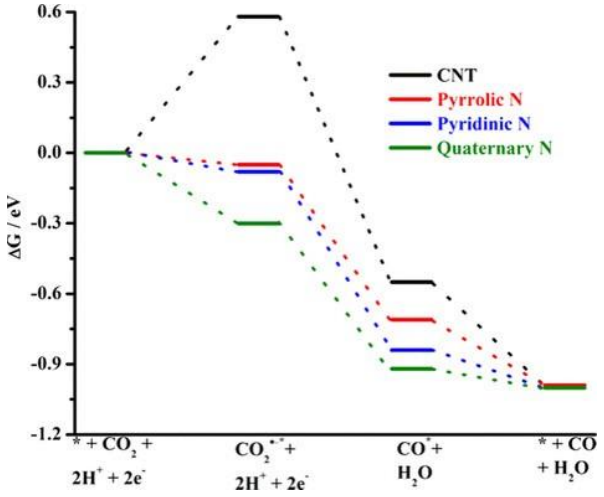

Figure 1-5. Calculated Gibbs free energy diagrams for CO_2 electrocatalytic reduction to CO on pristine CNT and different nitrogen sites at -0.40 V vs. RHE.[51]

In the last few years, Einaga's group focused on the research using bare boron-doped diamond (BDD) and modified BDD electrodes as CO_2 reduction catalysts.[53] Bare BDD electrodes in a continuous flow cell exhibit beyond 90% FE selectivity of formic acid and keep stable under 24-hour operation.[54] And compared with other electrodes, BDD electrodes show an extinct property for the production of formaldehyde with high FE (74%), using either methanol, aqueous NaCl, or seawater as electrolytes, associated with the sp^3-bonded carbon in BDD.[55] The formaldehyde can be formed by a two-electron reduction of formic acid.

$$HCOOH + 2H^+ + 2e^- \rightarrow HCHO + H_2O \quad (1\text{-}21)$$

(3) Molecular catalyst. Molecular catalyst, a family of transition metal complex, is a competitive candidate to selectively reduce CO_2 due to its versatile structure.[3, 56, 57] Compared with the solid catalysts, molecular catalyst more substantially and acutely tailors the chemical and electronic environment of the active sites.[58, 59] It is an old concept but tends to be popular recently, high diversity that combining transition metals with ligands such as porphyrin, polypyridine, cyclam and other macrocyclic structures, presents in electrochemical CO_2 reduction.[18, 60, 61] The separated active site due to the well-defined coordination geometrics is beneficial to the kinetic and mechanistic research.

In 1974, Meshitsuka *et al.* reported that Co and Ni phthalocyanines exhibited current for the passage of CO_2, as the first molecular catalyst for CO_2RR.[62] Then, the representative molecular catalysts for CO_2RR is the tetra-azomacrocyclic complexes of Co and Ni with a high current density of CO_2-to-CO converting and nearly 98% FE.[63] Kubiak and co-workers reported a series of molecular catalysts, including

$Re(bpy)(CO)_3Cl$ (bpy = 2,2'-bipyridine)[64] and $Ru(bpy)(CO)_2Cl_2$,[65] with a different performance by altering the substituents at the 4 and 4' position of the bipyridine ligand. One drawback of molecular catalysts is that few of them show full activity and selectivity in aqueous solutions, but require the nonaqueous aprotic solvent. It is an urgent duty to expand the applied condition of molecular catalysts. A series Cu complex show activity in aqueous solution, Weng *et al.* reported a molecular Cu-porphyrin complex that can reduce CO_2 to hydrocarbons (methane and ethylene) in aqueous media.[60]

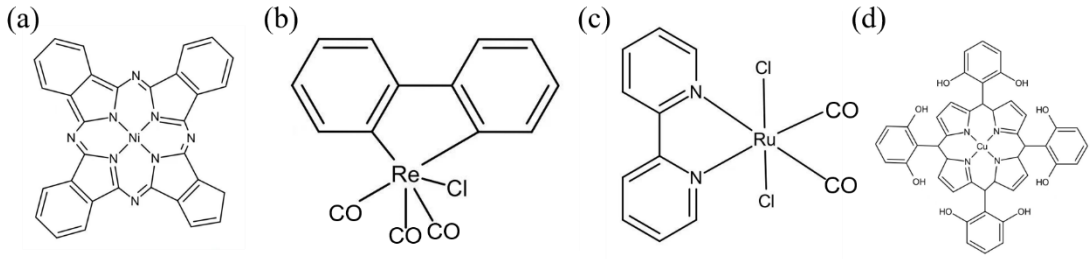

Figure 1-6. Catalyst structures of some representative molecular catalysts mentioned. (a) Ni phthalocyanines;[62] (b) $Re(bpy)(CO)_3Cl$;[64] (c) $Ru(bpy)(CO)_2Cl_2$;[65] (d) copper(II)-5,10,15,20-tetrakis-(2,6-dihydroxyphenyl)porphyrin.[60]

1.2.2 Optimization strategies

The products of CO_2RR mainly depend on the intrinsic property of catalysts as we mentioned above, the four genres of metallic catalysts, but also could manipulate the activity and selectivity via changing the electronic and geometric structure.[16, 66] There are two major guidelines for optimization, increasing the exposed active sites or the catalytic activity of the single site. The former one is often achieved by structural modification, such as nanostructuring, porous hierarchical structure, and exposure of specific crystal facets.[67] And the latter one has a strong relation to the binding energy

of key intermediates, including alloying, doping and defect engineering.[68] In this section, we would introduce some representative methods for the rational design of CO_2RR catalysts.

(1) Oxide-derived metal. Recently, metallic electrodes prepared by intentional oxidation and post-reduction exhibit promising performance for CO_2RR. The oxide-derived (OD) metals, including Au, Sn, Pb and Cu, with tuning oxidative state, have been widely studied by Kanan's group and other researchers.[69] The OD-Cu fabricated by annealing Cu foil in air and electrochemically reducing the result Cu_2O catalyzes the CO_2 reduction to CO and formate at exceptionally low overpotential and to C2 hydrocarbons with almost complete CH_4 suppression at high overpotential.[70] The sites on grain boundary of OD-Cu are suitable for the readsorption of CO, which supply abundant *CO for dimerization, leading an increasing FE of C_2H_4.[71]

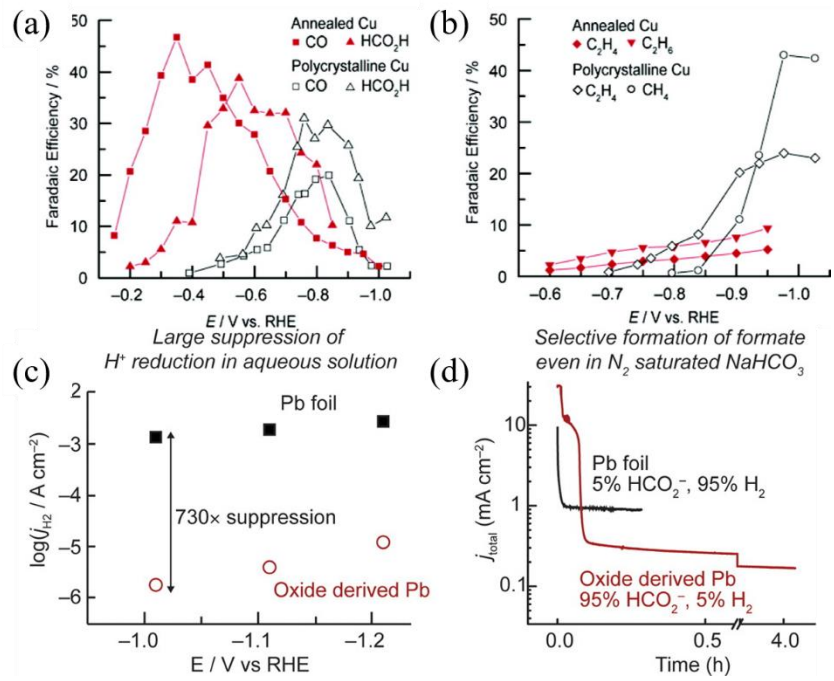

Figure 1-7. Faradaic efficiency for CO, HCOOH, CH_4, C_2H_4, C_2H_6 versus potential of polycrystalline Cu and annealed Cu (a, b);[70] Tafel plot of the HER on Pb foil and

OD-Pb in 0.25M Na_2CO_3 solution (c) and the total current plot of CO_2 reduction in N_2 saturated $NaHCO_3$ solution with low concentrated CO_2 (d).[72]

Chen *et al.* prepared a thin-film catalyst by simultaneous electrodeposition of Sn^0 and SnO_x on a Ti electrode, which exhibited significant enhancement of current density and FE (8 times and 4 times higher, respectively) for CO_2 reduction.[73] Suppression of the inevitable HER process is another aspect for increasing the overall FE for CO_2 reduction, and OD-Pb films prepared by reducing PbO_2 precursors have higher FE for CO_2 reduction to formate with almost no competitive H^+ reduction activity even in the solution with an extremely low concentration of CO_2. The nanocrystalline and defect-rich surface of a metastable Pb oxide passivate the H^+ reduction but activate CO_2 reduction.[72]

(2) Alloying**.** Pure metals have been widely researched for CO_2RR, and the metal alloys possess the potential as a cost-effective solution to tune the activity and selectivity. Here, we focus on the bimetallic alloys. As the most promising metal catalyst due to the capability of hydrocarbons production, Cu based bimetallic alloys with secondary metal atoms to alter inherent adsorption energetics show an improved selectivity. Yang and co-workers conducted a series survey based on the composition of an ordered monolayer on Au-Cu bimetallic nanoparticles, and found CO partial current density presented the same trend with the increasing amount of Au until the ratio of Au to Cu reached 3:1 with the exclusion of hydrocarbons.[74] The elemental arrangement of different metal atoms also shows the impact on the CO_2RR performance. Ordered, disordered, and phase-separated (atomic ratio is 1:1, 1:3 or 3:1) Cu-Pd catalysts with different atomic arrangements were prepared by Ma *et al.*

Ordered CuPd exhibited the highest selectivity for C1 product (＞80%), while phased-separated CuPd is beneficial to gain C2 chemicals (＞60%).[75] Moreover, the alloying method also could combine with the oxide-derived strategies, Ren *et al.* reported that the oxide-derived Cu_xZn catalysts tuned the selectivity of CO_2RR based on the amount of Zn dopant, and maximum FE of ethanol reached 29.1% with a current density of -8.2 mA cm^{-2} under -1.05 V vs. RHE potential.[76]

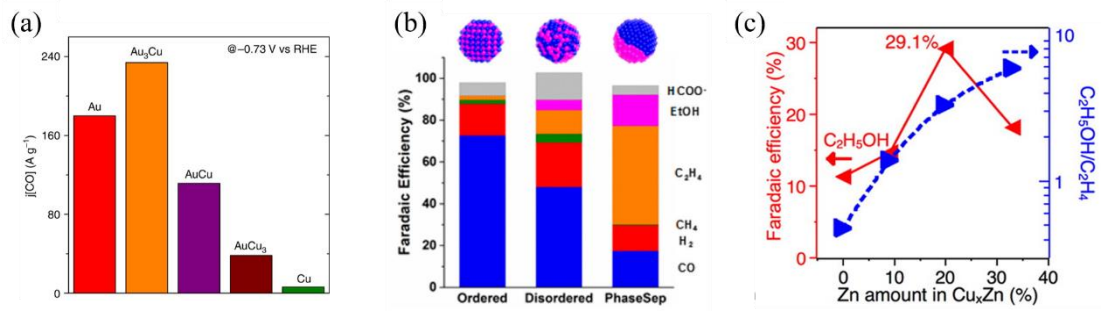

Figure 1-8. (a) CO mass activity of Au-Cu bimetallic nanoparticles at -0.73 V vs. RHE;[74] (b) product distribution from CO_2RR of Cu-Pd alloy with different atomic arrangement;[75] (c) FE of ethanol and the ratio of C_2H_5OH/C_2H_4 using Cu_xZn catalysts with different Zn amount for CO_2RR.[76]

(3) Single-atom catalysts. Recently, single-atom catalysts (SACs), with isolated metal atoms anchored on a solid substrate, emerged as a new frontier in catalysis science, including the CO_2RR region. SACs with full metal atom utilization, adjustable coordination number, and tunable electronic structure endow the high activity and the selectivity.[77] Advanced characterization tools, including the synchrotron-radiated X-ray absorption fine structure (XAFS) and sub-angstrom-resolution aberration-corrected scanning transmission electron microscopy (AC-STEM), have been devoted to gain the information of local atomic and electronic

structure. DFT calculation is effective in screening the metal atoms on the substrates. Back *et al.* calculated 12 metal elements of single atom anchored on defective graphene with single or double vacancies as CO_2RR catalyst, and found Ni and Pt SACs favored the formation of CH_3OH, while Os and Rh SACs tend to produce CH_4.[78, 79] Transition metal-based SACs are more widely studied in the experimental aspect. Jiang e*t al.* proposed a CO_2RR catalyst of Ni single atoms into nitrogen-doped graphene nanosheets (Ni-NG) with a high CO selectivity of 95% under an overpotential of 550 mV.[80] Then they expand the carbonaceous substrate to a commercial carbon black via a simple and scalable method, and applied in CO_2 electrolysis for large-scale production of CO.[81]

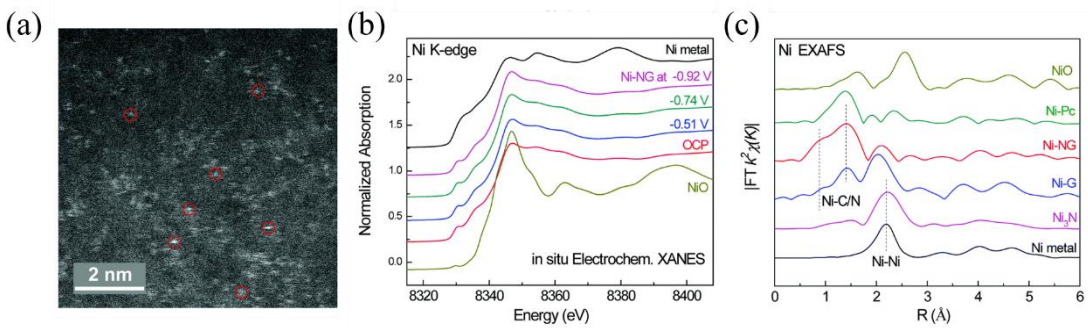

Figure 1-9. (a) aberration-corrected high angle annular dark-field (HAADF) STEM image of Ni-NG nanosheets. XAS spectra of *in situ* electrochemical analysis (b) and in comparison to other Ni-based samples (c).[80]

(4) Structural modification**.** Nanostructured catalysts show good performance in CO_2 reduction with a high density of active sites, and the morphological and/or structural regulation, which could further optimize the activity and selectivity. As a representative CO_2RR catalyst, nanostructured Cu has been widely researched in different dimensional formation, from 0D nanoparticle (NP),[82-84] 1D nanowires

(NWs)[85, 86] to 3D hierarchical structure.[14] Strasser's group prepared Cu NP catalysts in the 2-15 nm range, exhibiting suppression of hydrocarbons (CH_4 and C_2H_4) on nanoscale Cu surface, and increased selectivity for H_2 and CO with decreased Cu particle size (< 5 nm), which related to the more undercoordinated sites.[82] A variety of 3D nanostructure of Cu electrode has been fabricated, including the Cu mesopore electrode,[87] fine needle-like structures,[88] nanoporous Cu film,[89] which show a trend of CO_2 toward ethylene with high current density. Crystal orientation also affects the final product distribution on different metals.[13, 90] Take Cu as an example, Cu(111) facet usually favors the CH_4 production, while the Cu(100) facilitates the *CO dimerization to gain C_2H_4.[91, 92] Nanostructured catalysts modulate the performance not only by the number of active sites, but also by the local condition for CO_2RR. Sargent's group reported an electrodeposited sharp Au nanostructure with local high electric fields that concentrate electrolyte cations to activate CO_2 reduction on catalyst surface. The Au nanoneedles reached 22 mA cm^{-2} of CO_2-to-CO partial current density with 0.24 V overpotential, which is ~10 times to the best Au nanorods.[93, 94]

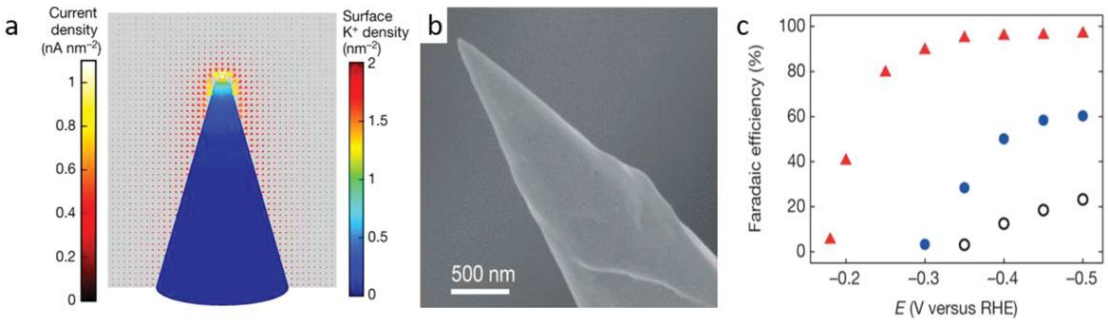

Figure 1-10. Current density and surface K^+ (cations from electrolyte) distribution on the surface (a) of Au needle (tip radius is 5 nm) and corresponding SEM image (b).

Potential-dependent FE of CO using Au needles (red triangle), Au nanorods (blue cycle) and Au nanoparticles (black hollow cycle).[17, 93]

1.3. Electrolysis system

To gain a practical CO_2RR electrolysis system with high current density, superior Faradaic efficiency and long-term stability, besides the catalyst, the electrolyzer type, electrode structure and electrolyte is also an indispensable part. Significant improvements have been developed to design and fabricate a novel CO_2 electrolysis system with better performance, and we will discuss it below.

1.3.1 Electrolyzer

(1) H-type cell. Traditionally, researchers carried out CO_2RR experiments in CO_2 saturated aqueous solution by a homemade liquid-phase reactor, which is typically called H-type cell, as illustrated in Figure 1-11a.[15, 95] H-type cell equipped with two independent chambers for cathode and anode, separated by an ion-exchange membrane to prevent the reduced products from second oxidation. Working electrode and reference electrode are fixed by the caps on the cathode chamber, counter electrode fixed on the anode side. The working electrode could be the bulk catalysts (*e.g.*, metal foil or mesh) or powder catalysts deposited on glassy carbon or carbon paper as substrate. CO_2 gas is purged into the electrolyte then reacted with catalysts in cathode chamber, gas phase products are collected from the headspace, or an online characterization device has been applied. Liquid phase products analysis are extracted from the electrolytes directly. Various advanced analytic techniques have been devoted to the characterization of products, including the gas chromatography (GC), liquid chromatography (LC), and nuclear magnetic resonance spectrometer (NMR).

However, liquid products, which generally mix with many kinds of chemicals and show low concentration in electrolytes, are hard to detect, leading a longer electrolysis time and smaller volume for electrode chamber. As we mentioned above, Jaramillo successfully distinguished 16 different products at the first time using Cu catalyst for CO_2RR assisted by a modified H-type cell with a larger working electrode and less electrolyte, as Figure 1-11b shown.[36]

The merits of H-type cell are obvious in lab-scale tests of facile assembly, easy operation and low cost.[13] However, limited electrode surface, large resistance induced by the long distance between working electrode, and counter electrode and the insufficient CO_2 supply due to the low solubility of CO_2 in water (~ 0.033 M),[96] leading the result of small current density (typically < 100 mA cm^{-2}). Kaneco *et al.* fabricated a stainless steel high-pressure vessel with an H-type glass cell (Figure 1-11c) to provide high-pressure CO_2 with 10 atm, and conducted the experiments of CO_2RR using Cu foil catalyst at low temperature.[97] It is still challenging to achieve the requirement for industrial application (> 300 mA cm^{-2}) in an ambient condition, we have to develop an alternative electrolyzer for extensive employments.

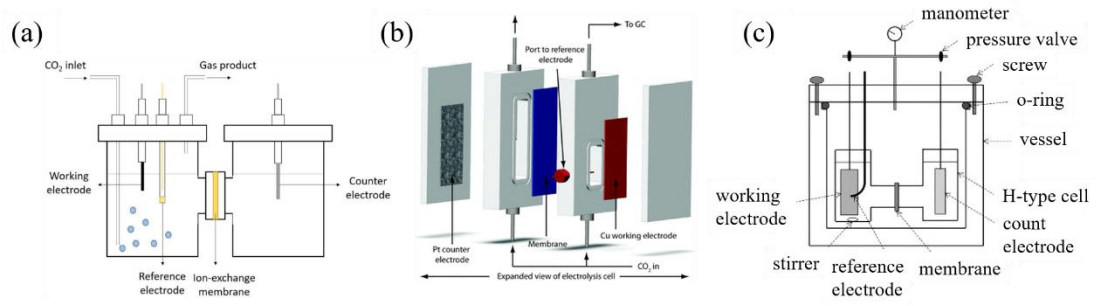

Figure 1-11. Illustrations of traditional H-type cell (a),[95] modified H-type cell by Jaramillo *et al.* (b),[36] and the stainless steel high-pressure vessel with an H-type cell (c).[97]

(2) Gas-phase electrolyzer. Continuous CO_2 flow directly supplies by the gas-phase using a flow reactor is a solution to the problem of limited mass diffusion, leading a significant increase of current density.[98] Furthermore, the common electrolyte using for liquid-phase electrolyzer is the neutral electrolyte, although the alkaline electrolyte would be more suitable for CO_2RR due to the low concentration of protons. The CO_2 stream would like to react with the OH^- ions to form bicarbonate (HCO_3^-) solution, mediate the pH to the neutral condition. The working electrode using in liquid-phase electrolyzer is normally based on a gas diffusion electrode (GDE). The flowing gas would diffuse through GDE and consume at the triple-phase boundary (CO_2-catalyst-electrolyte) instantly.

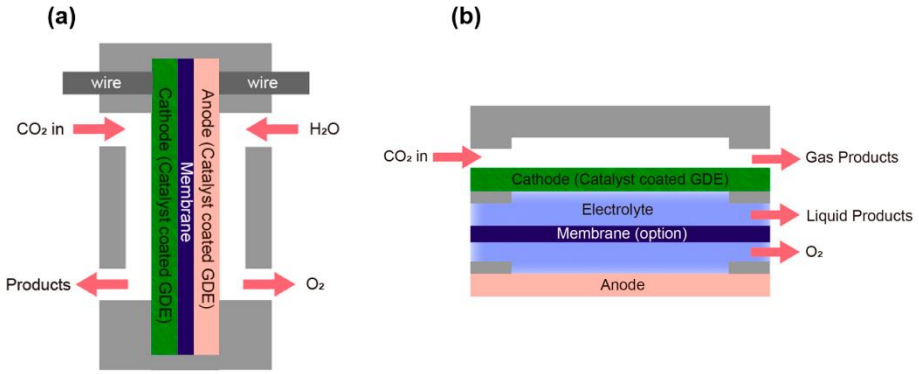

Figure 1-12. Typical schemes of two flow reactors. (a) membrane electrode assembly (MEA); (b) microfluidic cell (MFC).[99]

In general, the flow reactor is categorized into membrane electrode assembly (MEA) and microfluidic cell (MFC) based on the architecture, as presented in Figure 1-12.[99] Since Cook *et al.* firstly conducted CO_2RR experiment in an MEA device,[100] it has been widely researched in many aspects. There is no aqueous electrolyte between electrodes, replaced by an ion-conducting polymer, which decreases the overall ohmic overpotential of cell.[101] There are many options for the

ion exchange membrane, and the anion-exchange membrane (AEM) is beneficial for CO_2RR experiment compared with cation exchange membrane (CEM) due to the facilitation of (bi)carbonate ions transfer and the low proton concentration, which is the key factor to hinder HER.[102, 103] The first MFC application in CO_2RR field is Kenis and co-worker's experiment of CO_2 reducing to formic acid using different catalysts with wide flexibility in operation conditions.[104] In this setup, a very thin channel separating the anode and cathode replaces the membrane with flowing electrolytes. Without the membrane, the separation of product from reduction and oxidation process is attributed by the product diffusion.

1.3.2 Gas diffusion electrode

Gas diffusion electrode, as the main component of flow reactors, is comprised of a gas diffusion layer (GDL, cross-linked carbon fibers), a microporous layer (MPL, mixture of carbon black nanoparticles and polytetrafluoroethylene (PTFE)), and a catalyst layer.[14] Compared with the traditional H-type cell, the flow cell equipped with GDE possesses a much thinner diffusion layer close to the triple-phase boundary of ~ 50 nm (50 μm of H-type cell), which is beneficial to the high concentration of reacted CO_2.[105]

The morphology, porosity, thickness and hydrophobicity of GDE have an obvious impact on the CO_2RR performance due to the complicated gas and liquid flow. Especially, flooding is the major problem to the long-term stability test when applied high current density, which requires superior hydrophobicity. To solve this problem, increasing the amount of PTFE in the MPL layer or coating another PTFE on GDE have both been developed. Kim *et al.* investigated a wide range of PTFE% in

MPL, and found the optimum level is around 20 wt% PTFE, which showed 280 mA cm^{-2} partial current density of CO_2-to-CO at a cathode potential of -2.2V with no decay during 4-hour continuous operation.[106] Sargent's group created a sandwich-like GDE, which means the Cu catalyst layer is in the middle of the separated PTFE and carbon nanoparticles layer with an extra graphite layer. The pure PTFE is more stable to avoid the flooding problem, leading a constant high efficiency of C_2H_4 (beyond 70%) over 150 h operation in 7 M KOH, as shown in Figure 1-13.[107]

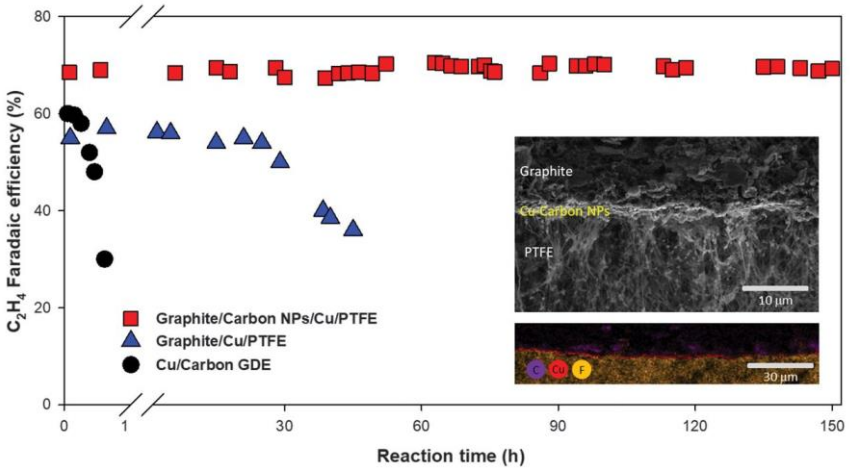

Figure 1-13. Stability test of a new sandwich-like electrode.[107]

The catalyst layers are commonly deposited via drop-casting, airbrush and electrodeposition, which show various morphology, chemical composition and overall structure.[101] Ru *et al.* compared three deposition methods via visualization techniques: hand-painting, air-brushing, and screen printing, confirmed that more homogeneous catalyst distribution and less particle agglomeration promote the catalytic performance.[108] Puring *et al.* control the catalyst loading with the same content of PTFE, leading the change of surface area, pore size distribution and

wettability. And with the increased loading of catalyst, the electrode faced the risk of blocked pore channel of carbon black.[109]

Three-dimensional (3D) nanostructured catalysts are usually grown via direct electrodeposition on GDE surface.[110] The various morphologies, including a layer of wires, needles, dendrites or 3D porous structures, providing a large number of active sites for catalytic reaction. Electrodeposited Ag,[111] Cu,[88] Zn[112] dendrites have been prepared by different optimized methods and show better performance in current density and selectivity compared with the bulk metals. To reduce the metal ions in electrolyte, the negative potential is required, which also drive the H_2 bubbles via hydrogen evolution to gain a porous structure, as the Ag foam.[113] Besides the single metal, benefit from the simple modulated ratio of electrolyte composition, co-deposition is also a facile method to prepare alloy catalysts. Lai *et al.* reported a series of electrodeposited In/Sn alloys on GDEs with different chemical composition, and confirmed that the $In_{0.90}Sn_{0.10}$ alloy electrode exhibited the better CO_2RR selectivity toward formate formation (~92%) and kept stable during 15 h operation.[114]

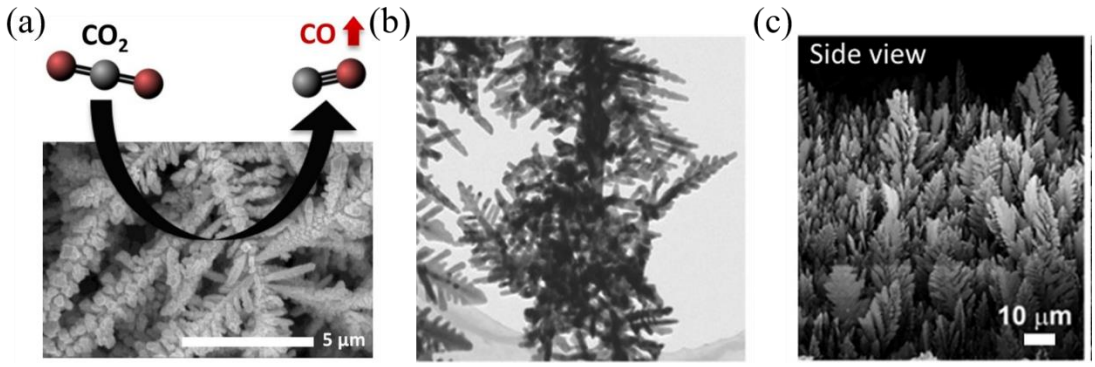

Figure 1-14. Dendrite structures prepared by electrodeposition method on GDE of Ag (a),[111] Cu (b)[88] and Zn (c).[112]

1.4 Thesis overview

The purpose of this study is a better understanding of the overall electrocatalytic CO_2 reduction process in experimental or theoretical view, to develop various methods to hinder the most serious side reaction of hydrogen evolution in aqueous system, which is beneficial to the large-scale application and exploration of secondary use based on CO_2 reduction. And in this thesis, we developed optimization methods from the modified electrolyzer to the rational design of electrocatalysts via state-of-art techniques.

At first, we fabricated a gas diffusion electrode-based three-compartment cell as the platform for subsequent research of CO_2RR. Compared with the plate electrode (PE)-based traditional two-compartment cell, the GDE-based cell largely suppressed the hydrogen evolution even in a pH=2 acidic electrolyte using Ni-doped covalent triazine framework catalyst. The thinner diffusion layer near the triple-phase boundary of GDE facilitates the increase of local pH due to the fast consumption of protons in the thin layer, and the elevated pH has been proven via experiments.

We also studied another factor that influenced the CO_2RR performance, catalyst modification. As the most intensively researched catalyst, copper still faces the problem of competitive HER induced by the unsaturated-coordinated sites. We replaced the unsaturated sites with the inert metal in low contents, which means Sn in there, to suppress the activity both for CO_2RR and HER, leading the emphasized behavior of saturated Cu sites, which prefer CO_2RR. Theoretical calculation confirmed the preferred site of Sn atoms replacement in low contents, and the Sn

modified Cu catalysts showed suppression of HER and an acceleration of CO production in CO_2RR measurements.

Electrodeposition on the GDE shows impressive advantages of gaining a homogenous catalyst layer, manipulating catalyst morphology and chemical composition compared with the coating method via the regulation of electrolytes and the deposition mode. We changed several electrolytes targeted different catalyst preparation with porous structures or specific crystal orientation, and investigated the morphological change via SEM and structural information via XRD. The CO_2RR result showed an increase of current densities compared with the dip-coating samples, and the products selectivity presented a strong relationship to the structure of as-prepared samples.

Finally, we conclude our results and present purpose for future works.

Chapter II CO_2 reduction in a wide range by introducing gas diffusion electrode

2.1 Introduction

Covalent triazine frameworks (CTFs), which are synthesized by trimerization reaction of carbonitriles and adopted triazine ring ($C_3N_3H_3$) as a building unit,[115, 116] is a special and emerging class of covalent triazine frameworks (COFs). In a recent work, we have successfully synthesized CTFs hybridized with conductive carbon nanoparticles by introducing carbon particles during the polymerization to improve the pristine poor electrical conductivity.[117] To obtain various catalytic activity, introducing the metal species as active site for catalytic reaction via impregnation process is a common method.[118] Due to the large amount of N sites, various metals can be atomically-dispersed on CTFs, then applied in many kinds of catalytic reactions, including CO_2RR field.[119-124] Furthermore, it was also shown that cascade reactions could also be activated by loading CTFs carrying several different metal species.[125]

Nickel-doped covalent triazine framework (Ni-CTF, as well as Cobalt-doped CTF, Co-CTF) can serve as an effective electrocatalyst for converting carbon dioxide (CO_2) to carbon monoxide (CO), a component of syngas, at an electrolyte pH of 6.8, refer previous work of our group.[126] In the examined potential range (-0.6 to -1.1 V vs. RHE) the maximum FE for electrochemical CO_2/CO conversion reached 90%. The FE of Ni-CTF was significantly higher than that of the Ni-doped fourfold-coordinated porphyrin, which was attributed to the larger adsorption energy of the key

intermediate on the unsaturated Ni in CTF.[126] Although we have thus revealed that Ni-CTF could serve as an efficient electrocatalyst for CO_2 reduction reaction (CO_2RR), not only higher FE but the larger current density is important for electrochemical CO_2RR. Use of a gas-diffusion electrode (GDE) as mentioned in Chapter I, which can overcome the problem of mass transport limitation due to the low solubility of CO_2, is an effective way to accelerate the CO_2RR.[127-133] A typical GDE has three-dimensional microstructures, by which the electrochemically active surface area at the triple-phase boundary, where the catalyst material, electrolyte, and gas pores intersect, is maximized. Although studies for electrochemical CO_2RR have been generally conducted in neutral or alkaline solutions, it is worth investigating the CO_2RR in wide pH range, because some of the CO_2RR products are expected to be further converted to higher-value compounds in various downstream processes. In the present work, considering that Ni-CTF is stable enough in a wide pH range, we investigated electrochemical CO_2RR on GDE loading Ni-CTF (hereafter called Ni-CTF/GDE)

2.2 Experimental Section

2.2.1 Synthesis of electrocatalysts

Ni-CTF and Co-CTF were prepared as CO_2RR electrocatalysts, using a previously reported method.[123, 124, 126] Briefly, a glass vacuum tube containing 2,6-pyridinedicarbonitrile (129 mg, Sigma-Aldrich), Ketjen Black (129 mg; EC600JD, Lion Corp.) and anhydrous $ZnCl_2$ (1.37 g, Wako) was heated to 400°C oven the period of an hour and then held for 40 h. The as-prepared powder was washed with deionized water, 1 M HCl solution (Wako), tetrahydrofuran (THF; Wako) and

acetonitrile (Wako). Then the CTF powder was dispersed in a 10 mM aqueous solution of $NiCl_2$ or $CoCl_2$ and stirred at 80°C in an oil bath for 3 h. The product was thoroughly washed with deionized water to remove residual metal salt, and then collected by vacuum filtration and transferred to a vacuum oven for drying at 60°C overnight.

2.2.2 Electrochemical measurements

GDEs loaded with the CTF catalysts (Ni-CTF/GDE and Co-CTF/GDE) were prepared as follows. Typically, 21 mg of the as-prepared CTF-based catalyst mixed with 2.1 mL of ethanol and 199.5 μL of 5% Nafion 117 solution (Sigma-Aldrich) was sonicated for 30 min to obtain a homogenous catalyst ink. The catalyst ink was spin-coated (800 rpm, 8 s) on a polytetrafluoroethylene (PTFE)-treated carbon paper with a gas diffusion layer (Sigracet, 38BC) repeatedly to achieve a mass loading of ca. 0.4 mg cm^{-2}, and was then dried prior to use. Glassy-carbon plate electrodes loaded with the same amount of CTF catalysts (Ni-CTF/PE and Co-CTF/PE) were also prepared for comparison by the same preparation method using the glassy-carbon plate instead of carbon paper.

Electrochemical measurements were performed using an electrochemical station (HZ-5000, Hokuto Denko) and a two or three-compartment electrochemical cell in conjunction with three electrodes. A Ag/AgCl electrode (with saturated KCl as the internal solution) was used as the reference electrode (RE), and platinum wire as the counter electrode (CE). RE and CE compartments were separated by a Nafion membrane (Sigma-Aldrich, Nafion 117). The geometrical working electrode area was ca. 2 cm^2. The CO_2 flow rate was set at 3 sccm (standard cubic centimeter per minute)

for the GDE. Electrolyte solutions were prepared from 0.1 M $NaClO_4$ (Wako) and specific volume of $HClO_4$ (Wako) based on the pH of the electrolyte. For pH = 14 condition, the electrolyte is 1 M KOH solution (Wako). To analyze the FE of product, the discharge gas would be collected by a PTEE bag for further characterization of possible products after an hour test. 0.1 M $ZnCl_2$ (Wako) was added to the electrolyte as a Zn^{2+} ions source for the verification of the local pH near the electrode. All potentials measured against the Ag/AgCl electrode were converted to the RHE scale without ohmic drop compensation.

2.2.3 Characterization

X-ray photoelectron spectroscopy (XPS; Axis Ultra, Kratos Analytical Co.) was performed with monochromated AlKα X-rays. Cross-sectional analysis of GDE was obtained with a Hitachi S-5000 scanning electron microscope (SEM). The surface of GDE tested in electrolyte with Zn ions analyzed by XPS spectra, scanning electron microscope equipped with energy dispersive spectroscope (SEM-EDS, Miniscope TM3000 and Swift ED3000), X-ray diffraction (XRD, Rigaku miniflex with CuKα radiation) and Raman spectra (JASCO, NRS-3100 with a laser excitation wavelength of 785 nm).

2.2.4 Analyses of CO_2RR products

The gas products were analyzed using gas chromatography-mass spectrometry (GC-MS; GCMS-QP 2010 Plus, Shimadzu, Japan), calibrated using CO and H_2 samples diluted with CO_2 to various concentrations. A 0.5 mL sample of electrolyte after electrolysis was mixed with 0.1 mL D_2O containing 10 ppm (part per million) dimethyl sulfoxide (DMSO; Wako) as an internal standard for characterization of the

products in the liquid phase using nuclear magnetic resonance spectroscopy (NMR; Varian 500 MHz, Agilent). ^{1}D ^{1}H NMR spectra were measured with solvent suppression using a pre-saturation method.

2.3 Results and Discussion

2.3.1 Electrochemical CO_2RR on Ni-CTF/GDE

Figure 2-1a shows a schematic diagram of the electrochemical reactor, which is composed of three compartments: (1) electrolyte compartment with CE, (2) electrolyte compartment with RE, and (3) gas compartment. The working electrode (i.e., GDE or PE) was placed at the boundary between compartment (2) and (3). The gas (CO_2 or Ar) was flowed in compartment (3) when the GDE was used, whereas it was bubbled into the electrolyte in compartment (2) when the PE was used. A proton exchange membrane was set at the boundary of compartments (1) and (2). The representative cross-sectional scanning electron microscopy (SEM) image of the Ni-CTF/GDE in Figure 2-1b shows a ca. 4 μm thick catalyst layer was formed on the microporous layer of the GDE. Characterization results for the Ni-CTF/GDE could see our previous paper.[126]

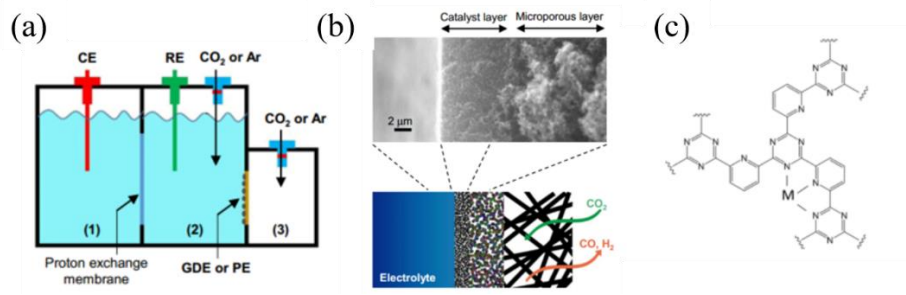

Figure 2-1. (a) Schematic diagram of two- or three-compartment cells; (b) cross-sectional SEM image and diagram of the metal-modified CTF/GDE architecture; (c) schematic illustration of metal-doped CTF

Figure 2-2a shows cyclic voltammograms (CVs) obtained for Ni-CTF/GDE in electrolytes with initial pH = 14 electrolyte under Ar (black) and CO_2 (red) supply conditions. The absolute value of the current density (j_{abs}) exceeding 200 mA cm^{-2} was obtained, indicating that the use of GDE overcome the problem of the low solubility of CO_2, as expected. CO was obtained as the main product of the electrochemical CO_2RR in agreement with our previous study on Ni-CTF/PE;[126] the FE reached 74% at 300 mA cm^{-2} (Figure 2-2b). The above fact indicates that the Ni-CTF/GDE we have prepared have an ideal structure that provides the same level of performance as the general GDE. The Ni-CTF/GDE thus prepared was used for the experiments conducted in acidic electrolytes as shown below.

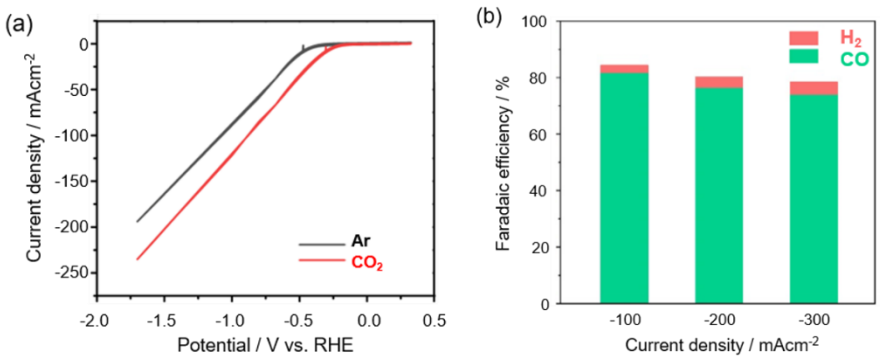

Figure 2-2. CV results (a) and FEs for CO and H_2 generation under different current density (b) using Ni-CTF/GDE in initial pH = 14 electrolyte. Scan rate: 10 mV s^{-1}.

2.3.2 CO_2RR activity in acidic solutions

Next, we examined the CO_2RR activity on GDE and PE in acidic solutions. For both Ni-CTF/GDE and Ni-CTF/PE, CO_2 supply had little impact on the current density-potential curves at pH = 1 (Figure 2-3a and b). For both cases, the j_{abs} started to increase at around -0.5 V, and the curves in both the absence and presence of CO_2 were almost overlapped. The active site for hydrogen evolution reaction is expected

lower density on GDE than on PE, because the half side of the GDE is exposed to gas phase where no proton exists. In fact, j_{abs} on GDE was confirmed to be smaller than on PE. In contrast to the case at pH = 1, the Ni-CTF/GDE and Ni-CTF/PE exhibited contrasting behavior at pH = 2 and 3. On Ni-CTF/GDE, a larger j_{abs} was obtained under CO_2-supply conditions than under Ar-supply conditions, in the potential region more negative than ca. -1.0 V (Figure 2-3c and e). Conversely, a larger j_{abs} was observed on Ni-CTF/PE under Ar-supply conditions than under CO_2-supply conditions (Figure 2-3 d and f).

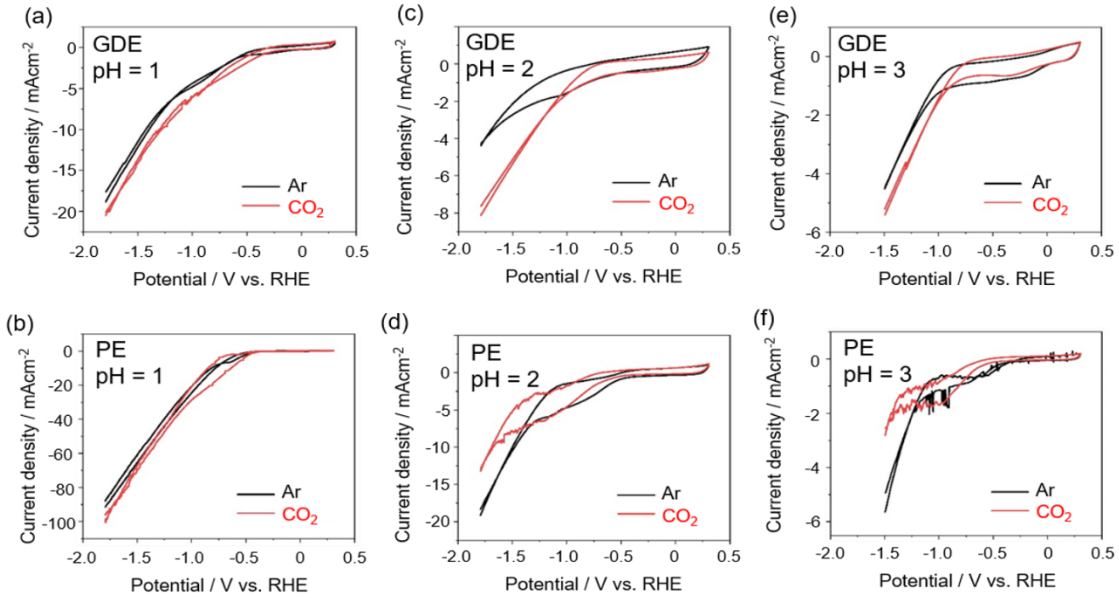

Figure 2-3. CV results of Ni-CTF using a GDE and PE with different pH electrolytes under Ar (black) and CO_2 (red) supply; (a, b) pH = 1, (c, d) pH = 2, and (e, f) pH = 3. Scan rate: 10 mV s^{-1}.

CO_2RR products taken from the liquid and gas compartments (*i.e.*, compartments (2) and (3) in Figure 2-1a) after application of -1.0 V for 1 h were quantitatively analyzed by ^{1}H NMR and GC-MS, respectively. In the present experiments, the applied potential was set to be much higher (and therefore j_{abs} was

lower) than typical experimental conditions for the CO_2RR on a GDE where a large current flows.[81, 107, 129, 134] As is the case with our previous research conducted in an electrolyte with pH = 6.8, it was confirmed that CO was the only detectable product from the CO_2RR on both the Ni-CTF/GDE and Ni-CTF/PE in this pH range (pH = 1–3). Partial current densities for H_2 and CO generation from the Ni-CTF/GDE and Ni-CTF/PE at -1.0 V are plotted against pH in Figure 2-4a and b. The absolute value of the partial current densities of hydrogen evolution reaction (HER) for the Ni-CTF/GDE (solid line) was smaller than that for the Ni-CTF/PE (dashed line) at all pHs examined, and the difference was the largest at pH = 1 (Figure. 2-4a). In contrast, the absolute value of the partial current densities for CO generation from the Ni-CTF/GDE (solid line) was equal to or larger than that from the Ni-CTF/PE (dashed line), as shown in Figure 2-4b.

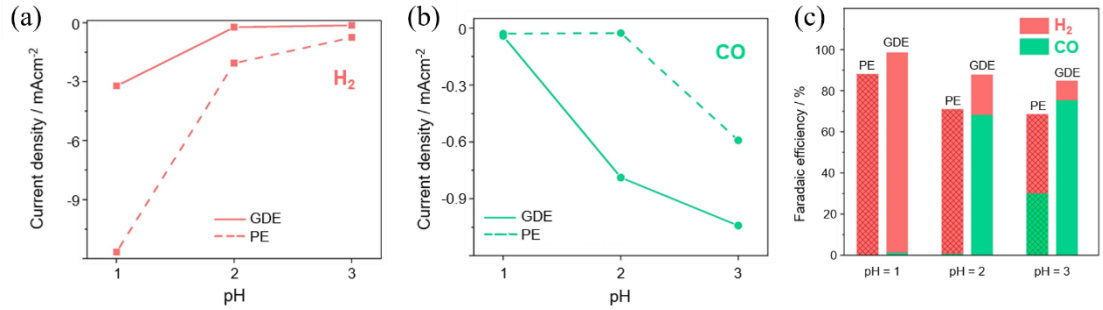

Figure 2-4. Partial current densities of (a) H_2 and (b) CO generation and (c) corresponding FEs from Ni-CTF/GDE and Ni-CTF/PE in electrolyte with pH from 1 to 3.

The FEs at pH = 1, 2, and 3 with an applied potential of -1.0 V are summarized in Figure 2-4c. The HER was the dominant reaction at pH = 1 for both Ni-CTF/GDE and Ni-CTF/PE, as expected. However, the Ni-CTF/GDE and Ni-

CTF/PE exhibited contrasting behavior at pH = 2 and 3. Although the HER was still dominant for the Ni-CTF/PE at pH = 2, the FE for the CO_2RR increased and reached 60% for the Ni-CTF/GDE. The FE for the CO_2RR increased for the Ni-CTF/PE at pH = 3, but it was still lower than that for the Ni-CTF/GDE. From the results given in Figure 2-4, it can be concluded that significant suppression of the HER led to improvement of the FE for the CO_2RR on the GDE at pH = 2 and 3. These results suggest that the local pH around the catalysts is largely different between Ni-CTF/GDE and Ni-CTF/PE, which will be discussed later in detail.

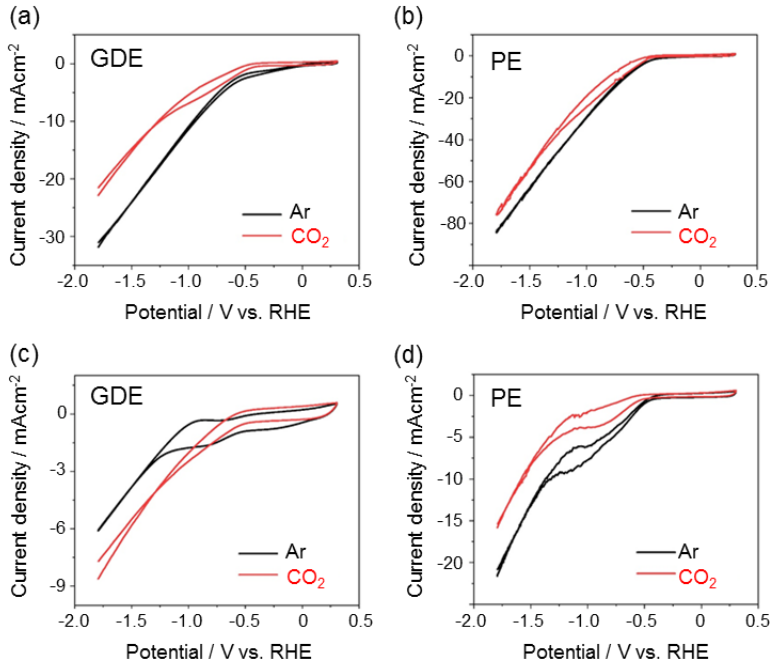

Figure 2-5. CV results of Co-CTF/GDE (left) and Co-CTF/PE (right) with different pH electrolytes in different atmosphere; electrolyte pH = 1 (a, b) and 2 (c, d). Scan rate: 10 mV s^{-1}.

Qualitatively the same results shown in Figure 2-3 and 2-4 were also confirmed for the gas diffusion and plate electrode loading cobalt (Co-CTF/GDE and Co-CTF/PE) as shown in Figure 2-5 and 2-6, which indicate that the GDE structure

rather than the catalyst is the origin of the unusual increase in the FE for the CO_2RR at pH = 2 and 3.

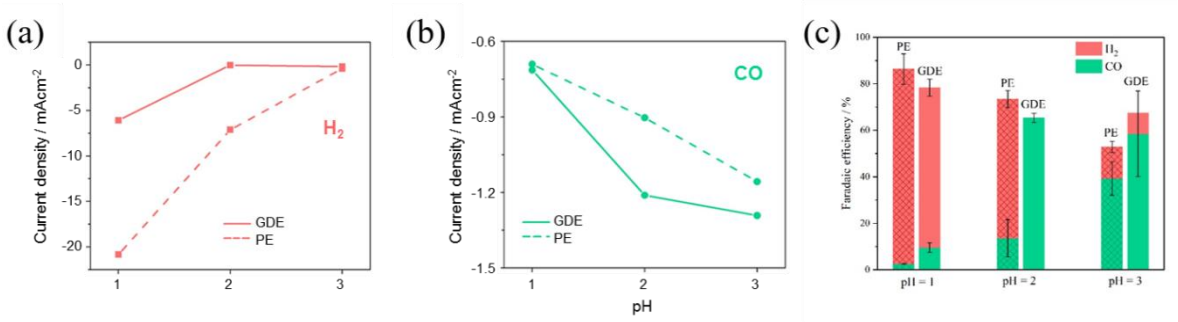

Figure 2-6. Partial current densities of (a) H_2 and (b) CO generation and (c) corresponding FEs from Co-CTF/GDE and Co-CTF/PE in electrolyte with pH from 1 to 3.

2.3.3 Potential dependence

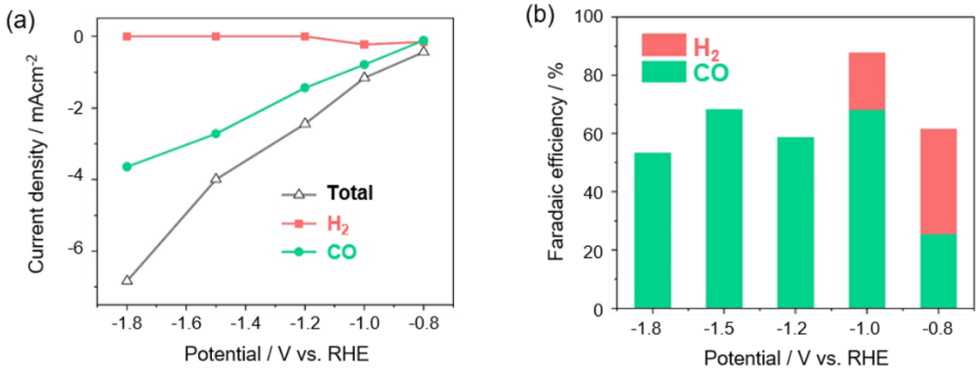

Figure 2-7. (a) Total current density, and H_2, CO partial current densities; (b) corresponding FEs for H_2 and CO generation with Ni-CTF/GDE under different applied potentials and an electrolyte of pH = 2.

In addition to the electrolyte pH, the electrode potential is another key factor that determines the FE for the CO_2RR. Figure 2-7a shows the partial current density for the HER (red) and the CO_2RR (green) for the Ni-CTF/GDE over a wide potential

range from -1.8 V to -0.8 V vs. RHE. These experiments were conducted in pH = 2 electrolyte, in which clear difference was obtained between the GDE and PE. CO was obtained as the sole detectable product in this potential region. Corresponding FE values calculated from Fig. 2-7a are shown against the applied potential in Fig. 2-7b. Both H_2 and CO were detected as the reaction products at -0.8 and -1.0 V, whereas CO was detected as the sole product at potentials more negative than -1.0 V vs. RHE. The Co-CTF/GDE also exhibited similar potential dependence as the Ni-CTF/GDE, as shown in Figure 2-8.

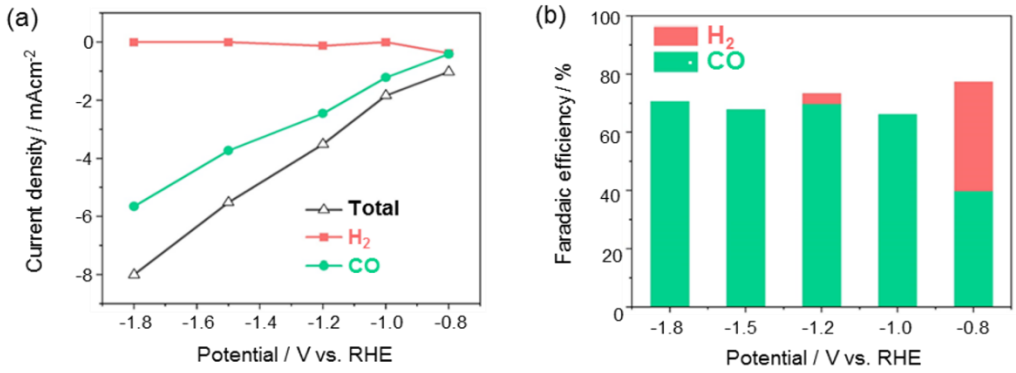

Figure 2-8. (a) Total current density, and H_2, CO partial current densities; (b) corresponding FEs for H_2 and CO generation with Co-CTF/GDE under different applied potentials and an electrolyte of pH = 2.

2.3.4 Verification of local pH increase

In acidic electrolytes, the HER is dominant;[41, 129, 133, 135-137] therefore, the FE of the CO_2RR inevitably becomes small. However, as shown in Figure 2-4, the CO_2RR produced CO with FEs as high as 60% using the GDE, even at pH = 2. This result suggests that the local pH around the catalyst increases during cathodic reactions that consume protons (equation (2-1) and (2-2)).

$$2H^+ + 2e^- \rightarrow H_2 \quad (2\text{-}1)$$

$$CO_2 + 2H^+ + 2e^- \rightarrow CO + H_2O \quad (2\text{-}2)$$

Notably, the increase of the local pH is more significant when microstructured electrodes, such as those with porous, roughened, nanowires, or inverse opal structures, are used, because protons can be more easily depleted inside the confined microstructures.[87, 99, 138-141] The increased local pH commonly leads to improvement of the FE for the CO_2RR via suppression of the competitive HER.[107, 129, 133, 135-137] Based on these previous studies, it is expected that the local pH in the vicinity of a GDE would also be significantly increased due to the 3D microstructured interface, even if there is no difference in the current density between the Ni-CTF/GDE and Ni-CTF/PE.

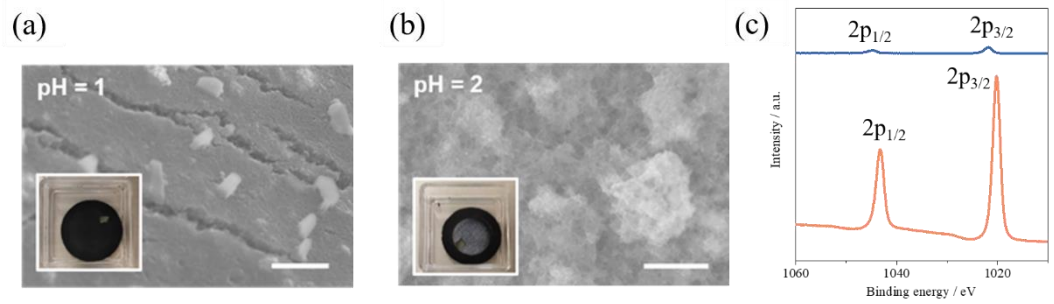

Figure 2-9. SEM images and photographs (insets) of GDE surface after an hour of the CO_2RR in electrolytes with added Zn^{2+} ions at (a) pH = 1 and (b) pH = 2; corresponding Zn 2p spectra of above GDE after test via from XPS spectra.

Therefore, we next attempted to experimentally verify the increase in the local pH at the GDE surface by observing the formation of zinc hydroxides analogues from zinc ions (Zn(II)) that can only proceed in an alkaline solution. Zn(II) becomes solid-state zinc hydroxides analogues on a cathode, even in acidic electrolytes, when the

local pH is increased by cathodic reactions, such as reduction reactions of protons, oxygen, nitrate, and hydrogen peroxide.[142-145] Therefore, if the present hypothesis is true, zinc hydroxide analogues should be formed only on the GDE in electrolytes with pH = 2 and 3.

pH	Zn	O	C	Na	Cl
1	0.45	18.20	71.13	2.03	5.13
2	22.3	50.97	19.99	5.01	1.69

Table 2-1. Surface composition (atom %) by XPS elemental analyses of GDE surfaces after the CO_2RR test in different pH electrolytes with added Zn^{2+}.

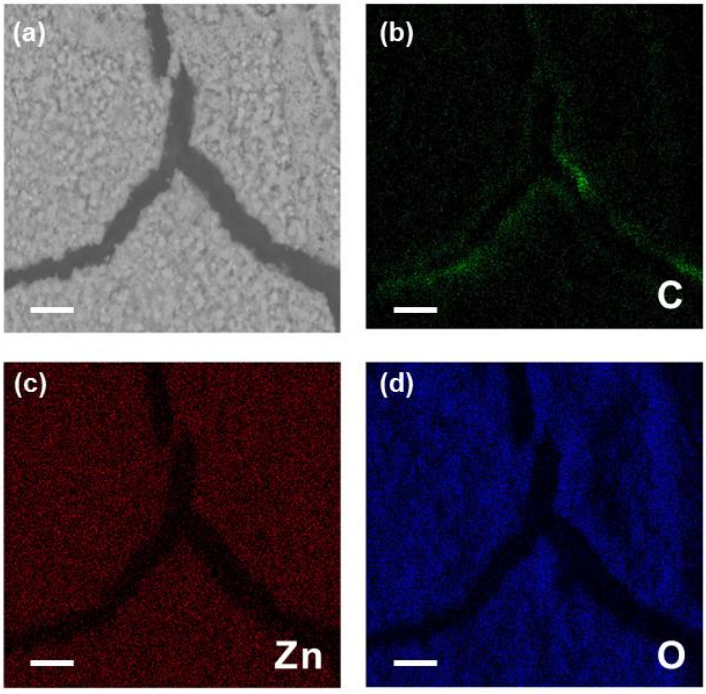

Figure 2-10. (a) SEM image and (c-d) elemental maps of the GDE tested in a pH=2 electrolytes added Zn^{2+} ions.

Figures 2-9a and b show SEM images and photographs of the Ni-CTF/GDE surface removed from the electrolyte after electrolysis for 1 h in the presence of Zn(II) at pH = 1 and 2, respectively. At pH = 1 (Figure 2-9a), there was no deposit other than precipitated salts that could not be completely washed out. In contrast, it was confirmed that the GDE electrode surface was covered with numerous deposits at pH = 2. XPS analyses of the crystals revealed two peaks assignable to Zn-$2p_{3/2}$ and Zn-$2p_{1/2}$ both for the samples obtained at pH = 1 and 2 (Figure 2-9c). The atomic ratio of zinc on the electrode obtained at pH = 2 reached 22.3%, which was significantly larger than that on the sample obtained at pH = 1 (Table 2-1).

	pH	Zn	O	C	Na	Cl
GDE	1	< 1	15	70	3	7
GDE	2	25	59	15	0	1
PE	2	0	9	81	0	1

Table 2-2. Composition (atom%) determined from SEM-EDX measurements of GDE and PE surfaces after the CO_2RR test in different pH electrolytes with added Zn^{2+}.

Figure 2-10 shows and SEM image and energy dispersive X-ray spectroscopy (EDX) elemental maps of the GDE surface, in which zinc and oxygen were confirmed to be homogeneously distributed and the atomic ratio of Zn reached 20% (Table 2-2). However, Zn was not detected by EDX when the PE was used. X-ray diffraction (XRD) and Raman spectroscopic analyses revealed that the deposits on the GDE at pH = 2 were composed of $Zn_5(OH)_6(CO_3)_2$, which cannot be formed in acidic electrolytes (Figure 2-11).[146-148] The experimental results thus indicated that the local pH in the vicinity of the GDE became alkaline, even when the bulk pH was set to 2.

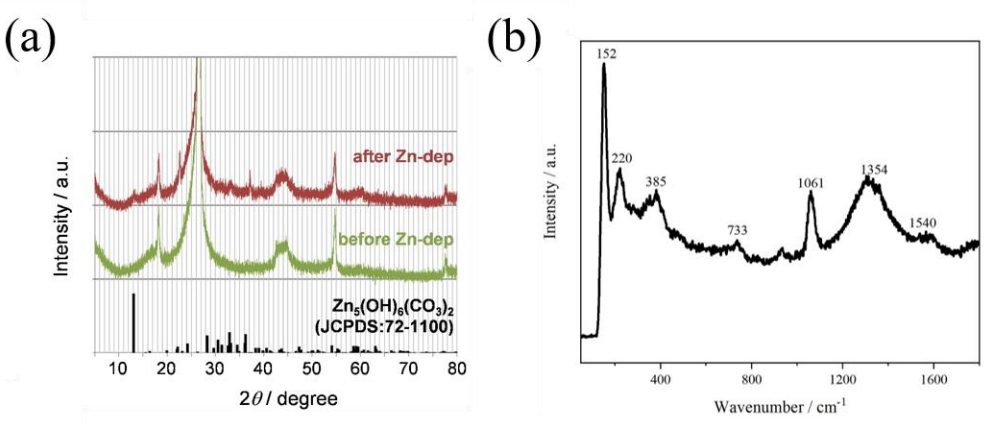

Figure 2-10. (a) XRD patterns and (b) Raman spectra for the GDE with deposited formation during CO_2RR test in the presence of Zn (II) ions.

Finally, let us consider the possible influence of the local CO_2 concentration on the difference in the FE between GDE and PE. As shown in Figure 2-4 and 2-9, despite that there is no difference in the CO_2 supply, in contrast to the case at pH = 2, both the CO and zinc hydroxide analogues were not formed at pH = 1 using same GDE. Furthermore, although CO and zinc hydroxide analogues were formed on GDE at pH = 2, they were not observed on PE in the electrolyte with the same pH. Thus, the formation of CO and zinc hydroxide analogues were always synchronized. The above results clearly show that the difference in the FE between on GDE and PE is not due to the difference in the local CO_2 concentration but in the local pH. Although the local pH can be generally larger when cathodic reactions proceed, the current density on the PE was at the same level as that on the GDE. Besides, it is known that protons can be more easily depleted inside the confined microstructures. Taken all together, this indicates that the increase of the local pH for the GDE is not based on the large current but on the structural features of the GDE, as schematically shown in Figure 2-11.

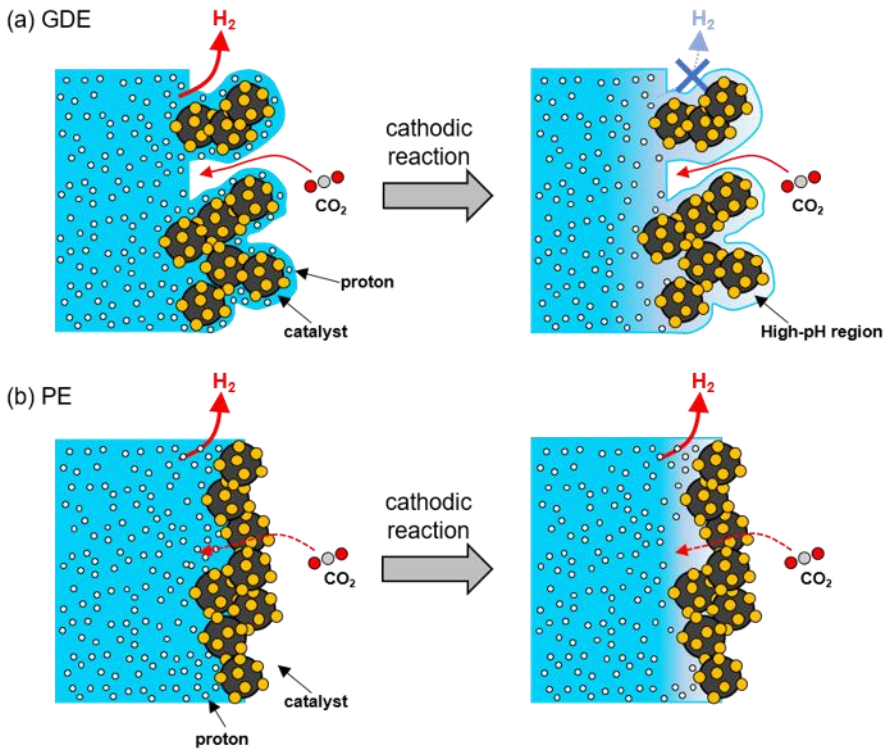

Figure 2-11. Schematic illustration of the local pH increase in the vicinity of the GDE surface.

2.4 Conclusion

In conclusion, we have revealed (1) that high CO_2RR rate exceeding 300 mA cm^{-2} with 74.1% FE of CO could be achieved on Ni-CTF/GDE in an alkaline solution and (2) that the FE reached 60% even in a pH = 2 solution by using GDE. CO was generated as a main product in a wide potential region. The improved FE was attributed to an increase of the local pH, which is specifically induced at the GDE because of the extremely thin electrolyte layer at the triple phase boundary. Although many factors of GDE, including the porosity, hydrophobicity/hydrophilicity, amount of catalyst loading, and the thickness of the microparticle layer, can affect local pH,

the general trend on pH dependence revealed in this study should be hold regardless of the detailed structure of the GDE used.

The increase of the FE of the CO_2RR via the suppression of the HER achieved with a GDE is advantageous to lower the voltage required for the CO_2RR. Various hydrocarbons can be obtained with electrochemical CO_2RR by the selection of appropriate catalysts, which can then be further converted to higher-value compounds in the downstream processes. For example, alcohols and acids can be used as substrates of oxygen fuel cells that are typically operated in acidic electrolytes. Furthermore, aldehyde compounds can be further converted to complex organics via acid-base reactions, such as Aldol condensation catalyzed by protons. Thus, expansion of the pH range to acidic conditions by the use of a GDE could be beneficial when considering secondary uses of the CO_2RR products.

Chapter III Atomic Sn modification on Cu nanoparticles for CO_2RR

3.1 Introduction

As we mentioned in Chapter I, electrochemical reduction of CO_2 has attracted intensive attention because the expected high rate of CO_2 conversion even at ambient temperature and pressure.[6, 12, 31, 67] Metallic copper (Cu) has been regarded as a promising CO_2RR electrocatalyst since the 1980s because only Cu-based electrocatalysts catalyze CO_2 conversion to organic substrates with relatively high efficiency.[34] Consequently, numerous studies on the development of highly active and selective Cu-based CO_2RR catalyts have been reported and introduced in Chapter I.[70, 82, 85, 149-153] However, the existing Cu-based catalysts still suffer from the hydrogen evolution reaction (HER),[34] which competes to some extent with the CO_2RR under a wide range of operating potentials. Therefore, the development of Cu-based catalysts for hydrocarbon production with high selectivity over the HER is important.

Strasser *et al.* investigated the particle size effects of Cu nanoparticles (2−15 nm) as CO_2RR catalysts in detail.[82] They observed a drastic increase in the HER with decreasing Cu particle size, which was attributed to an increase in the population of low-coordinated surface sites and a decrease in the abundance of coordinatively saturated Cu atoms in terrace sites with high selectivity for hydrocarbons. On the basis of this previous report, we hypothesized that an increase in the CO_2RR selectivity over the HER can be achieved through selective deactivation of the low-

coordinated Cu sites. Although there are several possible approaches to deactivating the low-coordinated Cu sites, including the use of organic compounds or inorganic ligands,[154-156] we herein chose to selectively modify Cu nanoparticles with HER-inactive metal atoms at their low-coordinated surface sites because we can avoid adding reactive molecules to electrolytes or electrocatalysts.

Tin (Sn) effectively catalyzes the CO_2RR to produce HCOOH as the main product, with a FE greater than 90% and inhibition of the HER.[157-159] There are several reports of Cu−Sn alloys developed as effective catalysts for the production of HCOOH or CO.[160-167] For example, Wang *et al.* prepared an intermetallic CuSn electrocatalysts (Cu_3Sn/Cu_6Sn_5) via an electrodeposition-calcination process, exhibiting FE of 82% for HCOOH at -1.0V vs. RHE over 42 h operation.[167] Haruyama *et al.* electrodeposited Cu−Sn alloys with different crystal structures and found that $Cu_{87}Sn_{13}$ exhibited high selectivity toward CO (60% FE at −0.99 V vs RHE), whereas $Cu_{55}Sn_{45}$ exhibited 60% FE for HCOOH.[162] Most of the studies on Cu−Sn catalysts focused on bimetallic alloys with different composition ratios (i.e., Cu_3Sn, CuSn, and $CuSn_3$),[162, 167] or control of the morphology by hybridizing Cu catalysts with Sn atoms.[161, 163, 164] In these reports, the Sn content was greater than 10%; thus, the Cu terrace sites, which are active toward hydrocarbon production, were somewhat hindered by Sn atoms. As a result, hydrocarbon production was nearly suppressed. Because the atomic radius of Sn is substantially larger than that of Cu, the low-coordinated sites would be preferentially occupied by the Sn atoms in Cu−Sn catalysts. Therefore, Cu atoms with unsaturated coordination are expected to be selectively replaced when Sn is present at trace levels. On the basis of the aforementioned hypothesis, in the present work, we modified Cu nanoparticles with a

trace amount of Sn atoms and used them as selective CO_2RR catalysts working on GDEs (Figure 3-1). We investigated the preferred site of the Sn atoms and the CO_2RR mechanism using first-principles calculations.

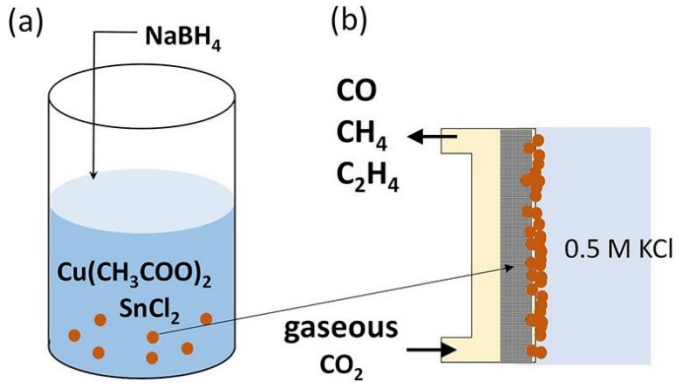

Figure 3-1. Schematic illustration of (a) the synthesis method used for the preparation for Cu/Sn catalysts and (b) the setup for CO_2RR using GDEs.

3.2 Experimental section

3.2.1 Chemical and materials for experiments

Copper(II) acetate monohydrate [$Cu(CH_3COO)_2 \cdot H_2O$, 99%], tin(II) chloride dehydrate ($SnCl_2 \cdot 2H_2O$), hydrochloric acid (HCl, 99%), methanol (CH_3OH, 99.8%), potassium bicarbonate ($KHCO_3$, 99.8%), and potassium chloride (KCl, 99.8%) were purchased from Wako Pure Chemical. Sodium borohydride ($NaBH_4$, 99%) and Nafion solution (5 wt%) were obtained from Sigma-Aldrich. All chemicals were used without further purification. Carbon paper with a gas-diffusion layer (Sigracet 38BC) and Nafion membranes (Nafion 117) were purchased from SGL Carbon and Sigma-Aldrich, respectively. Ultrapure water obtained from a Milli-Q system (18.2 MΩ cm) was used for all catalyst preparations and electrochemical tests.

3.2.2 Catalyst preparation

Sn-decorated Cu nanoparticles (Cu/Sn) were fabricated via a previously reported wet-chemical reduction method in which $NaBH_4$ was used as the reductant.[168] Typically, $Cu(CH_3COO)_2 \cdot H_2O$ and $SnCl_2 \cdot 2H_2O$ were added to a conical flask with the desired elemental ratio and then dissolved in 250 mL of deionized water; the resultant solution was stirred for 30 min under a continuous flow of argon to remove residual O_2. The total amount of metal ions was controlled to 3 mM. $NaBH_4$ (1.14 g) dissolved into 20 mL of ultrapure water was then added to the Cu/Sn solution. The obtained black precipitate was washed with ultrapure water and C_2H_5OH via vacuum filtration. Finally, the prepared samples were dried at 60 °C in a vacuum oven overnight. Pure Cu or Sn samples were synthesized in a similar manner using only the Cu or Sn precursor as the starting material. The physically mixed samples were prepared by hand-mixing in a mortar the pure Cu and Sn powders that were synthesized by the above-mentioned method in the desired ratio.

3.2.3 Characterization

The XPS spectra and XRD patterns are recorded as the same condition using same devices as we mentioned in Chapter II. The elemental analyses were conducted by inductively coupled plasma optical emission spectrometry (ICPOES). Transmission electron microscopy (TEM; Hitachi H-9000NAR) was used for the morphological analysis. A JEOL JEM-2100F microscope equipped with a high-angular annular dark-field scanning transmission electron microscopy (HAADF-STEM) detector was used for TEM, high-resolution TEM (HRTEM), and selected-area electron diffraction (SAED). Sn K-edge X-ray absorption spectroscopy (XAS)

for as-prepared samples was performed on the BL01B01 beamline at the SPring-8 facility (Japan). The radiation was monochromatized by a Si(311) double-crystal monochromator. The spectra were recorded in transmission or fluorescence mode using 19 elements of germanium solid-state detectors. The Sn K-edge and Cu K-edge spectra of catalysts on the electrode after electrolysis were recorded in fluorescence mode. All XAS data were processed and analyzed using the Demeter package.[169]

3.2.4 CO_2 electrochemical reduction measurements

GDEs modified with the synthesized catalysts were prepared as follows. Typically, 5 mg of an as-prepared catalyst was mixed with a solution of 500 μL of CH_3OH and 10 μL of Nafion, and the resultant mixture was ultrasonicated for 30 min in a tip-sonication machine to obtain a homogeneous catalyst ink. The catalyst ink was dip-coated (60 μL) onto a circular GDE to achieve a mass loading of ∼0.6 mg cm^{-2} and was then dried at 60 °C under vacuum prior to use.

Electrochemical measurements were performed using an electrochemical workstation (HZ-5000, Hokuto Denko) and a custom-made three-compartment electrochemical cell presented as Figure 2-1a in conjunction with three electrodes, as reported previously.[170] A Ag/AgCl (KCl-saturated) electrode and a platinum wire were used as the reference and counter electrodes, respectively. The geometric area of the working electrode was ∼1 cm^2. Electrode potentials were transferred to the RHE reference scale with IR compensation. The electrolytes on the cathode and anode sides were 0.5 M KCl and 0.5 M $KHCO_3$, respectively. The anodic and cathodic compartments were separated by a proton-exchange membrane (Nafion 117, Sigma-Aldrich). The gas chamber of the three-compartment cell was bubbled with CO_2 for

more than 30 min before measurement. During the tests, CO_2 gas was flowed at 9 sccm, as controlled by a mass flow controller. The CO_2 gas with gaseous products generated throughout the experiments was collected in a gas bag and subsequently injected into a gas chromatograph using a gastight syringe. The CO_2RR products were sampled after 30 min or 1 h of electrolysis. The roughness factor of the GDEs with Cu/Sn catalysts are estimated by conducting CVs with different scan rates (10, 20, 40, 60, 80, 100 mV s^{-1}) to gain the double-layer currents. Turnover frequencies (TOF) values of CO_2RR product for main products were calculated via following equation:

$$TOF\ of\ product = \frac{FE\ of\ products \times I}{n \times F \times N} \quad (3\text{-}1)$$

where *I* is current, *n* is the electron transfer number (*i.e.*, 2 for CO generation), *N* is the number of active sites on electrode calculated based on the mass amount, and *F* is the Faraday constant (96484 C mol^{-1}).

Gas and liquid product were analyzed like the Chapter II described in major.[171] Considering the relatively high concentration of possible liquid product induced by large current densities in the section, we increased the internal standard to 100 or 250 ppm of DMSO.

3.2.5 Density Functional Theory

The DFT calculations performed to determine the stabilization energies (E_{stab}) of Sn atoms on the Cu surface and adsorption energies (ΔE_{ads}) for reaction intermediates were calculated using the PHASE/0 code.[172] The generalized gradient approximation of the Perdew−Burke−Ernzerhof model and projector-augmented-wave (PAW) method were used. In the calculations, a slab model with three layers of Cu atoms was used. Throughout the calculations, only the bottom layer of Cu was

fixed; other atoms, including adsorbates, were free to move in all directions. The atomic relaxations were conducted until the maximum force on any atom was less than 0.01 eV $Å^{-1}$. The cutoff energy for the planewave function was set to 25 Ry. A *k*-point sampling of a 3 × 3 × 1 Monkhorst−Pack mesh was used. The vacuum space was greater than 15 Å. The E_{stab} for Sn atoms was calculated as follows using a Cu(553) surface:

$$E_{stab} = E_{Sn-Cu} + E_{1Cu} - (E_{Cu} + E_{1Sn}) \quad (3\text{-}2)$$

where E_{Sn-Cu} and E_{Cu} represent the total electronic energies of a Sn-doped Cu surface with a (533) surface with three successive slab structures and a Cu surface without Sn modification. E_{1Cu} and E_{1Sn} represent the total electronic energies for 1 Cu atom and 1 Sn atom, respectively (for detailed structures, see the 3.3 Result and Discussion section) The formation free energies (ΔG) of the reaction intermediates for HER and CO_2RR are calculated by adsorbing H atom, COOH, and CO molecule. G(adsorbate*) was calculated as follows:

$$\mathrm{G} = E_{DFT} + ZPE - TS \quad (3\text{-}3)$$

Where E_{DFT} represents the total energies for each reaction step. ZPE is the zero-point energy, and TS is the entropic corrections. Those value are obtained from previous reports.[126, 173, 174] In the present study, the reaction free energies were calculated using the CHE model as reported previously[21, 46] and introduced in Chapter I.

3.3 Result and Discussion

3.3.1 Physical and morphological characterization of Cu/Sn catalysts

We fabricated Cu/Sn catalysts with various Sn contents (0.5, 1.5, 2.5, 5, and 10 atom %), as well as bare Cu and Sn nanoparticles, by tuning the ratio of the precursors (Figure 3-1a). The bulk composition of the catalysts was quantified by ICP-OES (Table 3-1); the results show that their atomic composition was similar to that of the added precursors. The obtained catalysts are denoted as Cu/Sn-*x*, where *x* indicates the atomic ratio (%) of Sn precursors.

Sn % of precursors	0.5	1.5	2.5	5.0	10.0
ICP-OES	0.43	1.58	2.20	4.79	9.16

Table 3-1. Atomic Sn elemental concentration of As-prepared Cu/Sn-*x* samples, as determined by ICP-OES.

The crystalline structure of the as-prepared catalysts was analyzed by XRD (Figure 3-2). We observed peaks at 30.0°, 36.7°, 42.7°, 43.3°, 50.6°, and 61.6°, which are attributed to the Cu_2O(110), Cu_2O(111), Cu_2O(200), Cu(111), Cu(200), and Cu_2O(220) planes, respectively.[66] In addition, some samples showed small peaks assignable to CuO, which might be derived from the oxidation by air. These results indicate that the dominant crystal phases of these samples were a mixture of Cu and Cu_2O. The XRD results show no Sn-related peaks with increasing Sn content, even at a Sn content of 10%, indicating that crystalline Sn agglomerates, such as Sn metal nanoparticles or oxides, did not form on the Cu/Cu_2O nanoparticles during the synthesis.[162] Furthermore, the intensity ratio, which are related to different crystal

facets, are almost same with the increasing Sn contents, which means that Sn modification on Cu nanoparticles has no impact on the preferred crystal orientation.

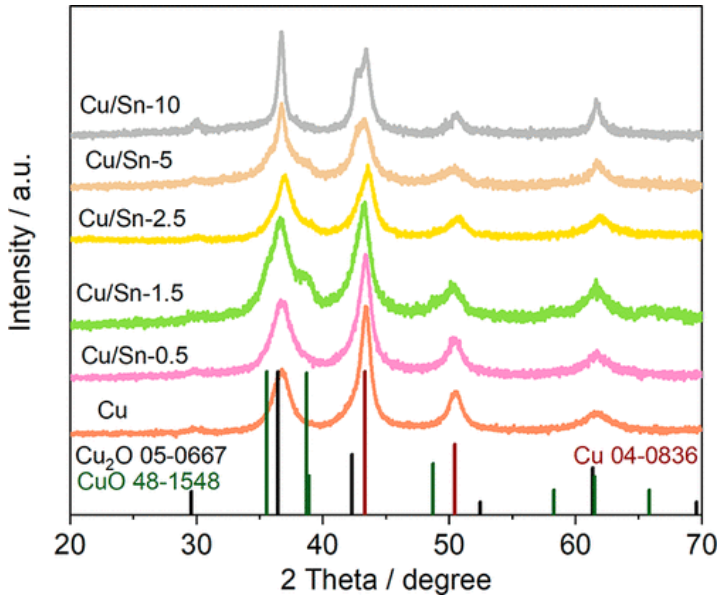

Figure 3-2. XRD patterns of as-prepared Cu and Cu/Sn nanoparticles with various Sn contents. The green, black, and reddish-brown bars indicate the standard peaks of CuO, Cu_2O and Cu, respectively.

We next investigated the morphologies of the Sn-modified Cu samples by TEM imaging (Figure 3-3). Detailed (S)TEM investigations and energy-dispersive X-ray spectroscopy (EDX) mappings were conducted for further structural characterization and observation of the distribution of elements, respectively.

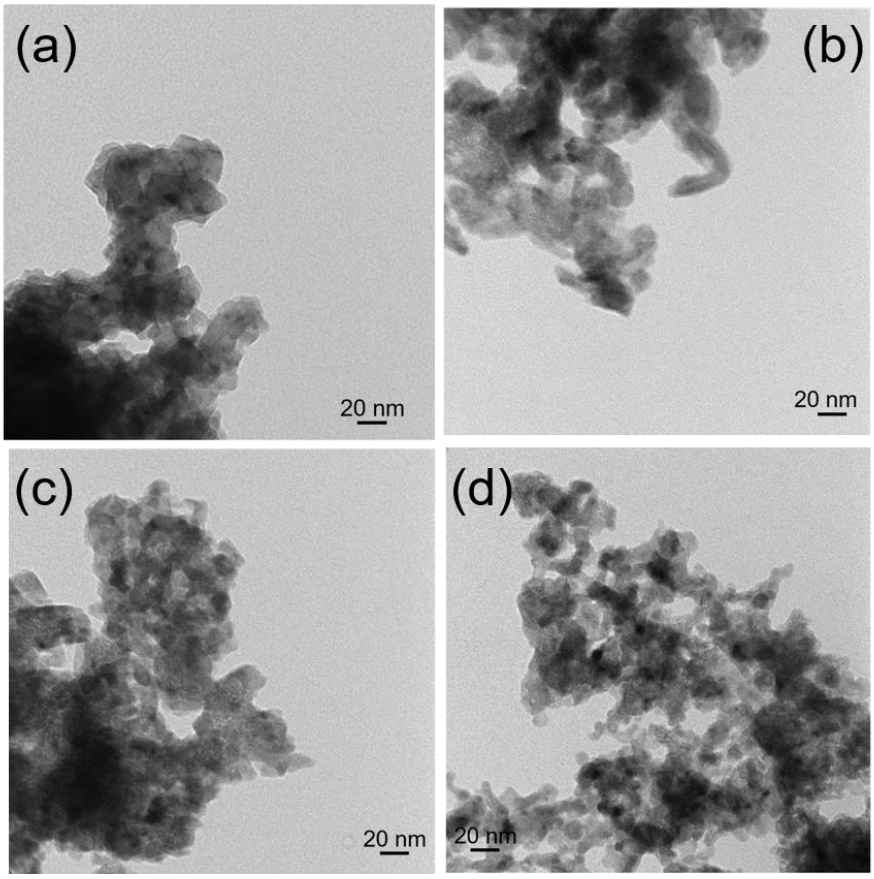

Figure 3-3. TEM images of as-prepared Cu (a), Cu/Sn-0.5 (b), Cu/Sn-1.5 (c), and Cu/Sn-10 (d) nanoparticles.

Representative (S)TEM images and the corresponding EDX mapping images for samples Cu/Sn- 0.5, -1.5, and -10 are shown in Figures 3-4. The HRTEM images (Figure 3-4b) indicate good crystallinity of the Cu/Sn-1.5 catalyst, with a $Cu_2O(111)$ d spacing of 0.240 nm, consistent with the XRD results.[85, 175] The SAED patterns can also confirm a distinct structure of the Cu_2O/Cu mixed phase (inset image of Figure 3-4e). The atomic-scale-resolution STEM−EDX mapping images (Figure 3-4j, k) show a homogeneous distribution of Sn atoms and few Sn aggregates (>1 nm) on the Cu/Sn-0.5 and -1.5 samples. With increasing Sn content, the EDX mapping images of the Cu/Sn-10 sample show phase separation between the Cu and Sn parts, indicating

that Sn agglomerates formed on the Cu agglomerates (Figures 3-4l). The direct observation of atomically dispersed Sn atoms in Cu/Sn catalysts using STEM is in progress in our laboratory.

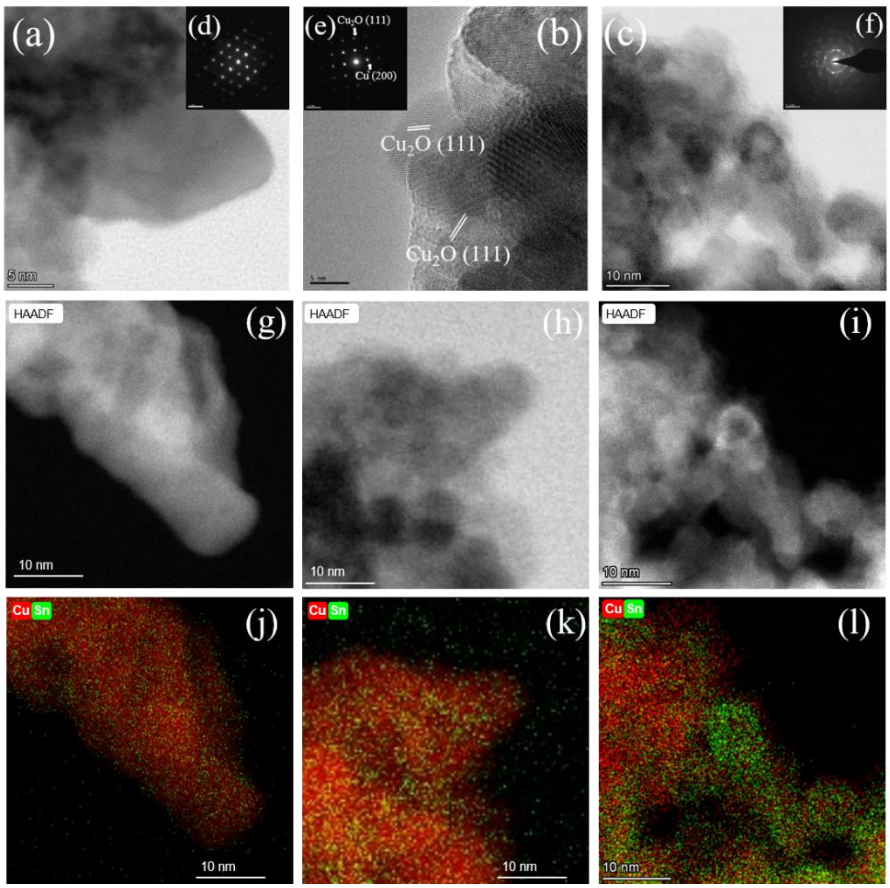

Figure 3-4. HRTEM and corresponding SAED and EDX images of Cu/Sn-0.5 (a, d, g, j), Cu/Sn-1.5 (b, e, h, k) and Cu/Sn-10 (c, f, i, l).

We next investigated the electronic states of the Cu and Sn species in Cu/Sn catalysts using various X-ray techniques. Figure 3-5a, b show XPS narrow-region scans for Cu 2p and Sn 3d, respectively. In Figure 3-5a, the peaks at 932.4 and 952.4 eV, which are assignable to Cu $2p_{3/2}$ and Cu $2p_{1/2}$, are clearly observed, suggesting that the Cu(0) and/or Cu(I) valence state(s) was (were) dominant, although a small portion of Cu(II) was observed in deconvoluted curves (Figure 3-5c).[176] These

results basically correspond to the XRD results. The peaks at 486.0 and 494.5 eV in the spectrum of the Cu/Sn-0.5 sample are assigned to Sn $3d_{5/2}$ and Sn $3d_{3/2}$, respectively (Figure 3b). The Sn 3d peaks of the Sn-decorated Cu nanoparticles shift to higher binding energies by ~0.65 eV when the Sn content is increased from 0.5% to 10%. The peak top positions for Sn $d_{3/2}$ and $d_{5/2}$ finally reach 486.6 and 495.1 eV, respectively, which are positions similar to those of Sn nanoparticles synthesized without Cu. These XPS results reveal that the electronic states of Sn atoms decorated on Cu/Cu_2O nanoparticles are slightly reductive compared with the electronic states of Sn atoms in SnO_2.[177]

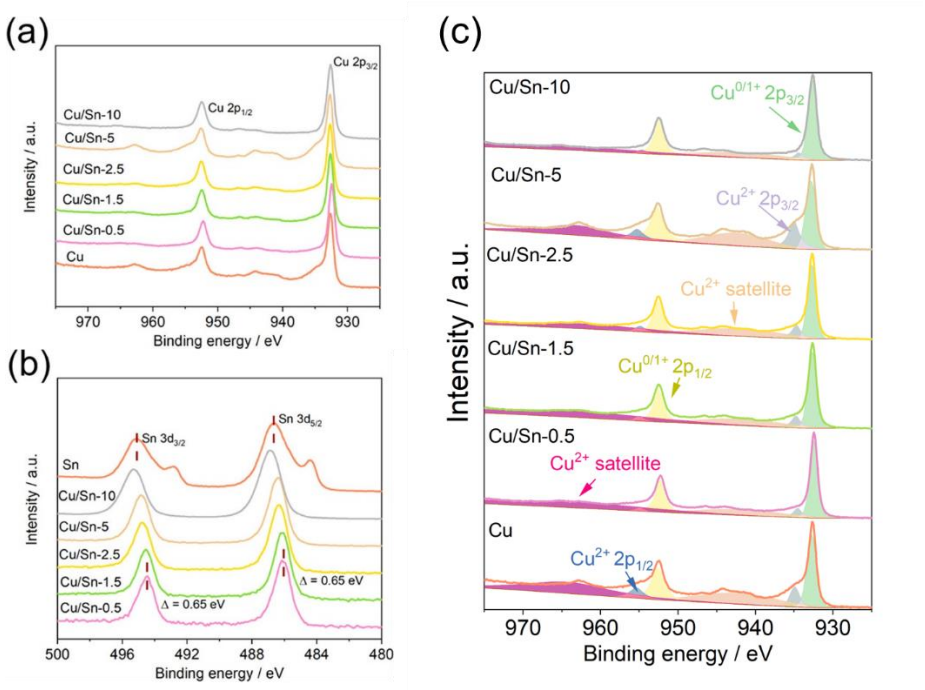

Figure 3-5. High resolution Cu 2p (a) and Sn 3d (b) spectra of Cu or Sn and Cu/Sn catalysts with various Sn contents (0.5, 1.5, 2.5, 5, 10%). And the corresponding deconvoluted peaks (c) of Cu 2p spectra.

X-ray absorption near edge structure (XANES) spectra corresponding to the Sn K-edge (Figure 3-6a) were recorded to obtain further insight into the electronic state of Sn atoms in Cu/Sn catalysts. The onset of the normalized XANES curves for Cu/Sn catalysts (20207.0 eV) corresponded with that for SnO_2, indicating that the Sn(IV) oxidative state is dominant for all Sn species in Sn-decorated Cu/Cu_2O nanoparticles.[178] In contrast, the valence state of Sn atoms in the physically mixed Cu/Sn catalysts is zero, as confirmed by the XANES spectra (Figure 3-6b). Figure 3-6c shows Sn K-edge extended X-ray absorption fine structure (EXAFS) spectra for Cu/Sn catalysts, and the fitting results of EXAFS are summarized in Table 3-2. The coordination number of the first coordination sphere containing O atoms (the peak at 1.7 Å) for Cu/Sn catalysts is smaller than that for SnO. In addition, the peak at 3.5–4.0 Å assignable to the second coordination sphere observed in SnO_2 is rarely observed.

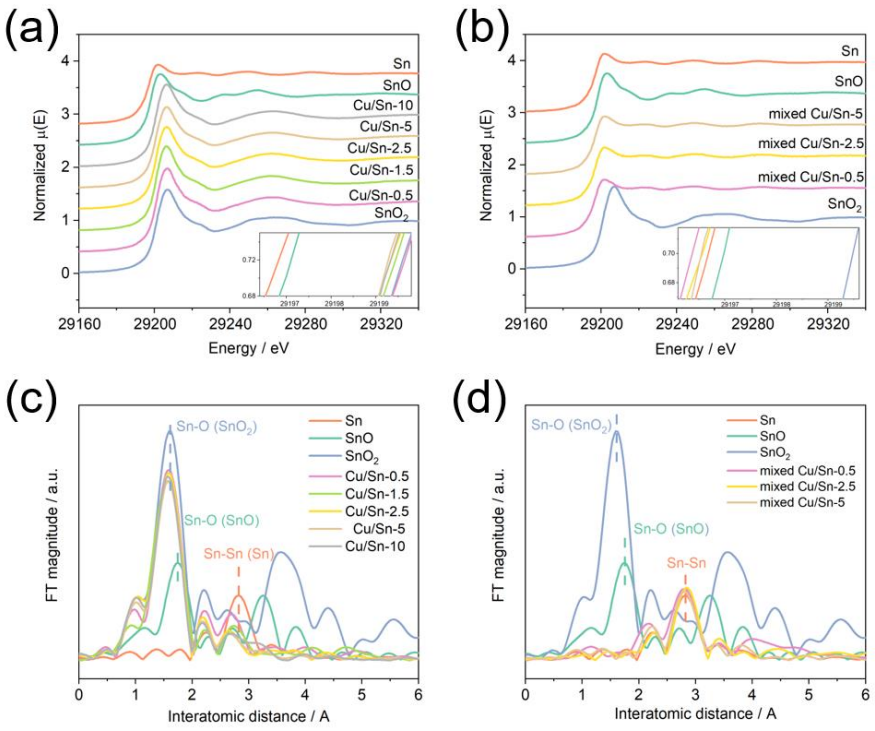

Figure 3-6. Normalized Sn K-edge XANES (a, b) and k^3-weighted Fourier transform EXAFS (FT-EXAFS) spectra. (a, c) Cu/Sn catalysts and (b, d) physically-mixed Cu/Sn powders with different Sn contents.

These results are basically consistent with the reported EXAFS for Sn nanoclusters containing O and OH as anions.[179, 180] Taken together, the TEM and EXAFS results show that oxidized Sn nanoclusters were formed on Cu/Sn catalysts with a high Sn concentration. We speculate that a relatively higher Debye–Waller factor for a Cu/Sn catalyst with higher Sn loading is due to the low crystallinity of Sn nanoclusters on Cu nanoparticles. To confirm the Sn species in physically mixed Cu/Sn catalysts, we analyzed the Fourier-transformed EXAFS of those samples (Figure 3-6d). The peak assignable to Sn–Sn (2.9 nm) is clearly observed for physically mixed Cu/Sn catalysts. This result indicates that Sn species in physically mixed Cu/Sn catalysts dominantly exist as Sn(0), although the top surface might be partially oxidized by air.

	Bond type	CN	R	σ^2 ($\times 10^{-3}$, Å)	S_0^2
SnO_2	Sn-O	5.0	2.06±0.004	3.4±0.6	1.31
Cu/Sn-0.5	Sn-O	4.1	2.06±0.01	2.7±1.5	1.31
Cu/Sn-1.5	Sn-O	4.8	2.05±0.03	5.0±3.8	1.31
Cu/Sn-2.5	Sn-O	4.7	2.06±0.01	5.2±1.2	1.31
Cu/Sn-5	Sn-O	4.5	2.06±0.004	5.1±0.6	1.31
Cu/Sn-10	Sn-O	4.7	2.06±0.01	5.5±0.7	1.31

Table 3-2. Peak fitting of EXAFS spectra of SnO_2 as references and Cu/Sn catalysts. (Note: R: atomic distance (Å), CN: coordination number, σ^2: Debye–Waller factor. Amplitude Reduction Factor for all samples is set to 1.31, which are calculated by reference SnO_2. The curve fitting is conducted using R-space (range: 1−2.2 Å). Curve fitting for the EXAFS spectra was conducted by using ARTEMIS software.[169])

On the basis of the aforementioned XRD, STEM–EDX, and XPS results, we explain the electronic states and morphology of the Sn atoms on Cu/Cu_2O nanoparticles as follows. At low Sn contents (less than 1.5%), most of the Sn atoms are atomically dispersed, with a valence state of IV. As for the as-prepared samples, atomically dispersed oxidized Sn atoms would be grafted onto Cu_xO layers with O or OH ligands.[181, 182] As the Sn ratio increases (greater than 1.5%), oxidized Sn nanoclusters might be formed on the Cu/Cu_2O nanoparticles, and the Sn 3d peaks shift toward the positive energy region. Finally, when the Sn ratio reaches 10%, most of the Sn is aggregated as oxidized Sn nanoclusters.

3.3.2 CO_2 electrolysis performance of Cu/Sn catalysts

The CO_2 reduction behavior was investigated using a homemade three-compartment cell with the GDEs carrying the Cu/Sn catalysts (Figure 2-1a and 3-1b). Cyclic voltammetry (CV) curves of the Cu/Sn electrode are compared with those of bare Cu catalysts (without Sn modification) in a 0.5 M KCl electrolyte solution under continuous CO_2 supply conditions (Figure 3-7a). Although the onset potential of the cathodic currents was approximately −0.38 V versus RHE, little difference was observed in the onset potentials among the Sn-decorated Cu samples with molar ratios between 1.5% and 5% and the bare Cu sample. The Cu/Sn-0.5 and -10 samples

exhibited slightly more positive (−0.25 V vs RHE) and slightly more negative (−0.47 V vs RHE) onset potentials, respectively, than the other Cu/Sn-*x* samples.

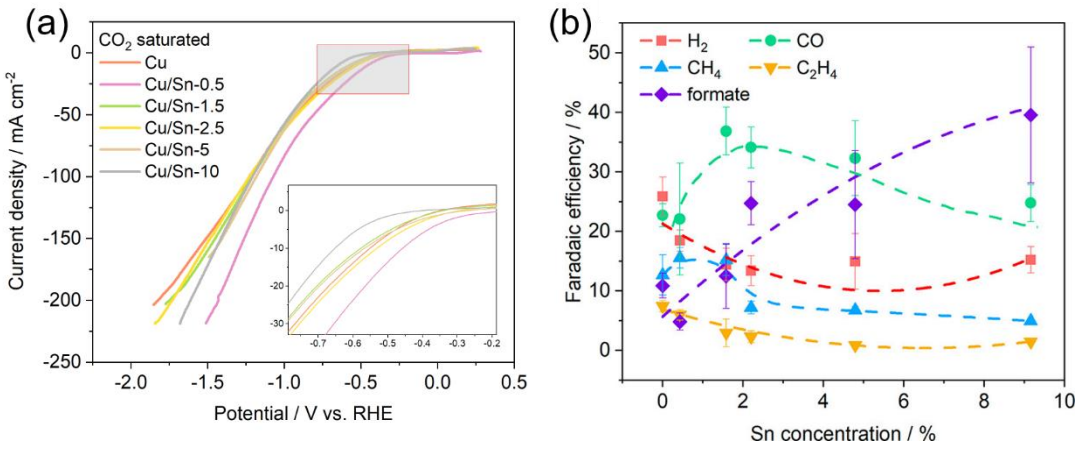

Figure 3-7. (a) CV scan curves of Cu and Cu/Sn catalysts (contents of Sn = 0.5, 1.5, 2.5, 5, 10%) modified GDE under CO_2 atmosphere (scan rate = 100 mV s^{-1}); (b) FEs of gaseous product and formate after 1 h of CO_2RR testing with different Sn contents (result based on ICP-OES analysis) under a constant current density of 200 mA cm^{-2}.

We next analyzed the products of the CO_2RR carried out under galvanostatic conditions (j = 200 mA cm^{-2}). The FEs of the reduction products are shown in Figure 3-7b. The FEs of H_2 as the product of proton reduction reactions decreased to less than 15% upon the addition of just 1.5% Sn atoms, whereas the FE of bare Cu nanoparticles was ~25%. Focusing on gaseous CO_2RR products, we found that the amount of CO, which has been reported elsewhere to be the main product obtained with most Cu/Sn alloy catalysts,[160] clearly increased when Cu was modified with a trace amount of Sn (<5%). Notably, the sum of the FEs for hydrocarbons (CH_4 and C_2H_4) showed almost no decay for the Cu/Sn-0.5 and -1.5 samples when compared with the sum of the FEs for bare Cu nanoparticles. In particular, the FE of CH_4

formation increased for the Cu/Sn-0.5 and -1.5 samples. When the Sn content was greater than 5%, the main product was HCOOH. The FE for HCOOH formation for the Cu/Sn-10 catalyst reached 40%.

	Capacity / μF	Surface roughness factor
Cu	0.037	1.00
Cu/Sn-0.5	0.046	1.24
Cu/Sn-1.5	0.052	1.42
Cu/Sn-2.5	0.032	0.87
Cu/Sn-5	0.036	0.97
Cu/Sn-10	0.036	0.97

Table 3-3. The double-layer capacities and surface roughness factors measured using CVs.

We also discuss the roughness factor of the electrodes and turnover frequency (TOF) in Table 3-3 and Figure 3-8. We must note here that the reaction surface using GDEs is the triple-phase interface, and thus, it is quite difficult to accurately evaluate the electrochemical surface area. As just a reference, the roughness factor of the GDEs with Cu/Sn catalysts are estimated by CVs with different scan rates. The capacitance values differ between samples (*i.e.*, 0.032 mF for Cu/Sn-2.5 and 0.052 for Cu/Sn-1.5). The TOF result shows that Cu/Sn catalysts with a doping level of 1.5 or 2.5 show the highest TOF_{CO} of ~140 h^{-1}. However, we again note that it is difficult to estimate the active Cu sites, and thus, these values are definitely underestimated because we assume that all Cu is active for CO_2RR in this calculation.

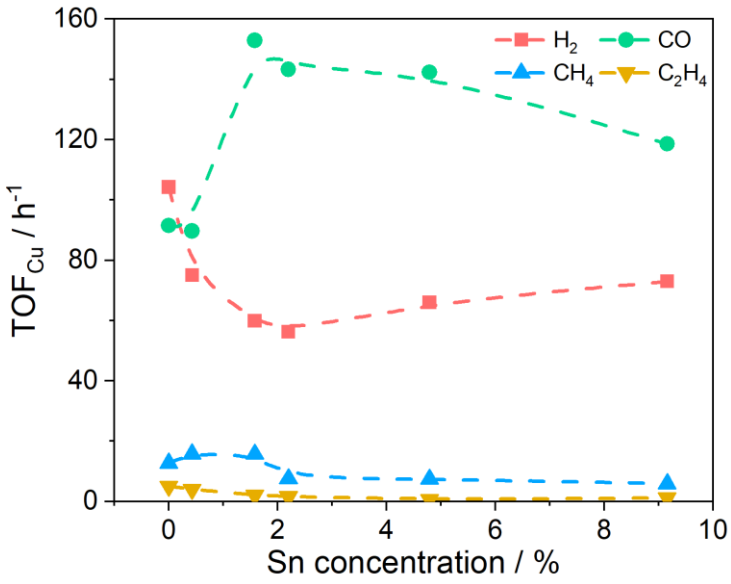

Figure 3-8. TOF of main products (H_2, CO, CH_4 and C_2H_4) for sysnthesized Cu/Sn catalysts in this study.

The CO_2RR potential dependence for the bare Cu and Cu/Sn catalysts is shown in Figure 3-9. Parts a, c, and e of Figure 3-9 indicate that Sn modification suppressed H_2 evolution over the full range of examined potentials. With respect to the partial current density of various products (Figure 3-9b, d, f), the H_2 partial current density decreased to approximately -12.4 mA cm^{-2} from -41.7 mA cm^{-2} under a potential of -1.25 V versus RHE upon modification of the Cu nanoparticles with 1.5% Sn. The current density of CH_4 reached -27.5 mA cm^{-2} at a potential of -1.25 V versus RHE for Cu/Sn-1.5. Notably, it has been reported that Cu_xO can be reduced at −0.3 V versus RHE. Therefore, the Cu surfaces are reduced to Cu(0) during CO_2RR electrolysis.[183, 184] In addition to Cu, the oxidative Sn atoms are also known to be easily reduced to Sn(0) at about −0.3 V versus RHE.[185, 186] Therefore, both oxidized

Cu and Sn atoms in the as-prepared samples are instantaneously reduced to metallic states with zero valences during CO_2RR electrolysis.

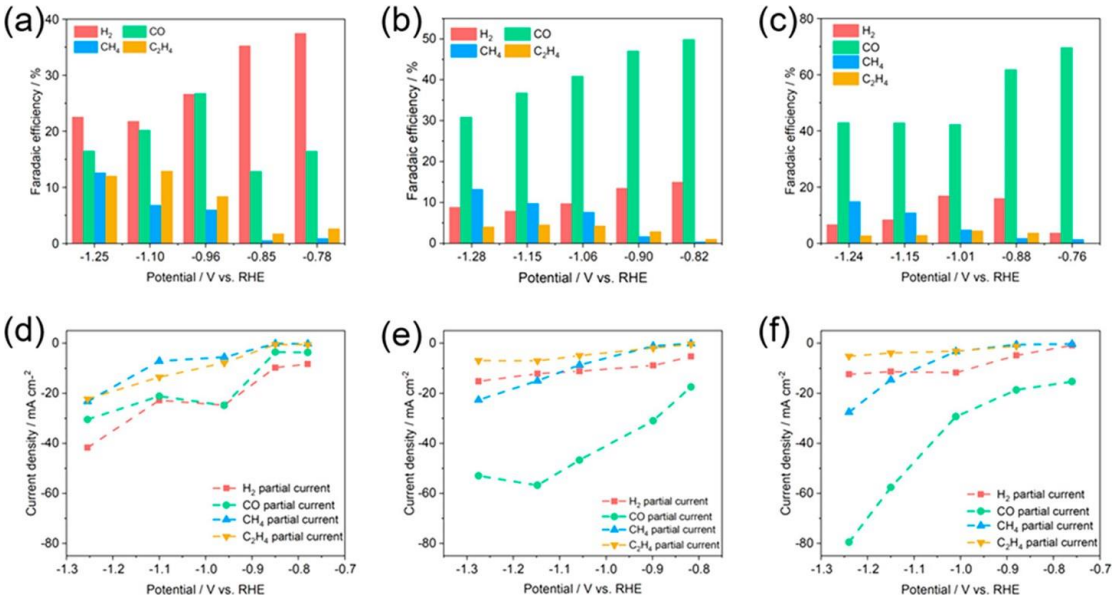

Figure 3-9. FEs and partial current densities of the CO_2RR products after 30 min of testing on Cu (a, d), Cu/Sn-0.5 (b, e), and Cu/Sn-1.5 (c, f) loading GDE-based cells under different potentials.

Next, we conducted stability tests of Cu/Sn-0.5 and -1.5 catalysts at a constant current of 200 mA cm^{-2}. The FEs for H_2 and CO generation were almost constant, and thus the doping effect of a trace amount of Sn to Cu particles was maintained for 6 h (Figure 3-10). These results suggest that our Sn-decorated Cu catalysts were stable enough to discuss the effect of Sn doping within this time scale. Figure 3-11 shows the XAS analyses for Cu/Sn catalysts after electrolysis. Although no obvious change in the spectra was observed for Sn atoms by electrolysis, we could not exclude the effect of air oxidation after electrolysis. Thus, analysis of the electronic states of Cu and Sn by operando XAFS measurement is an essential future work.

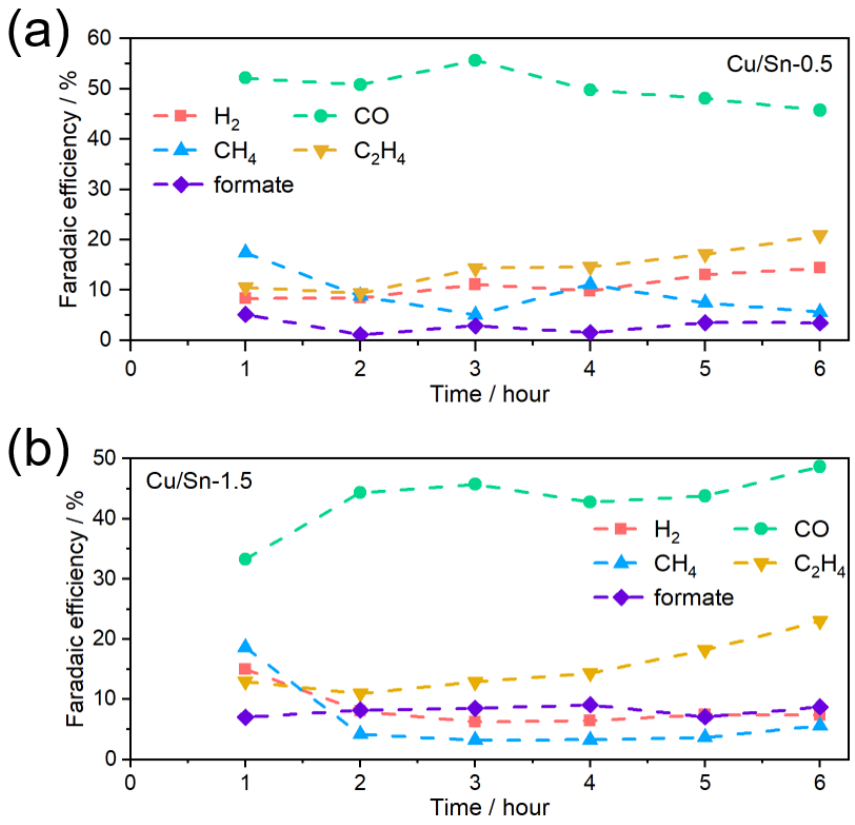

Figure 3-10. Stability test (6 hours) of Cu/Sn-0.5 (a) and Cu/Sn-1.5 (b) catalysts modified GDE under a constant current density of 200 mA cm^{-2}. The products were sampled for each hour.

To be specific, The Sn K-edge XANES spectra revealed that the valence state of Sn is similar to SnO_2 or SnO after electrolysis. No obvious peaks assignable Sn(0) or Sn-oxides particles are observed in Sn K-edge FT-EXAFS spectra (Figure 3-11b). This result implies that no critical change of Sn species occurs during electrolysis for Cu/Sn-0.5 and Cu/Sn-1.5. The Figure 3-11c revealed that the valence states of Cu of those samples on electrodes after electrolysis are the mixture of Cu^{1+} and Cu^0. Many previous reports revealed that Cu particles are reduced from Cu^{2+} or

Cu^{1+} to Cu^0 during electrolysis at the cathodic potential in our study. Thus, we assume that our electrodes were partially re-oxidized by air after electrolysis.

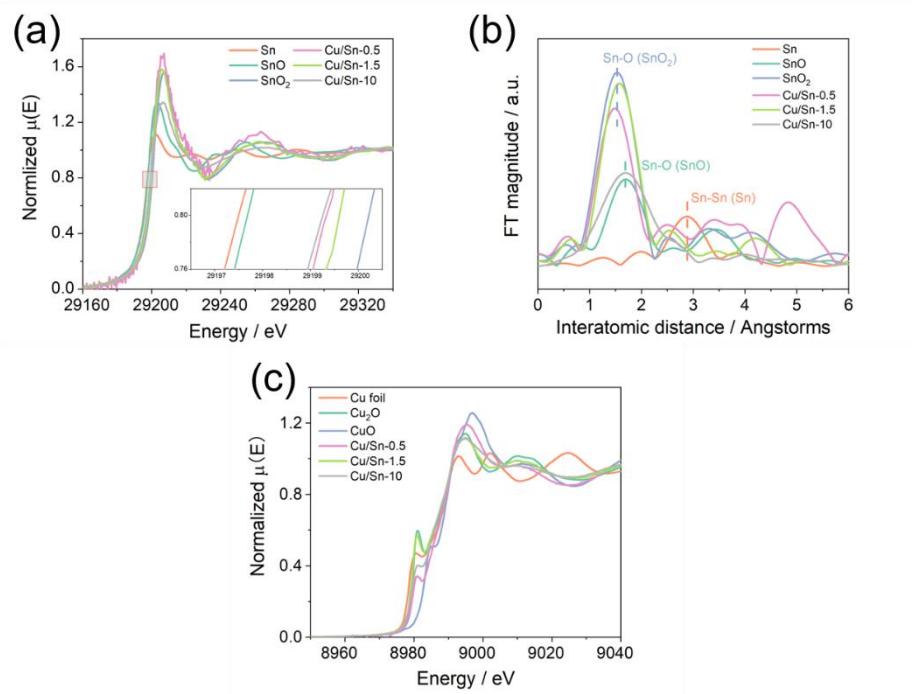

Figure 3-11. Representative Sn K-edge XANES (a) and FT-EXAFS spectra (b) after electrolysis of Cu/Sn-0.5, 1.5 and 10. (c) corresponding Cu K-edge XANES spectra after electrolysis.

We also tested the CO_2RR performance using physically mixed Cu/Sn samples as reference samples with the same molar ratios (Sn % = 0.5, 1.5, 2.5, 5, and 10; Figure 3-12). As expected, the physically mixed Cu/Sn samples exhibited almost no change in the product composition when the Sn content was low. Thus, modification with Sn atoms played a critical role in suppressing H_2 formation and enhancing CO generation.

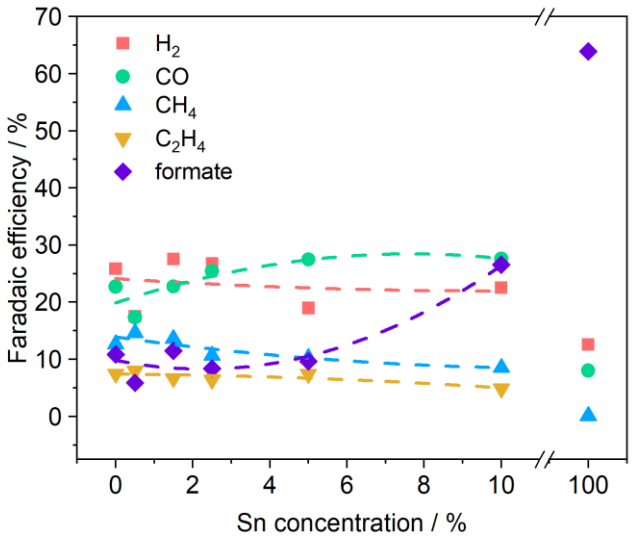

Figure 3-12. FEs of gaseous product after 1h CO_2RR testing using Sn and physically-mixed Cu/Sn catalysts with different Sn content (0.5, 1.5, 2.5, 5, 10%) under constant 200 mA cm^{-2} current density.

3.3.3 DFT analyses of the position of Sn atoms and the catalytic mechanism

As shown in Figures 3-7b and 3-9, at low Sn contents (less than 1.5%), the FE of the HER was suppressed to approximately half of that with bare Cu nanoparticles, resulting in an increase of the FE of the CO_2RR to CO. Here, we consider the mechanism underlying these unique catalytic activities. To verify the details of the catalytic mechanism, the structure and location of Sn atoms should first be identified. The STEM results show that the Sn atoms were atomically dispersed in the as-prepared catalysts with trace Sn contents. However, as mentioned above, Cu_xO and the oxidized Sn atoms were reduced to the metallic state under CO_2RR experiments.

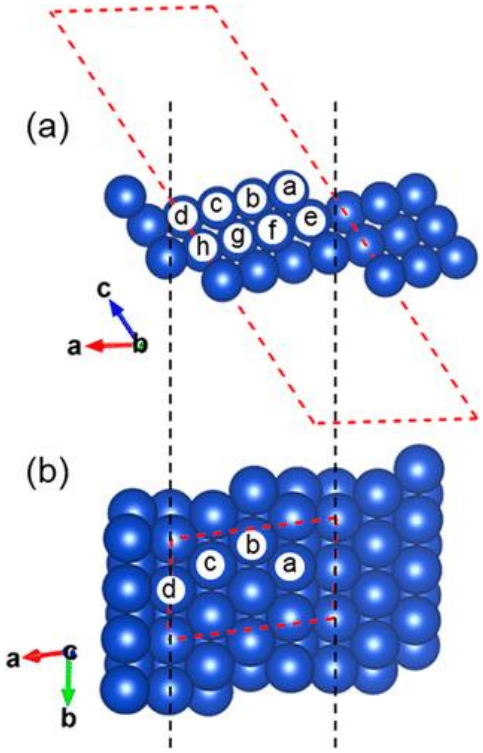

Figure 3-13. Structure of three layer of Cu(533) employed for the calculation of E_{stab}: (a) side view; (b) top view. The letters a-h represent the substitution of Sn atoms. The stabilized structure are shown in Figure 3-14.

Thus, we next attempted to investigate where the Sn atoms are located in the Cu/Sn catalysts during electrolysis using stabilization energy (E_{stab}) analyses via DFT calculations.[160, 187] In the present work, the Cu(553) facet was adopted as the model structure because the structure possesses both coordinatively saturated and unsaturated sites. We calculated E_{stab} for eight different positions of Sn atoms in Cu(553), as shown in Figure 3-13.

Figure 3-14 shows the structures after relaxation for four Sn-substituted Cu(533). In Table 3-4, we list E_{stab} values for the Sn atoms in Sn-substituted Cu(553) using the value for the Sn atom substituted into a low-coordinated site (site a) as a standard (for details of the calculations, see the 3.2.5 section). The E_{stab}

value of a Sn atom substituted into the low-coordinated site (site a in Figure 3-13) of the Cu was 0.25-0.37 eV smaller (more stable) than that of a Sn atom substituted into the first layer of saturated Cu sites on the surface (sites b–d in Figure 3-13). Thus, Sn atoms exist more stably on unsaturated sites of Cu nanoparticles than on saturated sites. In addition, the Sn atoms in the second layer of Cu(553) (sites e–h) are much more unstable than those in the first layer. These DFT calculation results reveal that Sn atoms tend to preferentially locate at low-coordinated surface sites of the Cu nanoparticles.

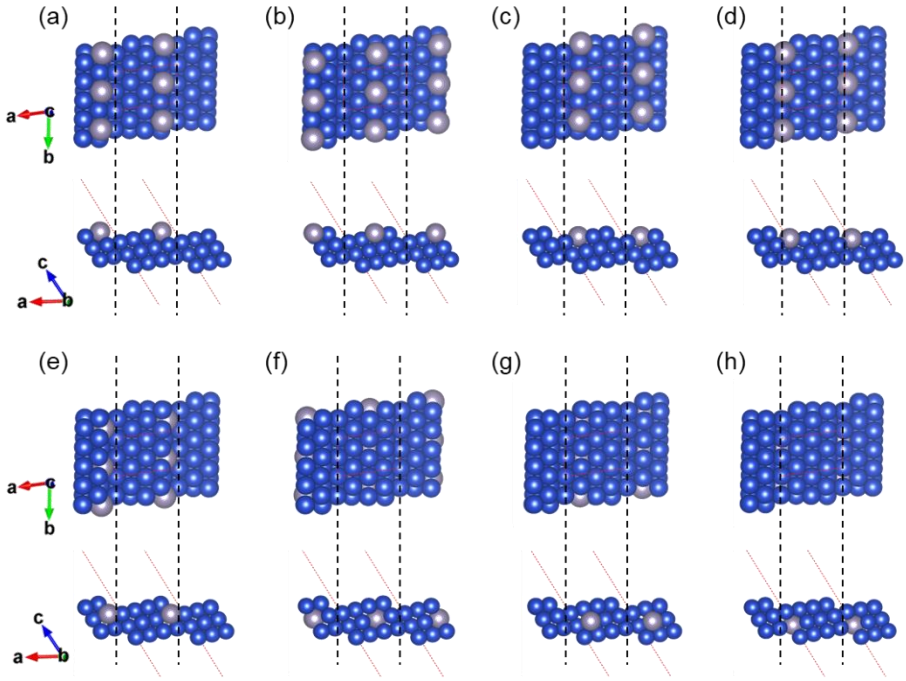

Figure 3-14. The structures of Sn-substituted Cu(533) after relaxation. Red dashed lines represented the unit cell. Blue: Cu and silver: Sn. Top figures for top view and bottom figures for side view of the stabilized structure. (a) - (h) figure represent the corresponding site with the same label as described in the text.

structure (first layer)	E_{stab}/eV	structure (second layer)	E_{stab}/eV
site a (unsaturated)	0	site e	0.87
site b (saturated)	0.35	site f	1.52
site c (saturated)	0.25	site g	1.47
site d (saturated)	0.27	site h	1.12

Table 3-4. Stabilization energy (E_{stab}) of different Sn-atom-decorated locations on Cu(533) crystal facet, as modeled via DFT calculation.

Next, DFT analyses were performed for CO_2 reduction to CO, which is the intermediate of CH_4 and C_2H_4, and for the HER. For calculation of the adsorption energies, Cu(100) and Cu(211) were adopted as the model structures of clean flat surface and low-coordinated Cu sites, respectively (Figure 3-15). We calculated the adsorption energies of the intermediates on the Cu atoms of bare Cu(100) and Cu(211) and on the Cu and Sn atoms of Sn-doped Cu(211), which are denoted as Cu@Cu/Sn and Sn@Cu/Sn, respectively. First, we investigated the HER activities for the four adsorption sites by obtaining the corresponding Gibbs free energy diagram (Figure 3-16a). The bare Cu(100) and Cu(211) facets show H* formation energies of 0.50 and 0.004 eV, respectively. These results indicate that the HER at the low-coordinated Cu sites [Cu(211)] is more favorable than that at the saturated sites [Cu(100)]. Interestingly, the Sn atom on Cu(211) (Sn@Cu/Sn) shows a H* formation energy of 0.71 eV. This result indicates that H* adsorption onto Sn atoms is endergonic and that atomically dispersed Sn sites cannot function as active centers for the HER because of weak interaction with H*, consistent with previous reports. In addition, a low-coordinated Cu site in Cu/Sn (Cu@Cu/Sn) exhibited a H* formation

energy of −0.1 eV. This result indicates that the rate-determining step for the HER at Cu@Cu/Sn became the desorption of H_2 molecules and that modification of Sn decreased the HER activity on the neighboring Cu sites.

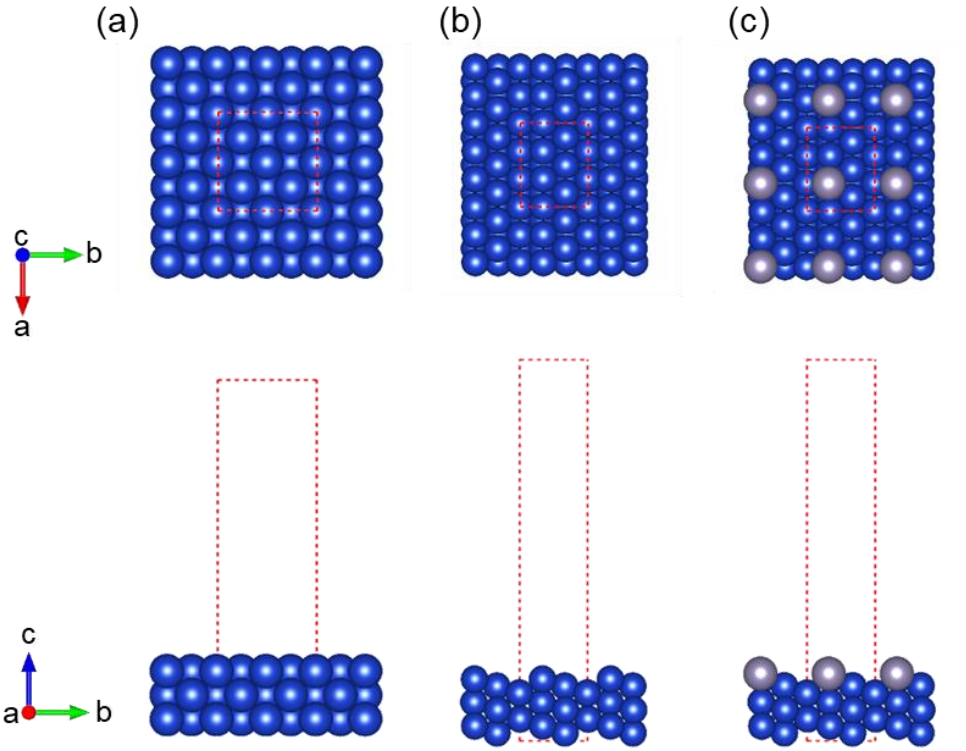

Figure 3-15. The structure of (a) Cu(100), (b) Cu(211) and (c) Sn doped Cu(211). Top column for top view and bottom column for side view.

We next investigated the CO_2RR for CO generation at the low-coordinated sites. The formation energies of the CO_2RR intermediates for CO generation at −0.8 V versus CHE are shown in Figure 3-16b. The reaction free energies are summarized in Table 3-5. The CO desorption barriers (ΔG_{CO}) for Cu(211), Cu@Cu/Sn, and Sn@Cu/Sn (less than ~0.2 eV) are certainly lower than those for the reported materials suffering from CO poisoning.[188, 189] Besides, the generation of CO molecules from the adsorbed COOH* is thermodynamically favorable by more than 1

eV. In this case, CO poisoning effects are known not to be serious.[189] Thus, the rate-determining step would not be CO desorption but the formation of COOH*. The formation energy of COOH* (ΔG_{COOH}) is almost 0 eV on the low-coordinated sites of bare Cu(211); this formation energy is the lowest value among the four investigated adsorption sites. The ΔG_{COOH} values on Cu@Cu/Sn and Sn@Cu/Sn are 0.08 and 0.64 eV, respectively. Therefore, not only the CO generation activity on Sn sites but also that on neighboring Cu sites is suppressed by the modification of low-coordinated Cu sites with Sn atoms, which is similar to our findings related to the HER.

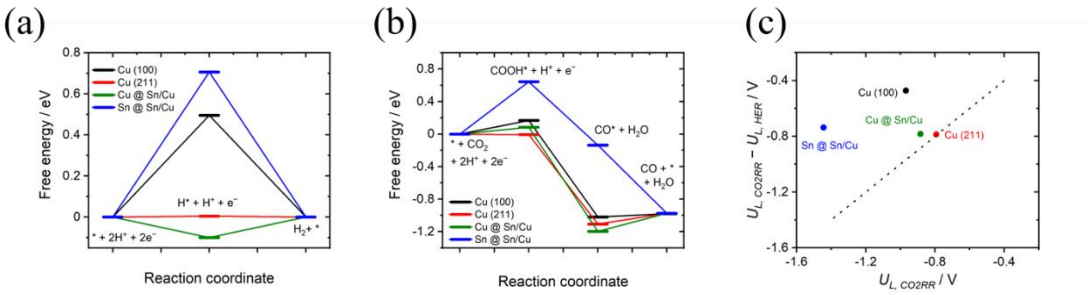

Figure 3-16. Binding-energy diagram of key intermediates on different facets of Cu crystals and stable decorated Cu-based catalysts of the HER (a) and CO_2RR to CO (b) reaction pathways. (c) Limiting potential for CO_2RR ($U_{L,\,CO2RR}$) – HER ($U_{L,\,HER}$) plotted against $U_{L,\,CO2RR}$. Larger values of $U_{L,\,CO2RR}$ (*x* axis) represent greater CO_2RR activity, and larger values of $U_{L,\,CO2RR} - U_{L,\,HER}$ (*y* axis) represent greater CO_2RR selectivity over the HER.

To understand the selectivity between the HER and CO_2RR, we plotted the limiting potential of CO_2RR for CO generation ($U_{L,\,CO2RR}$, which corresponds to the limiting potential of COOH* formation in the present study) and the HER ($U_{L,\,HER}$) in Figure 3-16c. The authors of the previous reports[46, 190] used $U_{L,\,CO2RR} - U_{L,\,HER}$ as a

descriptor of the selectivity of CO_2RR over HER; thus, a more positive value for $U_{L,\ CO2RR} - U_{L,\ HER}$ indicates greater selectivity for the CO_2RR. The values of $U_{L,\ CO2RR} - U_{L,\ HER}$ for the Cu(100) and Cu(211) surfaces are −0.47 and −0.79 V, respectively, indicating that the CO_2RR selectivity on the coordinatively saturated Cu sites on the Cu(100) facet is greater than that on the low-coordinated sites on the Cu(211) facet. This consideration is consistent with the previous experimental results related to Cu nanoparticles. The $U_{L,\ CO2RR} - U_{L,\ HER}$ values for Cu@Cu/Sn and Sn@Cu/Sn are −0.78 and −0.74 V, respectively, indicating that the selectivity between the CO_2RR and HER on Sn-modified Cu sites is approximately the same as that on bare Cu(211) (−0.79 V).

	Reaction free energy (eV)			
Reaction step	Cu(100)	Cu(211)	Cu@Cu/Sn	Sn@Cu/Sn
1. $CO_2 + * + e^- + H^+ \rightarrow COOH*$	0.17	−0.01	0.08	0.64
2. $COOH* + e^- + H^+ \rightarrow CO* + H_2O$	−1.19	−1.10	−1.28	−0.78
3. $CO* \rightarrow CO + *$	0.04	0.13	0.22	−0.84

Table 3-5. Difference of free energies (ΔG) between each reaction steps in Figure 3-16. The potential is -0.8 V vs. CHE.

3.4 Summary of the dependence of the HER and CO_2RR activity on Sn amounts

On the basis of the aforementioned DFT calculations, the mechanism responsible for the change in the FEs of the HER and CO_2RR upon Sn modification is summarized as follows (Figure 3-17). Both the HER and CO_2RR are more active at Cu atoms in unsaturated (*i.e.*, lower-coordination-number) sites, such as kinks, steps, and edge sites, than those in saturated (i.e., higher-coordination-number) sites, such as terrace sites, on pure Cu nanoparticles, as shown in Figure 3-16. In the case of Cu/Sn catalysts with a lower Sn content (less than 1.5%), some of the Cu atoms in low-coordinated sites are preferentially replaced by Sn atoms. Considering that Sn atoms served as the active centers for CO or HCOOH production in the previous papers,[191] the Sn sites would exhibit higher selectivity for the CO_2RR against HER. However, the DFT results indicated that the HER and CO_2RR activities at the low-coordinated sites modified with Sn atoms are lower than those at the site without modification. As a result, the activity of saturated Cu sites, where CO_2RR is more favorable than HER, is relatively emphasized with such lower contents (less than 1.5%). Importantly, the saturated Cu sites still remain and function as active centers for the further reduction reaction, leading to CO; thus, the FEs of CH_4 and C_2H_4 for Cu catalysts with trace amounts of Sn were approximately comparable to those for Cu nanoparticles.

Considering the DFT results and CO partial current density, an important question arose: although the DFT results suggested that both the HER and CO_2RR activity decreased by the substitution of Cu atoms by Sn atoms, why did the CO partial current density increase (Figure 3-9)? Not only CO_2RR but also HER produced

OH^-, and then OH^- reacted with the CO_2 substrate to electrochemically inert (bi)carbonates. Therefore, the HER at low-coordinated sites would decrease the CO_2 concentration at the catalytic surface, resulting in pure Cu showing a lower CO_2RR current density than Cu/Sn catalysts. Indeed, it has been reported that CO_2 absorption as carbonates by the local pH effect cannot be neglected under these high current conditions in neutral solutions using GDEs[192] (70% of the consumed CO_2 was absorbed as carbonates in the previous paper).

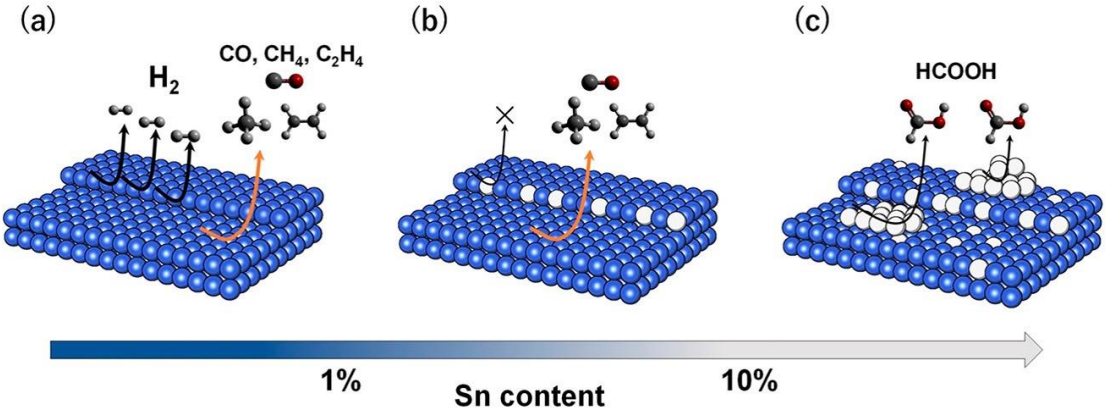

Figure 3-17. Illustration summarizing the selective modification of Sn on Cu nanoparticles and CO_2RR for (a) bare Cu and Cu/Sn catalysts with (b) low and (c) high Sn contents (blue, Cu; white, Sn).

When we further increased the Sn content (greater than 1.5%), Sn atoms were modified onto not only the unsaturated sites of Cu nanoparticles but also the saturated terrace sites or even formed oxidized Sn nanoclusters, as suggested in the TEM–EDX results in Figures 3-4l. The saturated Cu sites decorated with foreign metal atoms would not be active toward C_2H_4 and CH_4 production. Thus, increasing the Sn content to greater than 1.5% would decrease the FEs of hydrocarbon species such as CH_4 and C_2H_4. Oxidized Sn nanoclusters are known to generate HCOOH; thus, the Cu/Sn

catalysts with higher Sn loadings can more effectively produce HCOOH than pure Cu or Cu/Sn catalysts with a lower Sn content. As for the reported Sn-doped Cu catalysts, the Sn concentration is relatively high (>10%) compared with that of our catalysts. Therefore, even the coordinatively saturated Cu sites were likely substituted by Sn atoms, resulting in the production of only CO or HCOOH.

3.5 Conclusion

In this chapter, we prepared Cu catalysts with various molar ratios of Sn and confirmed the formation of different Sn moieties when the Sn content was varied. The Cu/Sn catalysts with a low Sn content (less than 1.5%) exhibited better CO_2RR selectivity, which led to higher FEs of CO production and almost the same FEs of hydrocarbon production. In particular, the Cu/Sn-1.5 sample showed a CH_4 partial current density of -27.5 mA cm^{-2} at -1.25 V versus RHE. DFT calculations confirmed that the Sn atoms preferentially decorated the low-coordinated sites of the Cu particles. The H_2 evolution biased unsaturated sites decorated with Sn atoms suppress the FEs of H_2 production, which is beneficial for the CO_2RR-active saturated Cu sites. We expect these results to provide guidance in the search for other effective CO_2RR catalysts by modifying Cu crystals with various elements at extremely low contents. In addition, this methodology could be applied generally to other metal nanoparticles with unique electrocatalytic properties.

Chapter IV Structural modulation of catalysts via direct electrodeposition on GDE

4.1 Introduction

As we mentioned in Chapter I, the rational morphological or structural design of catalysts for CO_2RR, especially for metallic catalysts, is also a common method to optimize the activity and selectivity. Up to date, many efforts have devoted to the various aspect of structural modulation, such as the particle size of nanoparticles,[82, 174, 193] exposed crystal facet,[150, 152, 194] pore size distribution[195] and so on, not only in single metal, but also the alloy[196, 197] or heterostructure.[161, 198] Among various effects, the crystal facet of various metallic catalysts, which possess different adsorption energy to the key intermediate, has been proven to be a vital role in the competition between CO_2RR and HER, and different reaction pathways of CO_2RR.[13, 90] For example, Qin *et al.* confirmed that Zn(101) facet favors the conversion of CO_2-to-CO, while Zn(002) prefers the HER. Thus, they successfully modulated the ratio of H_2 to CO in syngas via the regulated ratio of Zn(002) to Zn(101) through an electrodeposition method on Cu foam.[194] Based on the pioneering research of DFT calculation for the selectivity of C1 or C2 product from CO_2RR on different crystal facets of Cu electrode,[91, 92] Gregorio and co-workers demonstrated the facet-dependent selectivity via preparation of Cu spheres, Cu cubes and Cu octahedra, The Cu cubes with exposed facets of (100) exhibited high C_2H_4 selectivity of ~57% at 300

mA cm^{-2} current density, while the Cu octahedra with exposed facets of (100) showed the CH_4 selectivity of ~40% at the same condition.[152]

Direct electrodeposition on a conductive substrate, which involves the reduction of metallic ions in electrolytes and subsequent growth on a cathode surface, is an effective method to modulate the morphology of catalyst, especially for the porous structure.[199-202] Furthermore, unlike the traditional dip casting method, electrodeposition without the addictive ionomer, possesses better electronic and ionic contact within GDE.[203] The uniform catalyst layer exhibits the advantage in scale-up industrial application. Luo *et al.* electrodeposited the porous Zn layer on Cu mesh, and exhibited excellent selectivity of CO_2-to-CO conversion (FE = 95%) compared to the Zn foil.[204] To gain the porous structure, simultaneous H_2 bubbles production induced by hydrogen evolution with the metal ions reduction also succeed in the preparation of Ag foam preparation.[113] Besides the modulation of structure, the electrodeposition method offers a facile method to gain the alloy electrodes, although the different onset potential for different metal species could be a potential problem for the precise control of chemical composition. Lamaison *et al.* reported a high active Ag-alloyed Zn dendritic electrode via electrodeposition method on Zn plates. With optimized Ag content, porosity, thickness, and surface area, the CO_2-to-CO selectivity reached 91% and sustained above an average of 90% over 40 h in an H-type cell. Moreover, to overcome the mass transport limitation due to the low solubility of CO_2 in aqueous solution, they applied high-pressure CO_2 (up to 9.5 bar) allowed the CO production of up to -286 mA cm^{-2}.[205] And suppose we could direct electrodeposition of catalyst layer on carbon paper and applied in a GDE-based cell. In that case, we could combine the advantages of facile modulation of morphology and chemical

composition from electrodeposition method and sufficient CO_2 supply from a gas-phase feed in GDE-based cell, expecting a better performance via a simple way.

Based on above discussion, electrodeposition metallic catalyst direct on the surface of GDE boosts the various morphology with porous structure or exposed crystal facet of single metal or alloy. Here, we prepared different CO_2RR catalysts based on the GDE via electrodeposition method with varied morphology and chemical composition, and presented different activity of CO_2 electrolysis test.

4.2 Experimental section

4.2.1 Chemicals

Zinc(II) sulfate, anhydrous ($ZnSO_4$, 95%), silver (I) nitrate ($AgNO_3$, 99.8%), hexadecyl trimethyl ammonium bromide (CTAB, 98%), sulfuric acid (H_2SO_4, 95%), potassium bicarbonate ($KHCO_3$, 99%) and potassium chloride (KCl, 98%) were purchased from Wako Pure Chemical. All chemicals were directly used for experiments without any further purification. Carbon paper with a gas diffusion layer (Sigracet 38BC and 34BC) and Nafion membranes were obtained from SGL carbon and Sigma-Aldrich, respectively. Ultrapure water from a Mill-Q system (18.2 MΩ cm) was used for all preparation and electrochemical tests.

4.2.2 Electrodeposition method and characterization

The electrodeposition process was conducted using an electrochemical workstation (HZ-5000, Hokuto Denko) in a conventional three-electrode cell configuration. The carbon paper is covered by Kapton tape on one side and the exposed area for deposition on the other side is 0.5×0.5 cm^2. Dilute 2 M H_2SO_4 used as the supporting electrolyte,[113, 205] $ZnSO_4$ and $AgNO_3$ used as Zn and Ag precursors,

respectively. Depending on the condition, modulating the concentration of H_2SO_4 (1, 2, 3 M) and the molar ratio of metal ions with the constant total amount to 0.2 M. To control the morphology, adding the CTAB (1, 2, 3 mM) as the surfactants in electrolytes.[194] For another method, electrolytes containing 95g/L $Cu_2P_2O_7$, 420 g/L $K_4P_2O_7$ with 3 mL/L $NH_3•H_2O$ to modulate the pH to 8.8. The electrodeposition was conducted under galvanostatic mode with a continuous or pulsed direct current at room temperature and ambient pressure. Specific parameters were introduced in 4.3 section.

XRD, XPS, SEM and SEM-EDX were characterized as Chapter II and III, please refer to the 2.2.3 and 3.2.3 sections.

4.2.3 CO_2 electrolysis and product analysis

The as-prepared GDEs via electrodeposition were directly used in the CO_2RR electrochemical test without further process or annealing in a vacuum oven at 180 ℃ to remove the residual surfactants. Electrochemical measurements were performed using the same device (electrochemical station, mass flow controller) and cell as Chapter III. The electrolyte using in the section is 0.5M $KHCO_3$ with better buffer capability or 0.5M KCl, which is more beneficial for CO_2RR, and would be described in the Result section. The CO_2RR products were sampled after 30 mins or an hour of electrolysis in different tests.

The gas and liquid products were also analyzed as the previous description, except for an additional GC-MS (Nexis GC-2030, Shimadzu, Japan).

4.3 Results and Discussion

4.3.1 porous Zn and Ag/Zn electrodeposition on GDE

We researched the relation between catalyst morphology and variable parameters of electrodeposition process, including applied current, deposited time and the concentration of protons, *etc.* Under same deposited time (10 s), with increasing applied current density, the deposited Zn layer using the electrolyte of 0.2M $ZnSO_4$, and 1.5M H_2SO_4, changed from irregular nano- or microstructure to a cube-like structure about 1-2 μm in size (Figure 4-1). And with higher applied current density (-4 A cm^{-2}), the thin sheets grown on the surface of cubic structure also became more evident (Figure 4-1i).

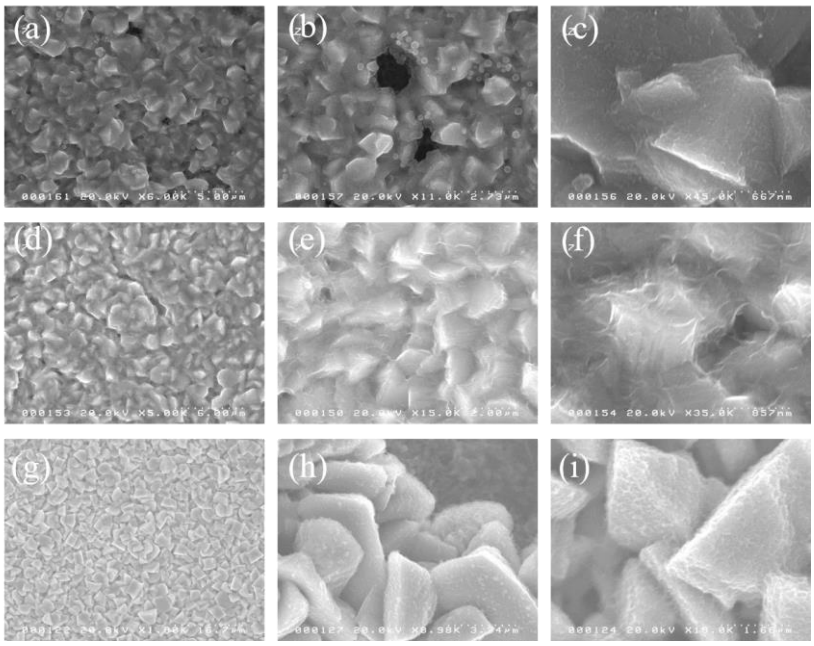

Figure 4-1. SEM images of GDEs with electrodeposited Zn layer of same time (10 s) and varied current density at different magnifications, (a-c) j = -2 A cm^{-2}, (d-f) j = -3 A cm^{-2}, (g-i) j = -4 A cm^{-2}.

Based on the result, we selected the j = -4 A cm^{-2} as the applied current density, SEM images of deposited Zn layer under the current density with different time (10, 15 and 30 s) are displayed in Figure 4-2. With longer deposition time, the thickness of the cubic structure became thicker, and transferred to a multilayer stacking morphology, and the small sheets on the surface also disappeared. When the deposition time increased to 30 s, the porous structure started to present.

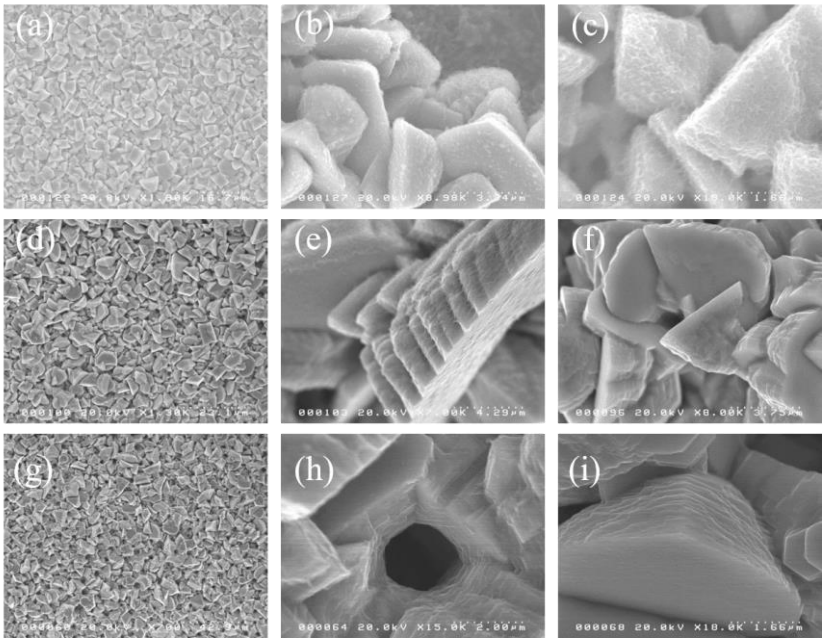

Figure 4-2. SEM images of GDEs with deposited Zn layer with same applied current density (-4 A cm^{-2}) but different time: (a-c) 10s, (e-f) 15s and (g-i) 30s.

The porous structure induced by the H_2 bubbles from hydrogen evolution simultaneously occurs on the cathode, and the rate and amount of H_2 bubbles production have a solid connection to the proton concentration. Thus, we increased the concentration of H_2SO_4 in electrolytes to expect the distinct porous structure of the deposited layer. As Figure 4-3 shown, the applied current density and time kept the same as the Figure 4-2a-c, when the concentration of H_2SO_4 was 2 M (Figure 4-

3a-c), the randomly stacking cubic structure became more uniform, while the exposed sheets on the surface as Figure 4-2a-c shown have disappeared. When the concentration of H_2SO_4 further risen to 3 M, the cubic structure had been destroyed and shifted to the nanosheets stacking nanosphere, the size was around 1 μm.

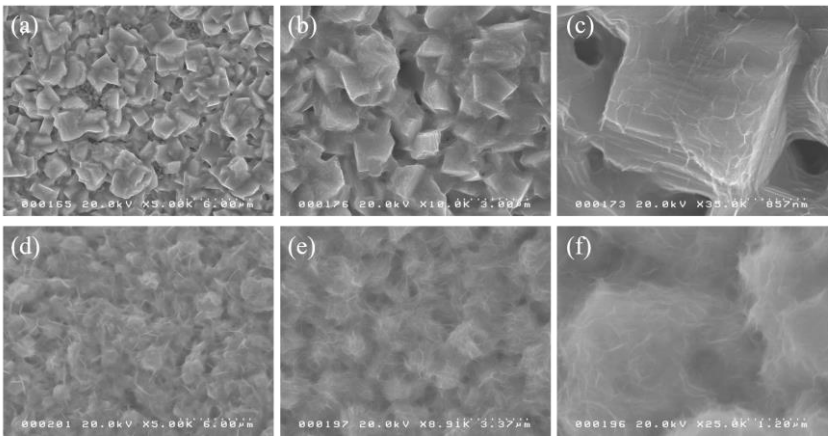

Figure 4-3. SEM images of GDE with deposited Zn layer under j = -4 A cm^{-2} and 10s deposition time in the electrolyte with 0.2 M $ZnSO_4$ and different concentration of H_2SO_4: (a-c) 2 M; (d-f) 3 M.

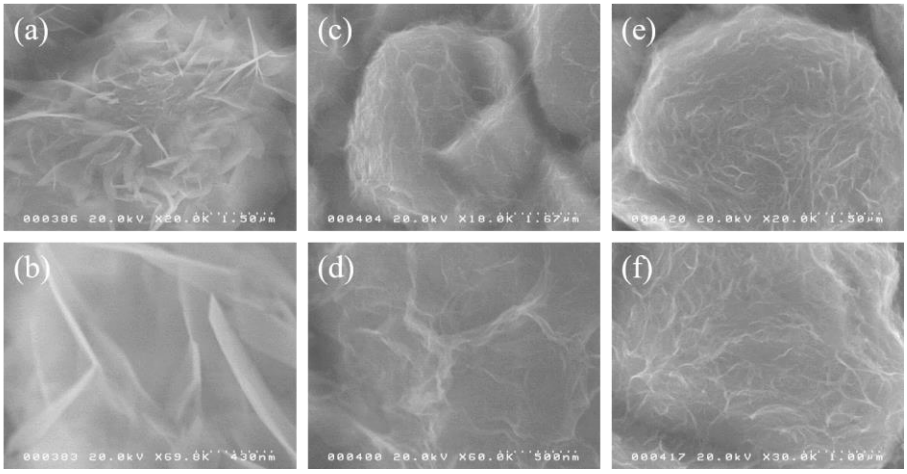

Figure 4-4. SEM images of GDEs with deposited Zn layer applied different pulse deposition mode using the electrolyte of 0.2 M $ZnSO_4$, 3 M H_2SO_4, and controlled the

sum of on-time to 30 s, Ic = -4 A cm^{-2}. (a, b) t_{on} = 0.25 s, t_{off} = 0.25s; (c, d) t_{on} = 0.25 s, t_{off} = 0.5s; (e, f) t_{on} = 0.5 s, t_{off} = 1s.

Compared with the continuous current, the pulse deposition significantly balances the concentration between the depleted region, such as edges and corners, and the bulk electrolyte, leading an elevated limiting current density.[203, 206] A typical current mode for pulse deposition, consisting of a cathodic current (on-time) and a relaxation period (off-time). The cathodic current (I_c), on-time (t_{on}), off-time (t_{off}), cycle numbers are used to precisely control the electrodeposition process. Figure 4-4 shows the SEM images of GDEs with the same j and the amount of t_{on} under different modes of pulse deposition. With the same t_{on} and t_{off} as well as the high frequency of shift (Figure 4-4a, b), the deposited Zn layer exhibited longer extended nanosheets on the surface, may be attributed by the high frequency of relaxation period, which provided the growth time in a single orientation.

To further clarify the structural difference of GDEs prepared by different deposition modes, we handled the XRD pattern tests to investigate the crystal phase and orientation of different samples. We also prepared Zn nanoparticles (denoted as Zn NPs below) via the wet-chemical reduction method as chapter III for comparison, then dip-coated on the GDE. Figure 4-5a indicated the main phase in Zn NPs is ZnO, while Figure 4-5b presented the main phase in four electrodeposited Zn samples is all metallic Zn. The ZnO phase of Zn NPs would reduce to metallic Zn under the negative potential,[207, 208] thus, the main phase effective in CO_2RR is the same of wet-chemical method or electrodeposition prepared samples. We introduced the texture coefficient (Tc) here to quantitatively compare the crystal facet ratio calculated via the following equation:

$$Texture\ coefficient_{(hkl)} = \frac{I_{(hkl)}/I_{0(hkl)}}{\sum_{i=1}^{n} I_{(hkl)n}/I_{0(hkl)n}} \times 100\% \qquad (4\text{-}1)^{[194]}$$

where $I_{(hkl)}$ is the intensity of (hkl) facet from the XRD analysis result of different samples, the $I_{0(hkl)}$ is the standard intensity of (hkl) facet from Zn #PDF 04-083, and the n is the numbers of diffraction peaks calculated here (n = 6), which has labeled in Figure 4-5b, and the calculated result represented in Figure 4-5c. Zn(002) crystal facet favors the HER, while (101) prefers the CO_2RR as in previous studies. The pulse deposited samples of t_{on} = 0.5s, t_{off} = 1s showed a higher ratio of (002) facet and a lower percentage of (100) facet compared with the continuous deposition samples. The results indicated that the GDEs with Zn layer under continuous current process would be more beneficial for the CO_2 electrolysis.

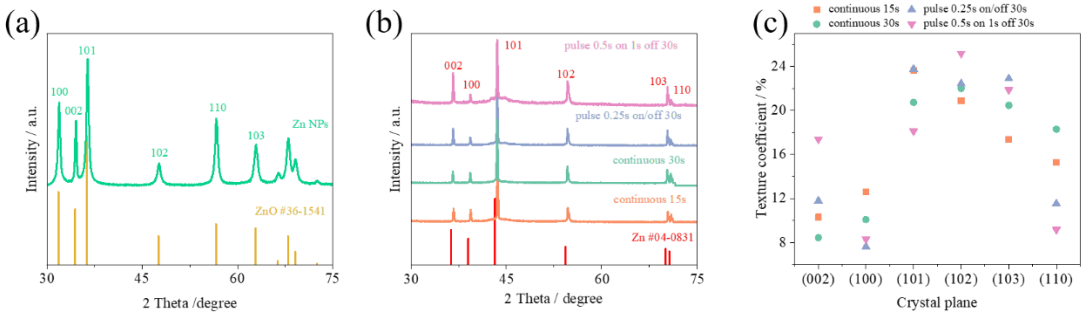

Figure 4-5. XRD patterns of Zn NPs (a) and the electrodeposited Zn (b). Calculated texture coefficient of electrodeposited Zn (c). Yellow and red bars indicate the standard peaks of ZnO and Zn, respectively.

To confirm our assumption of the CO_2RR performance using Zn NPs coated and different deposited GDEs as catalysts, we conducted the CO_2RR test using a three-compartment cell in the conjunction with three electrodes as the description in chapter II and III. Figure 4-6 showed the FEs of H_2, CO and formate and the total

current densities, as well as the partial current densities of each product using the Zn NPs coated GDE and electrodeposited Zn-based GDEs applied continuous current with different time as the working electrodes. In all Zn electrodes, with higher applied potential, the activity toward H_2 increased and suppressed the activity toward the conversion of CO_2-to-CO. The FE of CO using electrodeposited Zn electrodes was higher in less negative potential (-2.5 V vs. Ag/AgCl), then tended to almost same at more negative potential. Although they showed no significant difference in FEs, the current densities increased to 3-4 times compared with the Zn NPs electrode. For the continuous deposited sample of 30 s (Figure 4-6c), the CO partial current density at -2.5 V vs. Ag/AgCl reached 107.7 mA cm^{-2} with nearly 80% FE under ambient pressure.

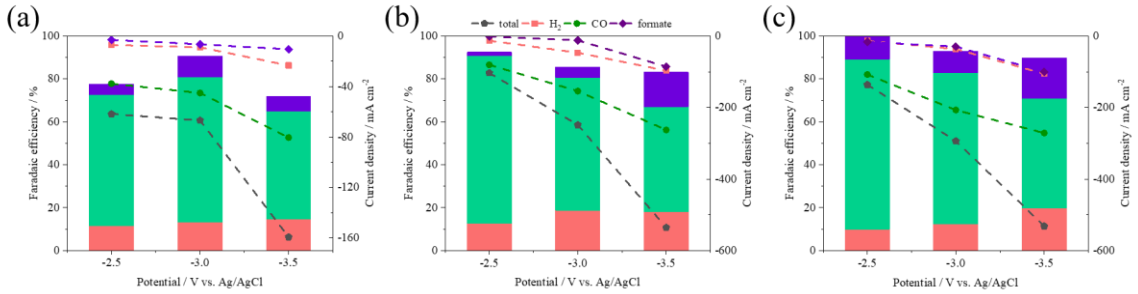

Figure 4-6. FE (stacking bars) and current density (line + scatters) of Zn NPs (a), continuous deposited Zn of 15 s (b) and 30 s (c) after 1 h CO_2 electrolysis in 0.5 M KCl electrolytes.

As for the Zn-based GDE prepared via the pulse deposition mode, the FE and current density as represented in Figure 4-7. We noted here, considering the poor buffer capability of 0.5 M KCl electrolytes, the pH increased a lot after 1 h electrolysis test, leading the electrodeposited layer to seriously peeled off. Thus, we changed the electrolytes to 0.5 M $KHCO_3$ as a buffer solution and narrowed the

potential range with higher CO_2RR activity. Although the current density of pulse deposited Zn electrodes kept the same range as the continuously deposited samples, the FE of H_2 increased a lot, which accorded with the analysis of texture coefficient, leading a direction to optimize the structure of catalysts.

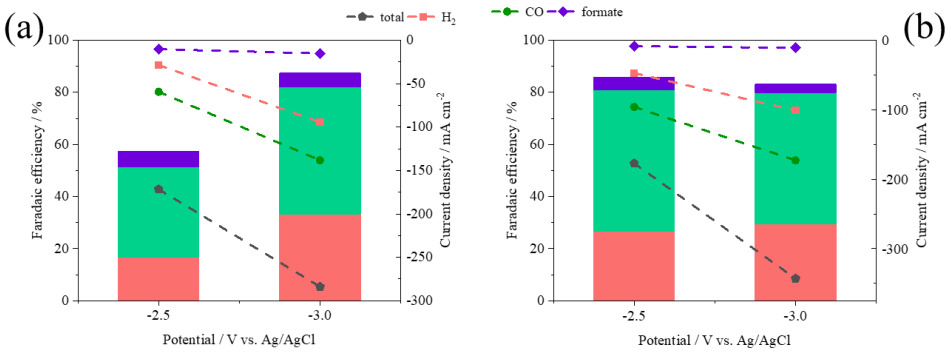

Figure 4-7. FEs and current densities of Zn deposited GDEs via different pulse mode with same amount of deposition time (30s) after 1 h CO_2 electrolysis in 0.5 M $KHCO_3$ electrolytes. (a) t_{on} = 0.25 s, t_{off} = 0.25s; (b) t_{on} = 0.5 s, t_{off} = 1s.

We added the H_2SO_4 in the electrolytes as the supplier of protons to produce H_2 bubbles, generating the porous structure. However, the porous structure is absent in most deposited GDEs. To create a porous structure and improve the CO_2RR performance, we added the 5% atomic ratio of $AgNO_3$ as Ag precursors to gain Ag/Zn bimetallic layer deposited GDE. The morphology of deposited Ag/Zn modified GDE observed by SEM as shown in Figure 4-8, exhibiting apparent irregular porous structure, whether inside the pore or on the surface, the sheet extended to various direction, and exhibited a flower-like structure.

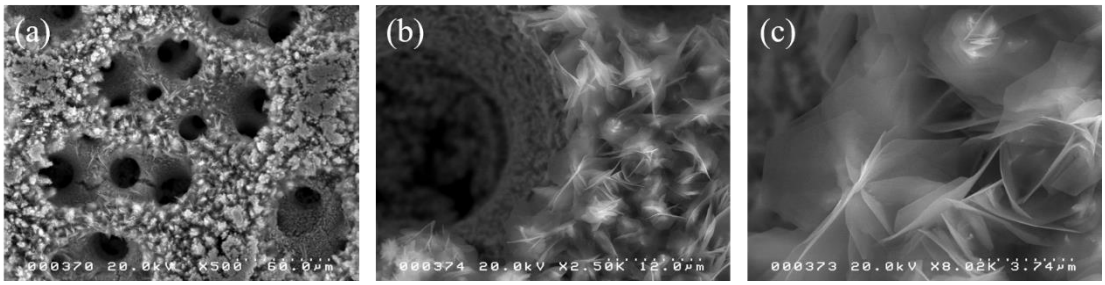

Figure 4-8. SEM images of electrodeposited Ag/Zn modified GDE at different magnifications (atomic ratio of Ag is 5%).

About the CO_2RR performance of Ag/Zn alloy, the CV curves (Figure 4-9a) under Ar or CO_2 atmosphere showed the preferred CO_2RR tendency in wide range potential. And for the quantitative analysis of CO_2RR, the CO partial current density arrived at -286.6 mA cm^{-2} with 81 % FE at -3.0 V vs. Ag/AgCl at ambient pressure. By introducing the GDE, the CO partial current density is comparable to the cited paper in a more convenient method, without a high pressure of CO_2 (9.5 bar).[205]

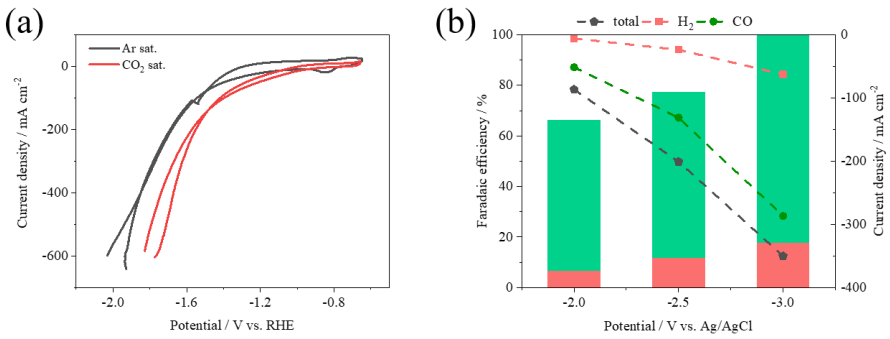

Figure 4-9. CV curves under Ar and CO_2 atmosphere (a), FEs and current densities (b) using Ag/Zn deposited GDE in 0.5M KCl electrolytes. Scan rate: 20 mV s^{-1}.

4.3.2 Zn electrodeposition with oriented modulation

From the results of above section, it is hard to fabricate porous structure via reduction of single Zn ions with the simultaneous H_2 bubbles production, one of the

possible reasons is the fast elimination of bubbles. Thus, we considered adding CTAB, a common surfactant, in the electrolytes to stabilize the as-prepared bubbles, leading a porous structure. Besides, the formation of Zn layer on GDE could be divided into two stages, the nucleation and growth phase. The more negative potential induced the more nucleated sites on the surface of GDE, and the moderate potential is more suitable for the crystal growth in a single orientation. For the pulse deposition mode, the different elapsed time of two potential stages would affect the morphology and crystal orientation of the as-prepared catalyst layer. We set two modes for pulse deposition of two potential U_1 and U_2 (V vs. Ag/Ag) and the duration time of two potential t_1 and t_2 with the same amount of deposition time. Figure 4-10 showed the morphology of the deposited Zn layer on GDE using two different pulse modes with an additional 1 mM CTAB in the electrolytes. Two samples exhibited porous structures, with the more negative potential of U_2, the pore size distribution tended to a higher ratio of smaller size, and the Zn sheet tended to be more random, unlike the cross-linked sheet structure of less negative potential (Figure 4-10c).

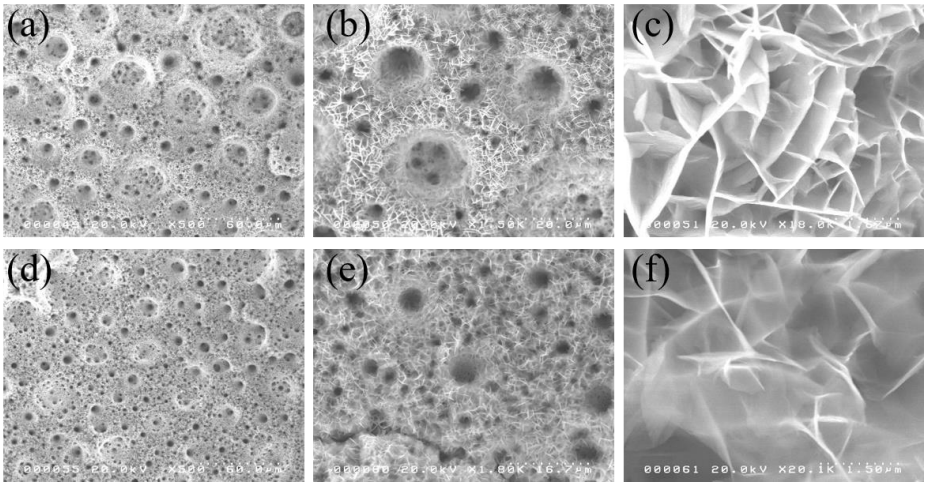

Figure 4-10. SEM images of deposited Zn layer on GDEs using two pulse modes at different magnifications. (a-c) U_1 = 3.0 V, t_1 = 2 s, U_2 = 3.5 V, t_2 = 2 s; (d-f) U_1 = 3.0 V, t_1 = 2 s, U_2 = 4.5 V, t_2 = 2 s.

And the structural analysis of these two samples via XRD is shown in Figure 4-11, as well as the calculated texture coefficient as the above description compared with the sample without CTAB addition. With the CTAB adding in electrolytes, the only detectable phase was still metallic Zn. For the texture coefficient, the crystal ratio of (002), (102) and (103) decreased a lot compared with the sample without CTAB, while the percentage of (100), (110) increased, which represented different preferred orientation with and without CTAB. Regarding the active facet for conversion of CO_2-to-CO, Tc of (101) facet fluctuate in a narrow range, suggesting the close performance of CO_2RR test.

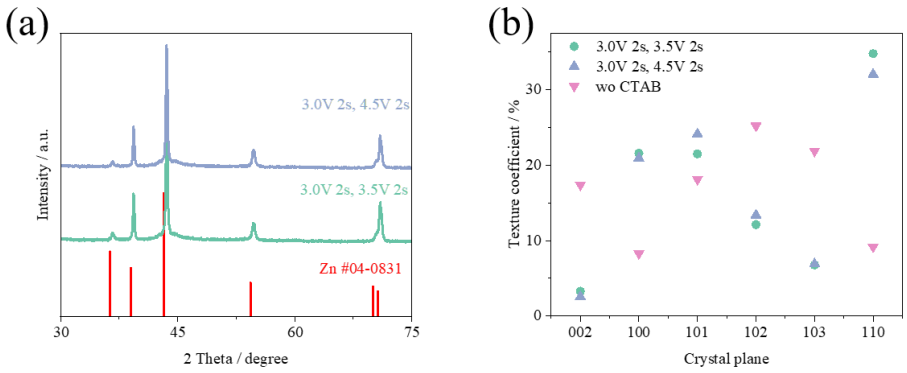

Figure 4-11. (a) XRD patterns of two electrodeposited GDE in different pulse modes using the electrolyte with 1 mM as surfactant and (b) the corresponding texture coefficient compared with the sample without CTAB. Red bars indicate the standard peaks of Zn.

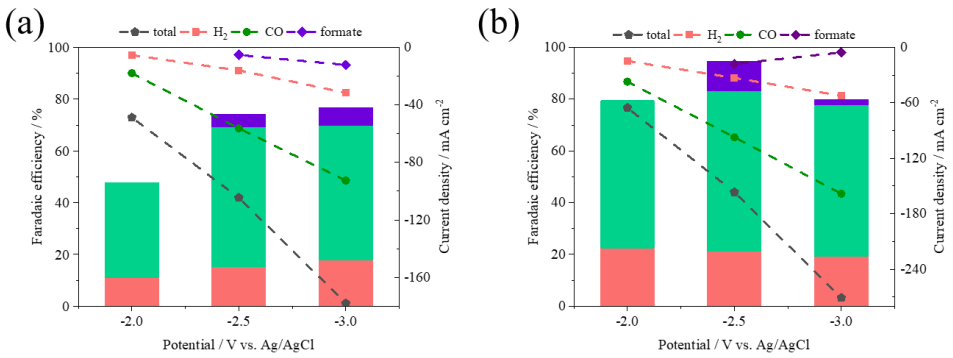

Figure 4-12. Faradaic efficiencies of H_2 and CO and the current densities of two electrodeposited Zn modified GDE after 30 min CO_2 electrolysis. (a) U_1 = 3.0 V, t_1 = 2 s, U_2 = 3.5 V, t_2 = 2 s; (b) U_1 = 3.0 V, t_1 = 2 s, U_2 = 4.5 V, t_2 = 2 s.

The FEs and current densities of two samples of CO_2 measurements are represented in Figure 4-12. The FEs of H_2 slightly increased compared with the sample without CTAB, and the current densities also declined. The worse performance of CTAB-assisted deposited samples may be attributed to the impact from other crystal facets, which needs to be further researched.

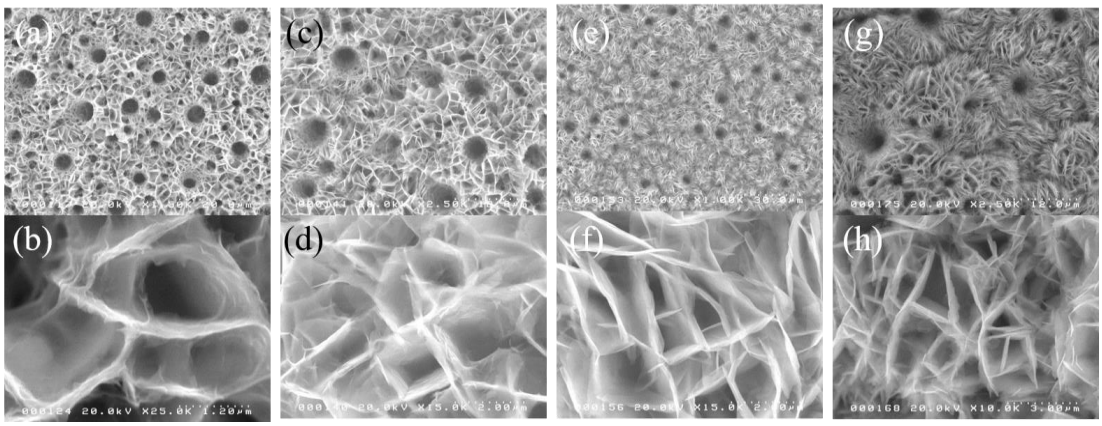

Figure 4-13. SEM images of #1-#4 samples prepared by electrodeposition Zn in same electrolytes at different magnifications. (a, b): #1; (c, d): #2; (e, f): #3; (g, h): #4.

To further investigate the relationship between the morphology and the pulse deposition mode, we fabricated the CTAB-assisted electrodeposited Zn with controlled potential of negative potential for nucleation, and slowly decreased the second potential and extended the duration time (labeled as #1-#4, U_1 = 4.5 V, t_1 = 2 s in previous three samples, and #1: U_2 = 3.0 V, t_2 = 4 s; #2: U_2 = 2.5 V, t_2 = 6 s; #3: U_2 = 2.0 V, t_2 = 8 s; #4: U_1 = 4.5 V, t_1 = 1 s, U_2 = 2.0 V, t_1 = 9 s). The morphologies of different samples were characterized by SEM, the #4 sample prepared via longer duration time for crystal growth exhibited a cross-linked structure composed by denser parallel sheets (Figure 4-13g).

We also measured the XRD patterns and calculated the corresponding Tc of #1-#4 samples presented in Figure 4-14. They showed similar orientation based on the results of Tc, and #1 exhibited a slightly higher ratio of (110) facet, while the #4 sample presented a higher percentage of (101) facet. And the CO_2RR performances of #1 and #4 sample, which prepared via two extreme pulse modes, are shown in Figure 4-15, and the potential has transferred to RHE scale based on the pH of electrolytes and *iR* compensation. Two samples showed similar FE of H_2 production, while different trends for CO_2 reduction: #1 preferred the conversion of CO_2-to-CO, while #4 favored the reduction of CO_2 to formate with a maximum FE of 36.8%. Thus the modulation of crystal orientation not only tunes the ratio of gas product based on the competition between HER and CO_2RR, but also affects the CO_2RR pathway, leading different distribution of CO_2RR product.

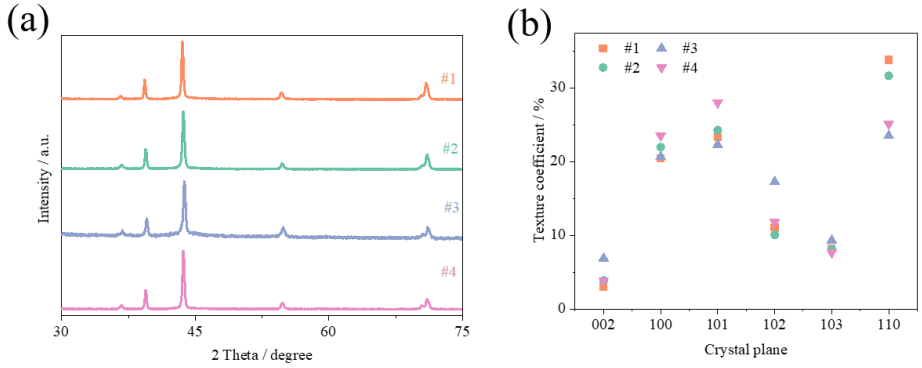

Figure 4-14. XRD patterns (a) and corresponding calculated Tc (b) of #1-#4 samples.

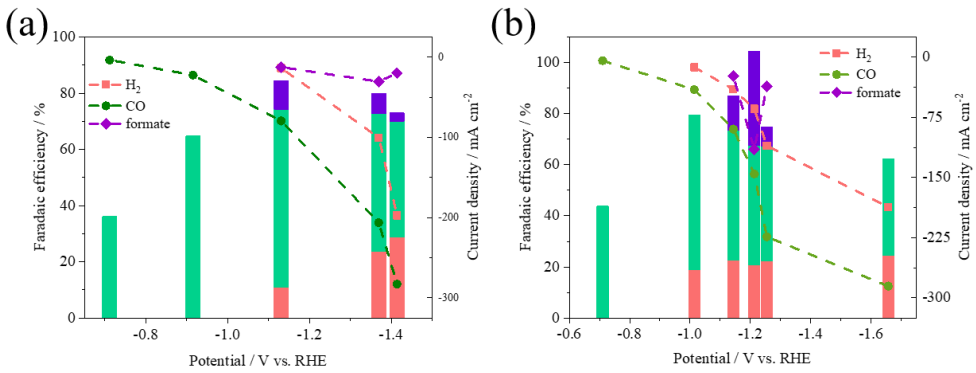

Figure 4-15. FEs and current densities of #1 (a) and #4 (b) samples under different potential after 30 min CO_2 electrolysis.

4.3.3 porous Cu on GDE

Unlike metal foils as substrates with good compatibility to the deposited metallic layer, one of the disadvantages of carbon paper substrate is the poor affinity. During the electrolysis test, due to the change of local condition and the stream transportation between gas and liquid side, the electrodeposited layer tends to peel off, leading the decay of catalytic performance. When we tried to prepare the porous Cu structure on GDE using H_2 bubbles production assisted method as above description, facing the problem of catalyst layer's peel off. To solve the problem, we

considered changing the electrolyte to pyrophosphate ($P_2O_7^{4-}$) based electrolyte, a common method for electrodeposition of Pb, Zn, Sn, Cu and their alloys in industrial application. Compared to the traditional cyanide electrolytes, the pyrophosphate-based electrolyte possesses several advantages, including non-toxic, economic properties, and no formation of oxide/hydroxide.[209, 210] In the other hand, the disadvantages of pyrophosphate method include the complex coordination structure between metal ions and $P_2O_7^{4-}$ ions, narrow window of the pH and P value (P_2O_7/Cu). We controlled the P value to 7.87 and pH to 8.8, prepared the Cu deposited GDE under different current densities and time.

Figure 4-16a represented the representative XRD patterns of GDEs with deposited Cu. The strong peaks at 26.7 and 54.8 º attributed by the graphite from the carbon paper, and the weak peaks at 42.9 and 50.9 º correspond to the (111) and (200) crystal facet of Cu, respectively. Compared to EDX analysis of the same sample (Figure 4-16b and Table 4-1), which indicates the atomic ratio of Cu exceeds 93%, the gap between intensity of XRD patterns and EDX analysis perhaps related to the amorphous phase of deposited Cu. The detected fluorine (F) element via EDX ascribed to the PTFE coating on GDE.

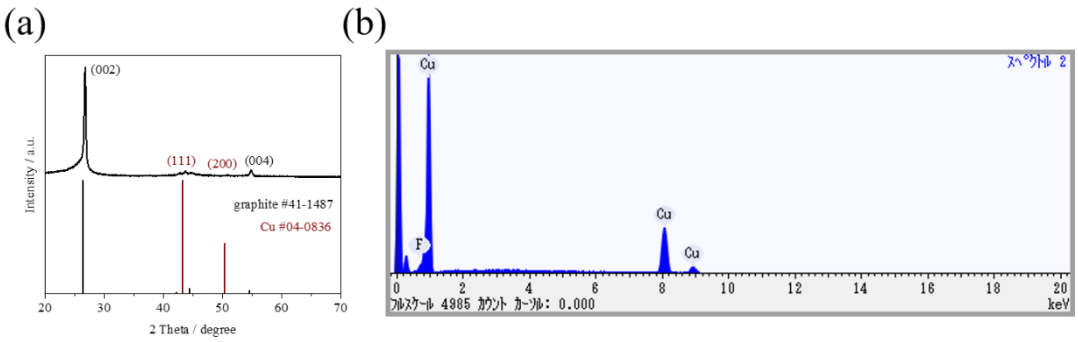

Figure 4-16. XRD patterns (a) and EDX analysis (b) of a representative GDE with

electrodeposited Cu using a pyrophosphate-based electrolyte. Black and red bars indicate the standard peaks of graphite and Cu, respectively.

Element	Weight%	Atomic%
F	1.984	6.342
Cu	98.016	93.658

Table 4-1. EDX analysis of the above sample.

Figure 4-17 represented the SEM images of Cu electrodeposited GDE after 5 min deposition with different applied current densities. When the current density was lower (-25 mA cm^{-2}), the deposited Cu exhibited a cotton-shaped structure, which is different with the cauliflower-like structure prepared via a larger current density (-40 mA cm^{-2}). The porous structure started to be observed when the current density further increased to -50 mA cm^{-2}, which also represented a smoother surface.

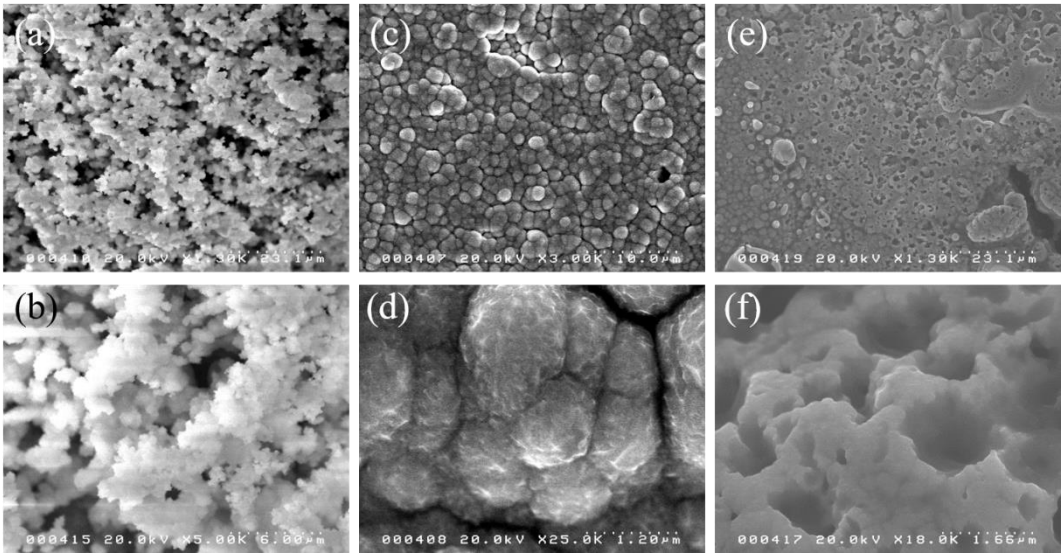

Figure 4-17. SEM images of Cu modified GDE after 5 min electrodeposition under different current densities. (a, b) -25 mA cm^{-2}; (c, d) -40 mA cm^{-2}; (e, f) -50 mA cm^{-2}.

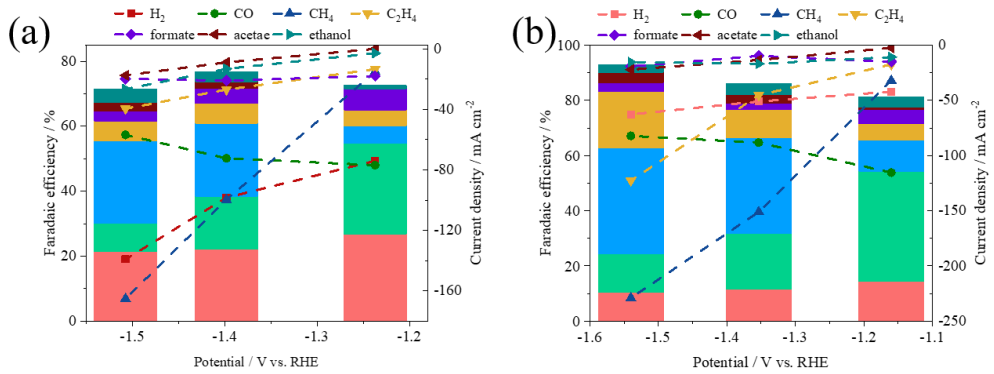

Figure 4-18. FEs and *j* of H_2 and products from CO_2RR after 30 mins test in 0.5 M KCl electrolytes using electrodeposited Cu GDE. (a) -40 mA cm^{-2}; (b) -50 mA cm^{-2}.

We also conducted the CO_2 electrolysis test to investigate the better morphology of the deposited Cu layer for CO_2RR. Figure 4-18 shows the FEs and current densities of gaseous and liquid product after 30 min test using 5 min electrodeposited Cu with -40 and -50 mA cm^{-2} current densities in 0.5 M KCl electrolytes. With larger current densities inducing porous structure, current density increased a lot compared with cauliflower-like structure, as well as the decreased FE of H_2, especially in the much negative potential range. For Cu-deposited electrode prepared using -50 mA cm^{-2} current density, the main products from CO_2RR changed from CO at the smaller potential to hydrocarbons (CH_4 and C_2H_4) at a more negative potential, especially for the CH_4, the FE and partial current density exceeded 38.3% and -229 mA cm^{-2}, respectively at -1.54 V vs. RHE. And the sum FE of hydrocarbons (CH_4 and C_2H_4) is also beyond 58.9%. Compared to the Cu deposited GDE prepared via the former method, the electrodeposited Cu layers electrodeposited using the pyrophosphate-based electrolytes show the better adhesive property to the GDE substrate.

4.4 Conclusion

In summary, we investigated the different parameters and the additives of catalysts' electrodeposition on gas diffusion electrode, and the impact for the final structures. H_2 bubbles induced by the H_2 evolution due to the acidic condition of electrolytes lead a porous structure of Zn and Ag/Zn alloy. And to further stable the bubbles to gain a more complicated porous structure, adding the CTAB as surfactant is also effective. As-prepared Zn deposited layers also showed a specific nanoflower-like structure with different preferred crystal orientations compared with Zn NPs, and affected by the parameters of the pulse-current program. By modulating the crystal facet ratio, not only the competition between CO_2RR and HER, the pathway of CO_2RR also regulated. For the low-affinity to GDE metal, Cu, the pyrophosphate-based electrolyte is capable of the porous structure on the GDE, and leading an increase of hydrocarbons production from CO_2RR. The facile method of direct electrodeposition is beneficial for the optimized structure and chemical composition of catalyst, and provides a possibility of large-scale production.

Chapter V General Conclusion and Prospect

In summary, we investigate various modified methods to suppress the competitive hydrogen evolution, which is inevitable during electrochemical CO_2 reduction in aqueous solution, including the electrolyzer and the optimized catalysts.

At first, we introduced the fundamental knowledge of CO_2 reduction, including the reaction pathway, evaluation system and the theoretical simulation method. We also summarized the classification of common catalysts and the corresponding optimized strategies as well as the design of electrolyzers.

In chapter II, we introduced the gas diffusion electrode in CO_2 reduction with a broader pH range of electrolytes compared with traditional plate electrodes. Using the same catalyst of Ni-doped CTF, coated GDE shows a preferred CO_2 activity in pH = 2 electrolytes, compared with a H_2 production dominated trend using a PE. The thinner diffusion layer close to the triple-phase interface of GDE induced the immediate consumption of protons in GDE with elevated local pH, and was confirmed by the Zn-related hydroxides sediments with additional Zn^{2+} ions in electrolytes on the surface of GDEs. These results provide more expansive space for the CO_2 reduction and the possible secondary reaction based on the products or intermediates from CO_2RR.

In chapter III, we change the spotlight to the optimization of catalysts based on the most common metallic catalyst, Cu. To hider the HER-active low-coordinated Cu sites, we decorated the Sn atoms with varied ratios, which is inactive for HER, on the Cu nanoparticles via a simple wet-chemical method. Physical and theoretical methods confirmed that the preferred site of Sn atoms is the unsaturated site when the

ratio is less than 1.5%. And the atomic-scale modification Sn presented suppression of hydrogen evolution and an increase of CO production compared with the pristine Cu nanoparticles. After Sn atomic modification, the catalysts showed lower activity both for the hydrogen evolution and CO_2 reduction via the first principle calculation of the adsorption strength of reaction intermediates. As a result, the activity of coordinatively-saturated Cu site, which shows favorable CO_2 reduction activity, was emphasized. The modification of trace foreign metal species in metal nanoparticles may provide an avenue for the synthesis of selective electrocatalysts for various target reactions.

And we combined the modification of catalyst and the direct electrodeposition on gas diffusion electrode. Direct electrodeposition on GDE surface shows many merits compared to the dip-coating of as-prepared catalyst powders on GDE, such as the better uniformity, the controllable fabrication of specific exposed active site or crystal facet and the possibility of porous structure with more channels for reactants delivery. We successfully deposited porous Cu and Zn layers directly on GDE surface via adding different surfactants in the electrolyte and applying pulsed current, and showed a much higher current density compared with the dip-coating samples. We also optimized the concentration of added surfactant and the program of pulsed current method to modulate specific crystal facets with favorable activity toward CO_2RR compared with HER. The direct electrodeposition method is beneficial to regulate and gain larger electrodes, which is a potential preparation method in scale-up industrial application.

However, the research of CO_2 reduction using electrochemical method still faces many problems and needs to advance further. About the application of gas

diffusion, although compared with the traditional H-type cell, it solved the problem of low current densities region and the small area of electrode. For the industrial application, the long-term stability at high current density cannot be ignored. Although, the PTFE layer increases the hydrophobicity of GDE, present GDE is still easy to face the problem of flooding during the CO_2 electrolysis tests. Up to now, there are many methods, including adding an additional layer of PTFE, modulating the ratio of PTFE and catalysts, optimizing the uniformity of deposited catalyst layer, but still need many efforts. And about our study in Chapter II, we explored the pH range to the acidic condition as low as 2, and the lower pH condition also needs to be investigated, as well as the possible candidate reaction, which could occur in this kind of acidic electrolytes.

As for the catalysts, considering the many possibilities of products and the close trigger potential, the ideal catalyst should show much more selectivity for a single product to simplify the purification procedure of products. It is hard to achieve the goal using a single catalyst, modulated alloy or heterostructure catalyst, which could keep the structural stability and catalytic activity in dozens, even hundreds of hours is urgently needed.

About the products, although there are papers about the multi-carbon products more than C3 products, the FE is still too low to discuss the meaning. Besides the single CO_2RR, using possible intermediates producing during CO_2RR pathway as precursors, combining with other organic reaction to bond longer C-C bond, even the C-N and C-S bond, to gain more complex product is also a promising field.

Reference

1. Falkowski, P.; Scholes, R. J.; Boyle, E.; Canadell, J.; Canfield, D.; Elser, J.; Gruber, N.; Hibbard, K.; Högberg, P.; Linder, S.; Mackenzie, F. T.; Moore Iii, B.; Pedersen, T.; Rosenthal, Y.; Seitzinger, S.; Smetacek, V.; Steffen, W., The Global Carbon Cycle: A Test of Our Knowledge of Earth as a System. *Science* **2000,** *290* (5490), 291.
2. Kim, D.; Sakimoto, K. K.; Hong, D.; Yang, P., Artificial Photosynthesis for Sustainable Fuel and Chemical Production. *Angew. Chem. Int. Ed.* **2015,** *54* (11), 3259-3266.
3. Windle, C. D.; Perutz, R. N., Advances in molecular photocatalytic and electrocatalytic CO_2 reduction. *Coord. Chem. Rev.* **2012,** *256* (21), 2562-2570.
4. Ross, M. B.; De Luna, P.; Li, Y.; Dinh, C.-T.; Kim, D.; Yang, P.; Sargent, E. H., Designing materials for electrochemical carbon dioxide recycling. *Nat. Catal.* **2019,** *2* (8), 648-658.
5. Hiragond, C. B.; Kim, H.; Lee, J.; Sorcar, S.; Erkey, C.; In, S.-I., Electrochemical CO_2 Reduction to CO Catalyzed by 2D Nanostructures. *Catalysts* **2020,** *10* (1), 98.
6. Zhu, D. D.; Liu, J. L.; Qiao, S. Z., Recent Advances in Inorganic Heterogeneous Electrocatalysts for Reduction of Carbon Dioxide. *Adv. Mater.* **2016,** *28* (18), 3423-3452.
7. Ren, W.; Zhao, C., Paths towards enhanced electrochemical CO_2 reduction. *Natl. Sci. Rev.* **2019,** *7* (1), 7-9.
8. Zhang, L.; Zhao, Z.-J.; Gong, J., Nanostructured Materials for Heterogeneous Electrocatalytic CO_2 Reduction and their Related Reaction Mechanisms. *Angew. Chem. Int. Ed.* **2017,** *56* (38), 11326-11353.
9. Zhao, X.; Du, L.; You, B.; Sun, Y., Integrated design for electrocatalytic carbon dioxide reduction. *Catal. Sci. Technol.* **2020,** *10* (9), 2711-2720.
10. Zhang, Y.; Guo, S.-X.; Zhang, X.; Bond, A. M.; Zhang, J., Mechanistic understanding of the electrocatalytic CO_2 reduction reaction – New developments based on advanced instrumental techniques. *Nano Today* **2020,** *31*, 100835.
11. Kortlever, R.; Shen, J.; Schouten, K. J. P.; Calle-Vallejo, F.; Koper, M. T. M., Catalysts and Reaction Pathways for the Electrochemical Reduction of Carbon Dioxide. *J. Phys. Chem. Lett.* **2015,** *6* (20), 4073-4082.
12. Birdja, Y. Y.; Pérez-Gallent, E.; Figueiredo, M. C.; Göttle, A. J.; Calle-Vallejo, F.; Koper, M. T. M., Advances and challenges in understanding the electrocatalytic conversion of carbon dioxide to fuels. *Nat. Energy* **2019,** *4* (9), 732-745.
13. Fan, L.; Xia, C.; Yang, F.; Wang, J.; Wang, H.; Lu, Y., Strategies in catalysts and electrolyzer design for electrochemical CO_2 reduction toward C2 products. *Sci. Adv.* **2020,** *6* (8), eaay3111.
14. Wang, G.; Chen, J.; Ding, Y.; Cai, P.; Yi, L.; Li, Y.; Tu, C.; Hou, Y.; Wen, Z.; Dai, L., Electrocatalysis for CO_2 conversion: from fundamentals to value-added products. *Chem. Soc. Rev.* **2021,** *50* (8), 4993-5061.

15. Liang, S.; Altaf, N.; Huang, L.; Gao, Y.; Wang, Q., Electrolytic cell design for electrochemical CO_2 reduction. *J. CO_2 Util.* **2020,** *35*, 90-105.
16. Zhang, X.; Guo, S. X.; Gandionco, K. A.; Bond, A. M.; Zhang, J., Electrocatalytic carbon dioxide reduction: from fundamental principles to catalyst design. *Mater. Today Adv.* **2020,** *7*, 100074.
17. Kibria, M. G.; Edwards, J. P.; Gabardo, C. M.; Dinh, C. T.; Seifitokaldani, A.; Sinton, D.; Sargent, E. H., Electrochemical CO_2 Reduction into Chemical Feedstocks: From Mechanistic Electrocatalysis Models to System Design. *Adv. Mater.* **2019,** *31* (31), 1807166.
18. Takeda, H.; Cometto, C.; Ishitani, O.; Robert, M., Electrons, Photons, Protons and Earth-Abundant Metal Complexes for Molecular Catalysis of CO_2 Reduction. *ACS Catal.* **2017,** *7* (1), 70-88.
19. Tian, Z.; Priest, C.; Chen, L., Recent Progress in the Theoretical Investigation of Electrocatalytic Reduction of CO_2. *Adv. Theory Simul.* **2018,** *1* (5), 1800004.
20. Rendón-Calle, A.; Builes, S.; Calle-Vallejo, F., A brief review of the computational modeling of CO_2 electroreduction on Cu electrodes. *Curr. Opin. Electrochem.* **2018,** *9*, 158-165.
21. Nørskov, J. K.; Rossmeisl, J.; Logadottir, A.; Lindqvist, L.; Kitchin, J. R.; Bligaard, T.; Jónsson, H., Origin of the Overpotential for Oxygen Reduction at a Fuel-Cell Cathode. *J. Phys. Chem. B* **2004,** *108* (46), 17886-17892.
22. Nørskov, J. K.; Bligaard, T.; Logadottir, A.; Kitchin, J. R.; Chen, J. G.; Pandelov, S.; Stimming, U., Trends in the Exchange Current for Hydrogen Evolution. *J. Electrochem. Soc.* **2005,** *152* (3), J23.
23. Gono, P.; Ambrosio, F.; Pasquarello, A., Effect of the Solvent on the Oxygen Evolution Reaction at the TiO_2–Water Interface. *J. Phys. Chem. C* **2019,** *123* (30), 18467-18474.
24. Wang, X. L.; Dong, L.-Z.; Qiao, M.; Tang, Y.-J.; Liu, J.; Li, Y.; Li, S. L.; Su, J. X.; Lan, Y. Q., Exploring the Performance Improvement of the Oxygen Evolution Reaction in a Stable Bimetal–Organic Framework System. *Angew. Chem. Int. Ed.* **2018,** *57* (31), 9660-9664.
25. Zhao, J.; Chen, Z., Single Mo Atom Supported on Defective Boron Nitride Monolayer as an Efficient Electrocatalyst for Nitrogen Fixation: A Computational Study. *J. Am. Chem. Soc.* **2017,** *139* (36), 12480-12487.
26. Peterson, A. A.; Abild-Pedersen, F.; Studt, F.; Rossmeisl, J.; Nørskov, J. K., How copper catalyzes the electroreduction of carbon dioxide into hydrocarbon fuels. *Energy Environ. Sci.* **2010,** *3* (9), 1311-1315.
27. Chen, L. D.; Urushihara, M.; Chan, K.; Nørskov, J. K., Electric Field Effects in Electrochemical CO_2 Reduction. *ACS Catal.* **2016,** *6* (10), 7133-7139.
28. Shi, C.; Hansen, H. A.; Lausche, A. C.; Nørskov, J. K., Trends in electrochemical CO_2 reduction activity for open and close-packed metal surfaces. *Phys. Chem. Chem. Phys.* **2014,** *16* (10), 4720-4727.
29. Jovanov, Z. P.; Hansen, H. A.; Varela, A. S.; Malacrida, P.; Peterson, A. A.; Nørskov, J. K.; Stephens, I. E. L.; Chorkendorff, I., Opportunities and challenges in the electrocatalysis of CO_2 and CO reduction using bifunctional surfaces: A theoretical and experimental study of Au–Cd alloys. *J. Catal.* **2016,** *343*, 215-231.

30. Peterson, A. A.; Nørskov, J. K., Activity Descriptors for CO_2 Electroreduction to Methane on Transition-Metal Catalysts. *J. Phys. Chem. Lett.* **2012,** *3* (2), 251-258.
31. Zhang, W.; Hu, Y.; Ma, L.; Zhu, G.; Wang, Y.; Xue, X.; Chen, R.; Yang, S.; Jin, Z., Progress and Perspective of Electrocatalytic CO_2 Reduction for Renewable Carbonaceous Fuels and Chemicals. *Adv. Sci.* **2018,** *5* (1), 1700275.
32. Jones, J.-P.; Prakash, G. K. S.; Olah, G. A., Electrochemical CO_2 Reduction: Recent Advances and Current Trends. *Isr. J. Chem.* **2014,** *54* (10), 1451-1466.
33. Bagger, A.; Ju, W.; Varela, A. S.; Strasser, P.; Rossmeisl, J., Electrochemical CO_2 Reduction: A Classification Problem. *ChemPhysChem* **2017,** *18* (22), 3266-3273.
34. Hori, Y.; Murata, A.; Takahashi, R., Formation of hydrocarbons in the electrochemical reduction of carbon dioxide at a copper electrode in aqueous solution. *J. Chem. Soc., Faraday Trans. 1* **1989,** *85* (8), 2309-2326.
35. Raciti, D.; Wang, C., Recent Advances in CO_2 Reduction Electrocatalysis on Copper. *ACS Energy Lett.* **2018,** *3* (7), 1545-1556.
36. Kuhl, K. P.; Cave, E. R.; Abram, D. N.; Jaramillo, T. F., New insights into the electrochemical reduction of carbon dioxide on metallic copper surfaces. *Energy Environ. Sci.* **2012,** *5* (5), 7050-7059.
37. Nie, X.; Esopi, M. R.; Janik, M. J.; Asthagiri, A., Selectivity of CO_2 Reduction on Copper Electrodes: The Role of the Kinetics of Elementary Steps. *Angew. Chem. Int. Ed.* **2013,** *52* (9), 2459-2462.
38. Montoya, J. H.; Peterson, A. A.; Nørskov, J. K., Insights into C-C Coupling in CO_2 Electroreduction on Copper Electrodes. *ChemCatChem* **2013,** *5* (3), 737-742.
39. Hori, Y.; Wakebe, H.; Tsukamoto, T.; Koga, O., Electrocatalytic process of CO selectivity in electrochemical reduction of CO_2 at metal electrodes in aqueous media. *Electrochim. Acta* **1994,** *39* (11), 1833-1839.
40. Zhao, S.; Li, S.; Guo, T.; Zhang, S.; Wang, J.; Wu, Y.; Chen, Y., Advances in Sn-Based Catalysts for Electrochemical CO_2 Reduction. *Nano-Micro Lett.* **2019,** *11* (1), 62.
41. Bumroongsakulsawat, P.; Kelsall, G. H., Effect of solution pH on CO: formate formation rates during electrochemical reduction of aqueous CO_2 at Sn cathodes. *Electrochim. Acta* **2014,** *141*, 216-225.
42. Yadav, V. S. K.; Purkait, M. K., Synthesis of Pb_2O electrocatalyst and its application in the electrochemical reduction of CO_2 to HCOOH in various electrolytes. *RSC Adv.* **2015,** *5* (50), 40414-40421.
43. Zhao, C.; Wang, J.; Goodenough, J. B., Comparison of electrocatalytic reduction of CO_2 to HCOOH with different tin oxides on carbon nanotubes. *Electrochem. Commun.* **2016,** *65*, 9-13.
44. Bashir, S. M.; Hossain, S. S.; ur Rahman, S.; Ahmed, S.; Hossain, M. M., NiO/MWCNT Catalysts for Electrochemical Reduction of CO_2. *Electrocatalysis* **2015,** *6* (6), 544-553.
45. Ramesha, G. K.; Brennecke, J. F.; Kamat, P. V., Origin of Catalytic Effect in the Reduction of CO_2 at Nanostructured TiO_2 Films. *ACS Catal.* **2014,** *4* (9), 3249-3254.

46. Chan, K.; Tsai, C.; Hansen, H. A.; Nørskov, J. K., Molybdenum Sulfides and Selenides as Possible Electrocatalysts for CO_2 Reduction. *ChemCatChem* **2014,** *6* (7), 1899-1905.
47. Asadi, M.; Kumar, B.; Behranginia, A.; Rosen, B. A.; Baskin, A.; Repnin, N.; Pisasale, D.; Phillips, P.; Zhu, W.; Haasch, R.; Klie, R. F.; Král, P.; Abiade, J.; Salehi-Khojin, A., Robust carbon dioxide reduction on molybdenum disulphide edges. *Nat. Commun.* **2014,** *5* (1), 4470.
48. Kim, S. K.; Zhang, Y.-J.; Bergstrom, H.; Michalsky, R.; Peterson, A., Understanding the Low-Overpotential Production of CH_4 from CO_2 on Mo_2C Catalysts. *ACS Catal.* **2016,** *6* (3), 2003-2013.
49. Wu, J.; Yadav, R. M.; Liu, M.; Sharma, P. P.; Tiwary, C. S.; Ma, L.; Zou, X.; Zhou, X. D.; Yakobson, B. I.; Lou, J.; Ajayan, P. M., Achieving Highly Efficient, Selective, and Stable CO_2 Reduction on Nitrogen-Doped Carbon Nanotubes. *ACS Nano* **2015,** *9* (5), 5364-5371.
50. Wang, H.; Chen, Y.; Hou, X.; Ma, C.; Tan, T., Nitrogen-doped graphenes as efficient electrocatalysts for the selective reduction of carbon dioxide to formate in aqueous solution. *Green Chem.* **2016,** *18* (11), 3250-3256.
51. Xu, J.; Kan, Y.; Huang, R.; Zhang, B.; Wang, B.; Wu, K.-H.; Lin, Y.; Sun, X.; Li, Q.; Centi, G.; Su, D., Revealing the Origin of Activity in Nitrogen-Doped Nanocarbons towards Electrocatalytic Reduction of Carbon Dioxide. *ChemSusChem* **2016,** *9* (10), 1085-1089.
52. Wu, J.; Ma, S.; Sun, J.; Gold, J. I.; Tiwary, C.; Kim, B.; Zhu, L.; Chopra, N.; Odeh, I. N.; Vajtai, R.; Yu, A. Z.; Luo, R.; Lou, J.; Ding, G.; Kenis, P. J. A.; Ajayan, P. M., A metal-free electrocatalyst for carbon dioxide reduction to multi-carbon hydrocarbons and oxygenates. *Nat. Commun.* **2016,** *7* (1), 13869.
53. Jiwanti, P. K.; Natsui, K.; Einaga, Y., The Utilization of Boron-doped Diamond Electrodes for the Electrochemical Reduction of CO_2: Toward the Production Compounds with a High Number of Carbon Atoms. *Electrochemistry* **2019,** *87* (2), 109-113.
54. Natsui, K.; Iwakawa, H.; Ikemiya, N.; Nakata, K.; Einaga, Y., Stable and Highly Efficient Electrochemical Production of Formic Acid from Carbon Dioxide Using Diamond Electrodes. *Angew. Chem. Int. Ed.* **2018,** *57* (10), 2639-2643.
55. Nakata, K.; Ozaki, T.; Terashima, C.; Fujishima, A.; Einaga, Y., High-Yield Electrochemical Production of Formaldehyde from CO_2 and Seawater. *Angew. Chem. Int. Ed.* **2014,** *53* (3), 871-874.
56. Rakowski Dubois, M.; Dubois, D. L., Development of Molecular Electrocatalysts for CO_2 Reduction and H_2 Production/Oxidation. *Acc. Chem. Res.* **2009,** *42* (12), 1974-1982.
57. Zhang, S.; Fan, Q.; Xia, R.; Meyer, T. J., CO_2 Reduction: From Homogeneous to Heterogeneous Electrocatalysis. *Acc. Chem. Res.* **2020,** *53* (1), 255-264.
58. Ren, S.; Joulié, D.; Salvatore, D.; Torbensen, K.; Wang, M.; Robert, M.; Berlinguette, C. P., Molecular electrocatalysts can mediate fast, selective CO_2 reduction in a flow cell. *Science* **2019,** *365* (6451), 367.
59. Benson, E. E.; Kubiak, C. P.; Sathrum, A. J.; Smieja, J. M., Electrocatalytic and homogeneous approaches to conversion of CO_2 to liquid fuels. *Chem. Soc. Rev.* **2009,** *38* (1), 89-99.

60. Weng, Z.; Jiang, J.; Wu, Y.; Wu, Z.; Guo, X.; Materna, K. L.; Liu, W.; Batista, V. S.; Brudvig, G. W.; Wang, H., Electrochemical CO_2 Reduction to Hydrocarbons on a Heterogeneous Molecular Cu Catalyst in Aqueous Solution. *J. Am. Chem. Soc.* **2016,** *138* (26), 8076-8079.
61. Elgrishi, N.; Chambers, M. B.; Wang, X.; Fontecave, M., Molecular polypyridine-based metal complexes as catalysts for the reduction of CO_2. *Chem. Soc. Rev.* **2017,** *46* (3), 761-796.
62. Meshitsuka, S.; Ichikawa, M.; Tamaru, K., Electrocatalysis by metal phthalocyanines in the reduction of carbon dioxide. *J. Chem. Soc., Chem. Commun.* **1974,** (5), 158-159.
63. Fisher, B. J.; Eisenberg, R., Electrocatalytic reduction of carbon dioxide by using macrocycles of nickel and cobalt. *J. Am. Chem. Soc.* **1980,** *102* (24), 7361-7363.
64. Smieja, J. M.; Kubiak, C. P., Re (bipy-tBu)$(CO)_3Cl^-$ improved catalytic activity for reduction of carbon dioxide: IR-spectroelectrochemical and mechanistic studies. *Inorg. Chem.* **2010,** *49* (20), 9283-9289.
65. Machan, C. W.; Sampson, M. D.; Kubiak, C. P., A Molecular Ruthenium Electrocatalyst for the Reduction of Carbon Dioxide to CO and Formate. *J. Am. Chem. Soc.* **2015,** *137* (26), 8564-8571.
66. Chen, W.; Fan, Z.; Lai, Z., Synthesis of core–shell heterostructured Cu/Cu_2O nanowires monitored by in situ XRD as efficient visible-light photocatalysts. *J. Mater. Chem. A* **2013,** *1* (44), 13862-13868.
67. Larrazábal, G. O.; Martín, A. J.; Pérez-Ramírez, J., Building Blocks for High Performance in Electrocatalytic CO_2 Reduction: Materials, Optimization Strategies, and Device Engineering. *J. Phys. Chem. Lett.* **2017,** *8* (16), 3933-3944.
68. Wang, Y.; Han, P.; Lv, X.; Zhang, L.; Zheng, G., Defect and Interface Engineering for Aqueous Electrocatalytic CO_2 Reduction. *Joule* **2018,** *2* (12), 2551-2582.
69. Pander III, J. E.; Ren, D.; Huang, Y.; Loo, N. W. X.; Hong, S. H. L.; Yeo, B. S., Understanding the Heterogeneous Electrocatalytic Reduction of Carbon Dioxide on Oxide-Derived Catalysts. *ChemElectroChem* **2018,** *5* (2), 219-237.
70. Li, C. W.; Kanan, M. W., CO_2 Reduction at Low Overpotential on Cu Electrodes Resulting from the Reduction of Thick Cu_2O Films. *J. Am. Chem. Soc.* **2012,** *134* (17), 7231-7234.
71. Feng, X.; Jiang, K.; Fan, S.; Kanan, M. W., A Direct Grain-Boundary-Activity Correlation for CO Electroreduction on Cu Nanoparticles. *ACS Cent. Sci.* **2016,** *2* (3), 169-174.
72. Lee, C. H.; Kanan, M. W., Controlling H^+ vs CO_2 Reduction Selectivity on Pb Electrodes. *ACS Catal.* **2015,** *5* (1), 465-469.
73. Chen, Y.; Kanan, M. W., Tin Oxide Dependence of the CO_2 Reduction Efficiency on Tin Electrodes and Enhanced Activity for Tin/Tin Oxide Thin-Film Catalysts. *J. Am. Chem. Soc.* **2012,** *134* (4), 1986-1989.
74. Kim, D.; Resasco, J.; Yu, Y.; Asiri, A. M.; Yang, P., Synergistic geometric and electronic effects for electrochemical reduction of carbon dioxide using gold–copper bimetallic nanoparticles. *Nat. Commun.* **2014,** *5* (1), 4948.
75. Ma, S.; Sadakiyo, M.; Heima, M.; Luo, R.; Haasch, R. T.; Gold, J. I.; Yamauchi, M.; Kenis, P. J. A., Electroreduction of Carbon Dioxide to Hydrocarbons Using

Bimetallic Cu–Pd Catalysts with Different Mixing Patterns. *J. Am. Chem. Soc.* **2017,** *139* (1), 47-50.
76. Ren, D.; Ang, B. S.-H.; Yeo, B. S., Tuning the Selectivity of Carbon Dioxide Electroreduction toward Ethanol on Oxide-Derived Cu_xZn Catalysts. *ACS Catal.* **2016,** *6* (12), 8239-8247.
77. Chen, Y.; Ji, S.; Chen, C.; Peng, Q.; Wang, D.; Li, Y., Single-Atom Catalysts: Synthetic Strategies and Electrochemical Applications. *Joule* **2018,** *2* (7), 1242-1264.
78. Lü, F.; Bao, H.; Mi, Y.; Liu, Y.; Sun, J.; Peng, X.; Qiu, Y.; Zhuo, L.; Liu, X.; Luo, J., Electrochemical CO_2 reduction: from nanoclusters to single atom catalysts. *Sustainable Energy Fuels* **2020,** *4* (3), 1012-1028.
79. Back, S.; Lim, J.; Kim, N.-Y.; Kim, Y.-H.; Jung, Y., Single-atom catalysts for CO_2 electroreduction with significant activity and selectivity improvements. *Chem. Sci.* **2017,** *8* (2), 1090-1096.
80. Jiang, K.; Siahrostami, S.; Zheng, T.; Hu, Y.; Hwang, S.; Stavitski, E.; Peng, Y.; Dynes, J.; Gangisetty, M.; Su, D.; Attenkofer, K.; Wang, H., Isolated Ni single atoms in graphene nanosheets for high-performance CO_2 reduction. *Energy Environ. Sci.* **2018,** *11* (4), 893-903.
81. Zheng, T.; Jiang, K.; Ta, N.; Hu, Y.; Zeng, J.; Liu, J.; Wang, H., Large-Scale and Highly Selective CO_2 Electrocatalytic Reduction on Nickel Single-Atom Catalyst. *Joule* **2019,** *3* (1), 265-278.
82. Reske, R.; Mistry, H.; Behafarid, F.; Roldan Cuenya, B.; Strasser, P., Particle Size Effects in the Catalytic Electroreduction of CO_2 on Cu Nanoparticles. *J. Am. Chem. Soc.* **2014,** *136* (19), 6978-6986.
83. Wang, Z.; Yang, G.; Zhang, Z.; Jin, M.; Yin, Y., Selectivity on Etching: Creation of High-Energy Facets on Copper Nanocrystals for CO_2 Electrochemical Reduction. *ACS Nano* **2016,** *10* (4), 4559-4564.
84. Tang, W.; Peterson, A. A.; Varela, A. S.; Jovanov, Z. P.; Bech, L.; Durand, W. J.; Dahl, S.; Nørskov, J. K.; Chorkendorff, I., The importance of surface morphology in controlling the selectivity of polycrystalline copper for CO_2 electroreduction. *Phys. Chem. Chem. Phys.* **2012,** *14* (1), 76-81.
85. Raciti, D.; Livi, K. J.; Wang, C., Highly Dense Cu Nanowires for Low-Overpotential CO_2 Reduction. *Nano Lett.* **2015,** *15* (10), 6829-6835.
86. Ma, M.; Djanashvili, K.; Smith, W. A., Selective electrochemical reduction of CO_2 to CO on CuO-derived Cu nanowires. *Phys. Chem. Chem. Phys.* **2015,** *17* (32), 20861-20867.
87. Yang, K. D.; Ko, W. R.; Lee, J. H.; Kim, S. J.; Lee, H.; Lee, M. H.; Nam, K. T., Morphology-Directed Selective Production of Ethylene or Ethane from CO_2 on a Cu Mesopore Electrode. *Angew. Chem. Int. Ed.* **2017,** *56* (3), 796-800.
88. Reller, C.; Krause, R.; Volkova, E.; Schmid, B.; Neubauer, S.; Rucki, A.; Schuster, M.; Schmid, G., Selective Electroreduction of CO_2 toward Ethylene on Nano Dendritic Copper Catalysts at High Current Density. *Adv. Energy Mater.* **2017,** *7* (12), 1602114.
89. Hoang, T. T. H.; Ma, S.; Gold, J. I.; Kenis, P. J. A.; Gewirth, A. A., Nanoporous Copper Films by Additive-Controlled Electrodeposition: CO_2 Reduction Catalysis. *ACS Catal.* **2017,** *7* (5), 3313-3321.

90. Wang, Y.; Liu, J.; Wang, Y.; Al-Enizi, A. M.; Zheng, G., Tuning of CO_2 Reduction Selectivity on Metal Electrocatalysts. *Small* **2017,** *13* (43), 1701809.
91. Hori, Y.; Takahashi, I.; Koga, O.; Hoshi, N., Selective Formation of C2 Compounds from Electrochemical Reduction of CO_2 at a Series of Copper Single Crystal Electrodes. *J. Phys. Chem. B* **2002,** *106* (1), 15-17.
92. Huang, Y.; Handoko, A. D.; Hirunsit, P.; Yeo, B. S., Electrochemical reduction of CO_2 using copper single-crystal surfaces: effects of CO* coverage on the selective formation of ethylene. *ACS Catal.* **2017,** *7* (3), 1749-1756.
93. Liu, M.; Pang, Y.; Zhang, B.; De Luna, P.; Voznyy, O. Xu, J.; Zheng, X.; Dinh, C. T.; Fan, F.; Cao, C.; de Arquer, F. P. G.; Safaei, T. S.; Mepham, A.; Klinkova, A.; Kumacheva, E.; Filleter, T.; Sinton, D.; Kelley, S. O.; Sargent, E. H., Enhanced electrocatalytic CO_2 reduction via field-induced reagent concentration. *Nature* **2016,** *537* (7620), 382-386.
94. Saberi Safaei, T.; Mepham, A.; Zheng, X.; Pang, Y.; Dinh, C.-T.; Liu, M.; Sinton, D.; Kelley, S. O.; Sargent, E. H., High-Density Nanosharp Microstructures Enable Efficient CO_2 Electroreduction. *Nano Lett.* **2016,** *16* (11), 7224-7228.
95. Lin, R.; Guo, J.; Li, X.; Patel, P.; Seifitokaldani, A., Electrochemical Reactors for CO_2 Conversion. *Catalysts* **2020,** *10* (5), 473.
96. Nguyen, T. N.; Dinh, C.-T., Gas diffusion electrode design for electrochemical carbon dioxide reduction. *Chem. Soc. Rev.* **2020,** *49* (21), 7488-7504.
97. Kaneco, S.; Iiba, K.; Katsumata, H.; Suzuki, T.; Ohta, K., Electrochemical reduction of high pressure CO_2 at a Cu electrode in cold methanol. *Electrochim. Acta* **2006,** *51* (23), 4880-4885.
98. Yang, H.; Lin, Q.; Zhang, C.; Yu, X.; Cheng, Z.; Li, G.; Hu, Q.; Ren, X.; Zhang, Q.; Liu, J.; He, C., Carbon dioxide electroreduction on single-atom nickel decorated carbon membranes with industry compatible current densities. *Nat. Commun.* **2020,** *11* (1), 593.
99. Song, J. T.; Song, H.; Kim, B.; Oh, J., Towards Higher Rate Electrochemical CO_2 Conversion: From Liquid-Phase to Gas-Phase Systems. *Catalysts* **2019,** *9* (3), 224.
100. Cook, R. L.; MacDuff, R. C.; Sammells, A. F., Ambient Temperature Gas Phase CO_2 Reduction to Hydrocarbons at Solid Polymer Electrolyte Cells. *J. Electrochem. Soc.* **1988,** *135* (6), 1470-1471.
101. Liu, K.; Smith, W. A.; Burdyny, T., Introductory Guide to Assembling and Operating Gas Diffusion Electrodes for Electrochemical CO_2 Reduction. *ACS Energy Lett.* **2019,** *4* (3), 639-643.
102. Hori, Y.; Ito, H.; Okano, K.; Nagasu, K.; Sato, S., Silver-coated ion exchange membrane electrode applied to electrochemical reduction of carbon dioxide. *Electrochim. Acta* **2003,** *48* (18), 2651-2657.
103. Weng, L. C.; Bell, A. T.; Weber, A. Z., Towards membrane-electrode assembly systems for CO_2 reduction: a modeling study. *Energy Environ. Sci.* **2019,** *12* (6), 1950-1968.
104. Whipple, D. T.; Finke, E. C.; Kenis, P. J. A., Microfluidic Reactor for the Electrochemical Reduction of Carbon Dioxide: The Effect of pH. *Electrochem. Solid-State Lett.* **2010,** *13* (9), B109.

105. Burdyny, T.; Smith, W. A., CO_2 reduction on gas-diffusion electrodes and why catalytic performance must be assessed at commercially-relevant conditions. *Energy Environ. Sci.* **2019,** *12* (5), 1442-1453.
106. Kim, B.; Hillman, F.; Ariyoshi, M.; Fujikawa, S.; Kenis, P. J. A., Effects of composition of the micro porous layer and the substrate on performance in the electrochemical reduction of CO_2 to CO. *J. Power Sources* **2016,** *312*, 192-198.
107. Dinh, C. T.; Burdyny, T.;Kibria, M. G.; Seifitokaldani, A.; Gabardo, C. M.; García de Arquer, F. P.; Kiani, A.; Edwards, J. P.; De Luna, P.; Bushuyev, O. S.; Zou, C.; Quintero-Bermudez, R.; Pang, Y.; Sinton, D.; Sargent, E. H., CO_2 electroreduction to ethylene via hydroxide-mediated copper catalysis at an abrupt interface. *Science* **2018,** *360* (6390), 783.
108. Jhong, H. R. M.; Brushett, F. R.; Kenis, P. J. A., The Effects of Catalyst Layer Deposition Methodology on Electrode Performance. *Adv. Energy Mater.* **2013,** *3* (5), 589-599.
109. Junge Puring, K.; Siegmund, D.; Timm, J.; Möllenbruck, F.; Schemme, S.; Marschall, R.; Apfel, U.-P., Electrochemical CO_2 Reduction: Tailoring Catalyst Layers in Gas Diffusion Electrodes. *Adv. Sustainable Syst.* **2021,** *5* (1), 2000088.
110. Hui, S.; Shaigan, N.; Neburchilov, V.; Zhang, L.; Malek, K.; Eikerling, M.; Luna, P. D., Three-Dimensional Cathodes for Electrochemical Reduction of CO_2: From Macro- to Nano-Engineering. *Nanomaterials* **2020,** *10* (9), 1884.
111. Ham, Y. S.; Choe, S.; Kim, M. J.; Lim, T.; Kim, S.-K.; Kim, J. J., Electrodeposited Ag catalysts for the electrochemical reduction of CO_2 to CO. *Appl. Catal., B* **2017,** *208*, 35-43.
112. Rosen, J.; Hutchings, G. S.; Lu, Q.; Forest, R. V.; Moore, A.; Jiao, F., Electrodeposited Zn Dendrites with Enhanced CO Selectivity for Electrocatalytic CO_2 Reduction. *ACS Catal.* **2015,** *5* (8), 4586-4591.
113. Dutta, A.; Morstein, C. E.; Rahaman, M.; Cedeño López, A.; Broekmann, P., Beyond Copper in CO_2 Electrolysis: Effective Hydrocarbon Production on Silver-Nanofoam Catalysts. *ACS Catal.* **2018,** *8* (9), 8357-8368.
114. Lai, Q.; Yang, N.; Yuan, G., Highly efficient In–Sn alloy catalysts for electrochemical reduction of CO_2 to formate. *Electrochem. Commun.* **2017,** *83*, 24-27.
115. Kuhn, P.; Antonietti, M.; Thomas, A., Porous, Covalent Triazine-Based Frameworks Prepared by Ionothermal Synthesis. *Angew. Chem. Int. Ed.* **2008,** *47* (18), 3450-3453.
116. Ren, S.; Bojdys, M. J.; Dawson, R.; Laybourn, A.; Khimyak, Y. Z.; Adams, D. J.; Cooper, A. I., Porous, Fluorescent, Covalent Triazine-Based Frameworks Via Room-Temperature and Microwave-Assisted Synthesis. *Adv. Mater.* **2012,** *24* (17), 2357-2361.
117. Guo, J.; Xu, Y.; Jin, S.; Chen, L.; Kaji, T.; Honsho, Y.; Addicoat, M. A.; Kim, J.; Saeki, A.; Ihee, H.; Seki, S.; Irle, S.; Hiramoto, M.; Gao, J.; Jiang, D., Conjugated organic framework with three-dimensionally ordered stable structure and delocalized π clouds. *Nat. Commun.* **2013,** *4* (1), 2736.
118. Puthiaraj, P.; Lee, Y.-R.; Zhang, S.; Ahn, W.-S., Triazine-based covalent organic polymers: design, synthesis and applications in heterogeneous catalysis. *J. Mater. Chem. A* **2016,** *4* (42), 16288-16311.

119. Lin, S.; Diercks, C. S.; Zhang, Y.-B.; Kornienko, N.; Nichols, E. M.; Zhao, Y.; Paris, A. R.; Kim, D.; Yang, P.; Yaghi, O. M.; Chang, C. J., Covalent organic frameworks comprising cobalt porphyrins for catalytic CO_2 reduction in water. *Science* **2015,** *349* (6253), 1208.
120. Banerjee, T.; Haase, F.; Savasci, G.; Gottschling, K.; Ochsenfeld, C.; Lotsch, B. V., Single-Site Photocatalytic H_2 Evolution from Covalent Organic Frameworks with Molecular Cobaloxime Co-Catalysts. *J. Am. Chem. Soc.* **2017,** *139* (45), 16228-16234.
121. Yamaguchi, S.; Kamiya, K.; Hashimoto, K.; Nakanishi, S., Ru atom-modified covalent triazine framework as a robust electrocatalyst for selective alcohol oxidation in aqueous electrolytes. *Chem. Commun.* **2017,** *53* (75), 10437-10440.
122. Yoshioka, T.; Iwase, K.; Nakanishi, S.; Hashimoto, K.; Kamiya, K., Electrocatalytic Reduction of Nitrate to Nitrous Oxide by a Copper-Modified Covalent Triazine Framework. *J. Phys. Chem. C* **2016,** *120* (29), 15729-15734.
123. Kamiya, K.; Kamai, R.; Hashimoto, K.; Nakanishi, S., Platinum-modified covalent triazine frameworks hybridized with carbon nanoparticles as methanol-tolerant oxygen reduction electrocatalysts. *Nat. Commun.* **2014,** *5* (1), 5040.
124. Iwase, K.; Yoshioka, T.; Nakanishi, S.; Hashimoto, K.; Kamiya, K., Copper-Modified Covalent Triazine Frameworks as Non-Noble-Metal Electrocatalysts for Oxygen Reduction. *Angew. Chem. Int. Ed.* **2015,** *54* (38), 11068-11072.
125. Kamiya, K.; Tatebe, T.; Yamamura, S.; Iwase, K.; Harada, T.; Nakanishi, S., Selective Reduction of Nitrate by a Local Cell Catalyst Composed of Metal-Doped Covalent Triazine Frameworks. *ACS Catal.* **2018,** *8* (4), 2693-2698.
126. Su, P.; Iwase, K.; Harada, T.; Kamiya, K.; Nakanishi, S., Covalent triazine framework modified with coordinatively-unsaturated Co or Ni atoms for CO_2 electrochemical reduction. *Chem. Sci.* **2018,** *9* (16), 3941-3947.
127. Mikkelsen, M.; Jørgensen, M.; Krebs, F. C., The teraton challenge. A review of fixation and transformation of carbon dioxide. *Energy Environ. Sci.* **2010,** *3* (1), 43-81.
128. Del Castillo, A.; Alvarez-Guerra, M.; Solla-Gullón, J.; Sáez, A.; Montiel, V.; Irabien, A., Sn nanoparticles on gas diffusion electrodes: Synthesis, characterization and use for continuous CO_2 electroreduction to formate. *J. CO_2 Util.* **2017,** *18*, 222-228.
129. Ma, S.; Sadakiyo, M.; Luo, R.; Heima, M.; Yamauchi, M.; Kenis, P. J. A., One-step electrosynthesis of ethylene and ethanol from CO_2 in an alkaline electrolyzer. *J. Power Sources* **2016,** *301*, 219-228.
130. Endrődi, B.; Bencsik, G.; Darvas, F. Jones, R.; Rajeshwar, K.; Janáky, C., Continuous-flow electroreduction of carbon dioxide. *Prog. Energy Combust. Sci.* **2017,** *62*, 133-154.
131. Higgins, D.; Hahn, C.; Xiang, C.; Jaramillo, T. F.; Weber, A. Z., Gas-Diffusion Electrodes for Carbon Dioxide Reduction: A New Paradigm. *ACS Energy Lett.* **2019,** *4* (1), 317-324.
132. Kopljar, D.; Inan, A.; Vindayer, P.; Wagner, N.; Klemm, E., Electrochemical reduction of CO_2 to formate at high current density using gas diffusion electrodes. *J. Appl. Electrochem.* **2014,** *44* (10), 1107-1116.

133. Kim, B.; Ma, S.; Molly Jhong, H. R.; Kenis, P. J. A., Influence of dilute feed and pH on electrochemical reduction of CO_2 to CO on Ag in a continuous flow electrolyzer. *Electrochim. Acta* **2015,** *166*, 271-276.
134. Lv, J. J.; Jouny, M.; Luc, W.; Zhu, W.; Zhu, J.-J.; Jiao, F., A Highly Porous Copper Electrocatalyst for Carbon Dioxide Reduction. *Adv. Mater.* **2018,** *30* (49), 1803111.
135. Ooka, H.; Figueiredo, M. C.; Koper, M. T. M., Competition between Hydrogen Evolution and Carbon Dioxide Reduction on Copper Electrodes in Mildly Acidic Media. *Langmuir* **2017,** *33* (37), 9307-9313.
136. Singh, M. R.; Clark, E. L.; Bell, A. T., Effects of electrolyte, catalyst, and membrane composition and operating conditions on the performance of solar-driven electrochemical reduction of carbon dioxide. *Phys. Chem. Chem. Phys.* **2015,** *17* (29), 18924-18936.
137. Singh, M. R.; Goodpaster, J. D.; Weber, A. Z.; Head-Gordon, M.; Bell, A. T., Mechanistic insights into electrochemical reduction of CO_2 over Ag using density functional theory and transport models. *Proc. Natl. Acad. Sci. U. S. A.* **2017,** *114* (42), E8812.
138. Hall, A. S.; Yoon, Y.; Wuttig, A.; Surendranath, Y., Mesostructure-Induced Selectivity in CO_2 Reduction Catalysis. *J. Am. Chem. Soc.* **2015,** *137* (47), 14834-14837.
139. Yoon, Y.; Hall, A. S.; Surendranath, Y., Tuning of Silver Catalyst Mesostructure Promotes Selective Carbon Dioxide Conversion into Fuels. *Angew. Chem. Int. Ed.* **2016,** *55* (49), 15282-15286.
140. Sen, S.; Liu, D.; Palmore, G. T. R., Electrochemical Reduction of CO_2 at Copper Nanofoams. *ACS Catal.* **2014,** *4* (9), 3091-3095.
141. Ma, M.; Trześniewski, B. J.; Xie, J.; Smith, W. A., Selective and Efficient Reduction of Carbon Dioxide to Carbon Monoxide on Oxide-Derived Nanostructured Silver Electrocatalysts. *Angew. Chem. Int. Ed.* **2016,** *55* (33), 9748-9752.
142. Shinagawa, T.; Murase, K.; Otomo, S.; Katayama, J.-i.; Izaki, M., Effects of Counteranions and Dissolved Oxygen on Chemical ZnO Deposition from Aqueous Solutions. *J. Electrochem. Soc.* **2009,** *156* (5), H320.
143. Peulon, S.; Lincot, D., Cathodic electrodeposition from aqueous solution of dense or open-structured zinc oxide films. *Adv. Mater.* **1996,** *8* (2), 166-170.
144. Khor, A.; Leung, P.; Mohamed, M. R.; Flox, C.; Xu, Q.; An, L.; Wills, R. G. A.; Morante, J. R.; Shah, A. A., Review of zinc-based hybrid flow batteries: From fundamentals to applications. *Mater. Today Energy* **2018,** *8*, 80-108.
145. Krężel, A.; Maret, W., The biological inorganic chemistry of zinc ions. *Arch. Biochem. Biophys.* **2016,** *611*, 3-19.
146. Han, Y. X.; Ding, Y. Z.; Yin, W. Z.; Ma, Z. X., Preparation of homogeneous ZnO nanoparticles via precipitation-pyrolysis with $Zn_5(CO_3)_2(OH)_6$ as precursor. *Trans. Nonferrous Met. Soc. China* **2006,** *16* (5), 1205-1212.
147. Han, W.; Yang, K.; Li, D.; Zhang, Z.; Ma, J.; Ni, S.; Yang, X., The fabrication and characterization of $Zn_5(CO_3)_2(OH)_6$ as a new anode material for lithium ion batteries. *Mater. Lett.* **2016,** *164*, 148-151.

148. Cheng, J.; Poduska, K. M., A Strategy for Hydroxide Exclusion in Nanocrystalline Solid-State Metathesis Products. *Nanomaterials* **2013,** *3* (3), 317-324.
149. Cook, R. L.; MacDuff, R. C.; Sammells, A. F., High Rate Gas Phase CO_2 Reduction to Ethylene and Methane Using Gas Diffusion Electrodes. *J. Electrochem. Soc.* **1990,** *137* (2), 607-608.
150. Loiudice, A.; Lobaccaro, P.; Kamali, E. A.; Thao, T.;Huang, B. H.; Ager, J. W.; Buonsanti, R., Tailoring Copper Nanocrystals towards C2 Products in Electrochemical CO_2 Reduction. *Angew. Chem. Int. Ed.* **2016,** *55* (19), 5789-5792.
151. Kas, R.; Kortlever, R.; Milbrat, A.; Koper, M. T. M.; Mul, G.; Baltrusaitis, J., Electrochemical CO_2 reduction on Cu_2O-derived copper nanoparticles: controlling the catalytic selectivity of hydrocarbons. *Phys. Chem. Chem. Phys.* **2014,** *16* (24), 12194-12201.
152. De Gregorio, G. L.; Burdyny, T.; Loiudice, A.; Iyengar, P.; Smith, W. A.; Buonsanti, R., Facet-Dependent Selectivity of Cu Catalysts in Electrochemical CO_2 Reduction at Commercially Viable Current Densities. *ACS Catal.* **2020,** *10* (9), 4854-4862.
153. De Luna, P.; Quintero-Bermudez, R.; Dinh, C. T.; Ross, M. B.; Bushuyev, O. S.; Todorović, P.; Regier, T.; Kelley, S. O.; Yang, P.; Sargent, E. H., Catalyst electro-redeposition controls morphology and oxidation state for selective carbon dioxide reduction. *Nat. Catal.* **2018,** *1* (2), 103-110.
154. Karapinar, D.; Huan, N. T.; Ranjbar Sahraie, N.; Li, J.; Wakerley, D.; Touati, N.; Zanna, S.; Taverna, D.; Galvão Tizei, L. H.; Zitolo, A.; Jaouen, F.; Mougel, V.; Fontecave, M., Electroreduction of CO_2 on Single-Site Copper-Nitrogen-Doped Carbon Material: Selective Formation of Ethanol and Reversible Restructuration of the Metal Sites. *Angew. Chem. Int. Ed.* **2019,** *58* (42), 15098-15103.
155. Wang, J.; Gan, L.; Zhang, Q.; Reddu, V.; Peng, Y.; Liu, Z.; Xia, X.; Wang, C.; Wang, X., A Water-Soluble Cu Complex as Molecular Catalyst for Electrocatalytic CO_2 Reduction on Graphene-Based Electrodes. *Adv. Energy Mater.* **2019,** *9* (3), 1803151.
156. Karapinar, D.; Zitolo, A.; Huan, T. N.; Zanna, S.; Taverna, D.; Galvão Tizei, L. H.; Giaume, D.; Marcus, P.; Mougel, V.; Fontecave, M., Carbon-Nanotube-Supported Copper Polyphthalocyanine for Efficient and Selective Electrocatalytic CO_2 Reduction to CO. *ChemSusChem* **2020,** *13* (1), 173-179.
157. Zhang, S.; Kang, P.; Meyer, T. J., Nanostructured Tin Catalysts for Selective Electrochemical Reduction of Carbon Dioxide to Formate. *J. Am. Chem. Soc.* **2014,** *136* (5), 1734-1737.
158. Du, D.; Lan, R.; Humphreys, J.; Sengodan, S.; Xie, K.; Wang, H.; Tao , S., Achieving Both High Selectivity and Current Density for CO_2 Reduction to Formate on Nanoporous Tin Foam Electrocatalysts. *ChemistrySelect* **2016,** *1* (8), 1711-1715.
159. Lv, W.; Zhang, R.; Gao, P.; Lei, L., Studies on the faradaic efficiency for electrochemical reduction of carbon dioxide to formate on tin electrode. *J. Power Sources* **2014,** *253*, 276-281.

160. Sarfraz, S.; Garcia-Esparza, A. T.; Jedidi, A.; Cavallo, L.; Takanabe, K., Cu–Sn Bimetallic Catalyst for Selective Aqueous Electroreduction of CO_2 to CO. *ACS Catal.* **2016,** *6* (5), 2842-2851.
161. Zhao, Y.; Wang, C.; Wallace, G. G., Tin nanoparticles decorated copper oxide nanowires for selective electrochemical reduction of aqueous CO_2 to CO. *J. Mater. Chem. A* **2016,** *4* (27), 10710-10718.
162. Morimoto, M.; Takatsuji, Y.; Yamasaki, R.; Hashimoto, H.; Nakata, I.; Sakakura, T.; Haruyama, T., Electrodeposited Cu-Sn Alloy for Electrochemical CO_2 Reduction to CO/$HCOO^-$. *Electrocatalysis* **2018,** *9* (3), 323-332.
163. Hou, X.; Cai, Y.; Zhang, D.; Li, L.; Zhang, X.;Zhu, Z.; Peng, L.; Liu, Y.; Qiao, J., 3D core–shell porous-structured Cu@Sn hybrid electrodes with unprecedented selective CO_2-into-formate electroreduction achieving 100%. *J. Mater. Chem. A* **2019,** *7* (7), 3197-3205.
164. Ju, W.; Zeng, J.; Bejtka, K.; Ma, H.; Rentsch, D.; Castellino, M.; Sacco, A.; Pirri, C. F.; Battaglia, C., Sn-Decorated Cu for Selective Electrochemical CO_2 to CO Conversion: Precision Architecture beyond Composition Design. *ACS Appl. Energy Mater.* **2019,** *2* (1), 867-872.
165. Rabiee, H.; Zhang, X.; Ge, L.; Hu, S.; Li, M.; Smart, S.; Zhu, Z.; Yuan, Z., Tuning the Product Selectivity of the Cu Hollow Fiber Gas Diffusion Electrode for Efficient CO_2 Reduction to Formate by Controlled Surface Sn Electrodeposition. *ACS Appl. Mater. Interfaces* **2020,** *12* (19), 21670-21681.
166. Dong, W. J.; Lim, J. W.; Hong, D. M.; Park, J. Y.; Cho, W. S.; Baek, S.; Yoo, C. J.; Kim, W.; Lee, J. L., Evidence of Local Corrosion of Bimetallic Cu–Sn Catalysts and Its Effects on the Selectivity of Electrochemical CO_2 Reduction. *ACS Appl. Energy Mater.* **2020,** *3* (11), 10568-10577.
167. Wang, J.; Zou, J.; Hu, X.; Ning, S.; Wang, X.; Kang, X.; Chen, S., Heterostructured intermetallic CuSn catalysts: high performance towards the electrochemical reduction of CO_2 to formate. *J. Mater. Chem. A* **2019,** *7* (48), 27514-27521.
168. Takashima, T.; Suzuki, T.; Irie, H., Electrochemical Reduction of Carbon Dioxide to Formate on Palladium-Copper Alloy Nanoparticulate Electrode. *Electrochemistry* **2019,** *87* (2), 134-138.
169. Ravel, B.; Newville, M., ATHENA, ARTEMIS, HEPHAESTUS: data analysis for X-ray absorption spectroscopy using IFEFFIT. *J. Synchrotron Radiat.* **2005,** *12* (4), 537-541.
170. Kato, S.; Iwase, K.; Harada, T.; Nakanishi, S.; Kamiya, K., Aqueous Electrochemical Partial Oxidation of Gaseous Ethylbenzene by a Ru-Modified Covalent Triazine Framework. *ACS Appl. Mater. Interfaces* **2020,** *12* (26), 29376-29382.
171. Jouny, M.; Luc, W.; Jiao, F., High-rate electroreduction of carbon monoxide to multi-carbon products. *Nat. Catal.* **2018,** *1* (10), 748-755.
172. Yamasaki, T.; Kuroda, A.; Kato, T.; Nara, J.; Koga, J.; Uda, T.; Minami, K.; Ohno, T., Multi-axis decomposition of density functional program for strong scaling up to 82,944 nodes on the K computer: Compactly folded 3D-FFT communicators in the 6D torus network. *Comput. Phys. Commun.* **2019,** *244*, 264-276.

173. Cheng, M. J.; Kwon, Y.; Head-Gordon, M.; Bell, A. T., Tailoring Metal-Porphyrin-Like Active Sites on Graphene to Improve the Efficiency and Selectivity of Electrochemical CO_2 Reduction. *J. Phys. Chem. C* **2015,** *119* (37), 21345-21352.
174. Mistry, H.; Reske, R.; Zeng, Z.; Zhao, Z. J.; Greeley, J.; Strasser, P.; Cuenya, B. R., Exceptional Size-Dependent Activity Enhancement in the Electroreduction of CO_2 over Au Nanoparticles. *J. Am. Chem. Soc.* **2014,** *136* (47), 16473-16476.
175. Yuan, L.; Yin, Q.; Wang, Y.; Zhou, G., CuO reduction induced formation of CuO/Cu_2O hybrid oxides. *Chem. Phys. Lett.* **2013,** *590*, 92-96.
176. Ghodselahi, T.; Vesaghi, M. A.; Shafiekhani, A.; Baghizadeh, A.; Lameii, M., XPS study of the Cu@Cu_2O core-shell nanoparticles. *Appl. Surf. Sci.* **2008,** *255* (5, Part 2), 2730-2734.
177. Cho, J. S.; Kang, Y. C., Nanofibers Comprising Yolk–Shell Sn@void@SnO/SnO_2 and Hollow SnO/SnO_2 and SnO_2 Nanospheres via the Kirkendall Diffusion Effect and Their Electrochemical Properties. *Small* **2015,** *11* (36), 4673-4681.
178. Park, J. W.; Park, C. M., A Fundamental Understanding of Li Insertion/Extraction Behaviors in SnO and SnO_2. *J. Electrochem. Soc.* **2015,** *162* (14), A2811-A2816.
179. Zhang, B.; Yu, Y.; Huang, Z.; He, Y. B.; Jang, D.; Yoon, W. S.; Mai, Y. W.; Kang, F.; Kim, J. K., Exceptional electrochemical performance of freestanding electrospun carbon nanofiber anodes containing ultrafine SnO_x particles. *Energy Environ. Sci.* **2012,** *5* (12), 9895-9902.
180. Hammond, C.; Padovan, D.; Al-Nayili, A.; Wells, P. P.; Gibson, E. K.; Dimitratos, N., Identification of Active and Spectator Sn Sites in Sn-β Following Solid-State Stannation, and Consequences for Lewis Acid Catalysis. *ChemCatChem* **2015,** *7* (20), 3322-3331.
181. Feng, Y.;Li, W.; Meng, M.; Yin, H.; Mi, J., Mesoporous Sn(IV) doping MCM-41 supported Pd nanoparticles for enhanced selective catalytic oxidation of 1,2-propanediol to pyruvic acid. *Appl. Catal., B* **2019,** *253*, 111-120.
182. Gu, Q.; Long, J.; Zhou, Y.; Yuan, R.; Lin, H.; Wang, X., Single-site tin-grafted anatase TiO_2 for photocatalytic hydrogen production: Toward understanding the nature of interfacial molecular junctions formed in semiconducting composite photocatalysts. *J. Catal.* **2012,** *289*, 88-99.
183. Lee, S. H.; Lin, J. C.; Farmand, M.; Landers, A. T.; Feaster, J. T.; Avilés Acosta, J. E.; Beeman, J. W.; Ye, Y.; Yano, J.; Mehta, A.; Davis, R. C.; Jaramillo, T. F.; Hahn, C.; Drisdell, W. S., Oxidation State and Surface Reconstruction of Cu under CO_2 Reduction Conditions from In Situ X-ray Characterization. *J. Am. Chem. Soc.* **2021,** *143* (2), 588-592.
184. Lee, S. Y.; Jung, H.; Kim, N.-K.; Oh, H.-S.; Min, B. K.; Hwang, Y. J., Mixed Copper States in Anodized Cu Electrocatalyst for Stable and Selective Ethylene Production from CO_2 Reduction. *J. Am. Chem. Soc.* **2018,** *140* (28), 8681-8689.
185. Kumar, B.; Atla, V.; Brian, J. P.; Kumari, S.; Nguyen, T. Q.; Sunkara, M.; Spurgeon, J. M., Reduced SnO_2 Porous Nanowires with a High Density of Grain Boundaries as Catalysts for Efficient Electrochemical CO_2-into-HCOOH Conversion. *Angew. Chem. Int. Ed.* **2017,** *56* (13), 3645-3649.

186. Zhang, R.; Lv, W.; Lei, L., Role of the oxide layer on Sn electrode in electrochemical reduction of CO_2 to formate. *Appl. Surf. Sci.* **2015,** *356*, 24-29.
187. Martirez, J. M. P.; Carter, E. A., Thermodynamic Constraints in Using AuM (M = Fe, Co, Ni, and Mo) Alloys as N_2 Dissociation Catalysts: Functionalizing a Plasmon-Active Metal. *ACS Nano* **2016,** *10* (2), 2940-2949.
188. Li, J.; Pršlja, P.; Shinagawa, T.; Martín Fernández, A. J.; Krumeich, F.; Artyushkova, K.; Atanassov, P.; Zitolo, A.; Zhou, Y.; García-Muelas, R.; López, N.; Pérez-Ramírez, J.; Jaouen, F., Volcano Trend in Electrocatalytic CO_2 Reduction Activity over Atomically Dispersed Metal Sites on Nitrogen-Doped Carbon. *ACS Catal.* **2019,** *9* (11), 10426-10439.
189. Sheng, W.; Kattel, S.; Yao, S.; Yan, B.; Liang, Z.; Hawxhurst, C. J.; Wu, Q.; Chen, J. G., Electrochemical reduction of CO_2 to synthesis gas with controlled CO/H_2 ratios. *Energy Environ. Sci.* **2017,** *10* (5), 1180-1185.
190. Back, S.; Yeom, M. S.; Jung, Y., Understanding the Effects of Au Morphology on CO_2 Electrocatalysis. *J. Phys. Chem. C* **2018,** *122* (8), 4274-4280.
191. Li, Q.; Fu, J.; Zhu, W.; Chen, Z.; Shen, B.; Wu, L.; Xi, Z.; Wang, T.; Lu, G.; Zhu, J. J.; Sun, S., Tuning Sn-Catalysis for Electrochemical Reduction of CO_2 to CO via the Core/Shell Cu/SnO_2 Structure. *J. Am. Chem. Soc.* **2017,** *139* (12), 4290-4293.
192. Ma, M.; Clark, E. L.; Therkildsen, K. T.; Dalsgaard, S.; Chorkendorff, I.; Seger, B., Insights into the carbon balance for CO_2 electroreduction on Cu using gas diffusion electrode reactor designs. *Energy Environ. Sci.* **2020,** *13* (3), 977-985.
193. Del Castillo, A.; Alvarez-Guerra, M.; Solla-Gullón, J.; Sáez, A.; Montiel, V.; Irabien, A., Electrocatalytic reduction of CO_2 to formate using particulate Sn electrodes: Effect of metal loading and particle size. *Appl. Energy* **2015,** *157*, 165-173.
194. Qin, B.; Li, Y.; Fu, H.; Wang, H.; Chen, S.; Liu, Z.; Peng, F., Electrochemical Reduction of CO_2 into Tunable Syngas Production by Regulating the Crystal Facets of Earth-Abundant Zn Catalyst. *ACS Appl. Mater. Interfaces* **2018,** *10* (24), 20530-20539.
195. Xie, H.; Wang, T.; Liang, J.; Li, Q.; Sun, S., Cu-based nanocatalysts for electrochemical reduction of CO_2. *Nano Today* **2018,** *21*, 41-54.
196. He, J.; Johnson, N. J. J.; Huang, A.; Berlinguette, C. P., Electrocatalytic Alloys for CO_2 Reduction. *ChemSusChem* **2018,** *11* (1), 48-57.
197. Zhi, X.; Jiao, Y.; Zheng, Y.; Vasileff, A.; Qiao, S. Z., Selectivity roadmap for electrochemical CO_2 reduction on copper-based alloy catalysts. *Nano Energy* **2020,** *71*, 104601.
198. Xie, J. F.; Chen, J. J.; Huang, Y. X.; Zhang, X.; Wang, W. K.; Huang, G.-X.; Yu, H. Q., Selective electrochemical CO_2 reduction on Cu-Pd heterostructure. *Appl. Catal., B* **2020,** *270*, 118864.
199. Machunda, R. L.; Lee, J.; Lee, J., Microstructural surface changes of electrodeposited Pb on gas diffusion electrode during electroreduction of gas-phase CO_2. *Surf. Interface Anal.* **2010,** *42* (6-7), 564-567.
200. Oh, S.; Park, H.; Kim, H.; Park, Y. S.; Ha, M. G.; Jang, J. H.; Kim, S. K., Fabrication of Large Area Ag Gas Diffusion Electrode via Electrodeposition for Electrochemical CO_2 Reduction. *Coatings* **2020,** *10* (4), 341.

201. Lim, J.; Kang, P. W.; Jeon, S. S.; Lee, H., Electrochemically deposited Sn catalysts with dense tips on a gas diffusion electrode for electrochemical CO_2 reduction. *J. Mater. Chem. A* **2020,** *8* (18), 9032-9038.
202. Irtem, E.; Andreu, T.; Parra, A.; Hernández-Alonso, M. D.; García-Rodríguez, S.; Riesco-García, J. M.; Penelas-Pérez, G.; Morante, J. R., Low-energy formate production from CO_2 electroreduction using electrodeposited tin on GDE. *J. Mater. Chem. A* **2016,** *4* (35), 13582-13588.
203. Sen, S.; Skinn, B.; Hall, T.; Inman, M.; Taylor, E. J.; Brushett, F. R., Pulsed Electrodeposition of Tin Electrocatalysts onto Gas Diffusion Layers for Carbon Dioxide Reduction to Formate. *MRS Adv.* **2016,** *2* (8), 451-458.
204. Luo, W.; Zhang, J.; Züttel, A., Boosting CO Production in Electrocatalytic CO_2 Reduction on Highly Porous Zn catalysts. *ACS Catal.* **2019**, 9(5), 3783-3791.
205. Lamaison, S.; Wakerley, D.; Blanchard, J.; Montero, D.; Rousse, G.; Mercier, D.; Marcus, P.; Taverna, D.; Giaume, D.; Mougel, V.; Fontecave, M., High-Current-Density CO_2-to-CO Electroreduction on Ag-Alloyed Zn Dendrites at Elevated Pressure. *Joule* **2020,** *4* (2), 395-406.
206. Kim, S.; Dong, W. J.; Gim, S.; Sohn, W.; Park, J. Y.; Yoo, C. J.; Jang, H. W.; Lee, J. L., Shape-controlled bismuth nanoflakes as highly selective catalysts for electrochemical carbon dioxide reduction to formate. *Nano Energy* **2017,** *39*, 44-52.
207. Jiang, X.; Cai, F.; Gao, D.; Dong, J.; Miao, S.; Wang, G.; Bao, X., Electrocatalytic reduction of carbon dioxide over reduced nanoporous zinc oxide. *Electrochem. Commun.* **2016,** *68*, 67-70.
208. Luo, W.; Zhang, Q.; Zhang, J.; Moioli, E.; Zhao, K.; Züttel, A., Electrochemical reconstruction of ZnO for selective reduction of CO_2 to CO. *Appl. Catal., B* **2020,** *273*, 119060.
209. Yavuz, A.; Hacıibrahimoğlu, M. Y.; Bedir, M., Passivation of Cu–Zn alloy on low carbon steel electrodeposited from a pyrophosphate medium. *Mater. Res. Express* **2018,** *5* (1), 016401.
210. Senna, L. F. d.; Díaz, S. L.; Sathler, L., Hardness analysis and morphological characterization of copper-zinc alloys produced in pyrophosphate-based electrolytes. *Mater. Res.* **2005,** *8* (3), 275-279.

List of publication

1. Y. Wu, K. Kaimya*, T. Hashimoto, R. Sugimoto, T. Harada, K. Fujii, S. Nakanishi*, "Electrochemical CO_2 reduction using gas diffusion electrode loading Ni-doped covalent triazine framework in acidic electrolytes", *Electrochemistry*, **88**, 359-364 (2020).

2. Y. Wu†, K. Iwase†, T. Harada, S. Nakanishi*, K. Kamiya*, "Sn atom on Cu nanoparticles for suppressing competitive H_2 evolution in CO_2 electrolysis", *ACS Appl. Nano Mater*., doi.org/10.1021/acsanm.1c00514.

Manuscript in preparation

3. Y. Wu, T. Harada, S. Nakanishi*, K. Kamiya*, "Structural modulation of metallic catalysts via direct electrodeposition on gas diffusion electrode for CO_2 electrolysis", in preparation.

Acknowledgement

At first, I'd like to thanks the China Scholarship Council and Monbukagakusho (the Japanese Government Scholarship) for supporting my study and life in Japan. This work was conducted at Research Center for Solar Energy Chemistry, Osaka University. I am so grateful for my supervisor, Prof. Shuji Nakanishi from Osaka University, from the initial decision of accepting me as a doctoral candidate in my despairing time, to the endless help during these four years. I'd also like to thank Prof. Kazuhide Kamiya and Dr. Takashi Harada, for their numerous help in experimental design, details and characterization side. Without their help, I cannot complete the complex experiments and analysis, as well as Dr. Kazuyuki Iwase, for him help from the initial introduction of background in this lab to the advice and collaborative work of paper. And all the members of Nakanishi lab, as a foreign student, and in some cases, the only foreign member, without your kindness, I cannot enjoy my four years' life in Japan.

And of course, I want to thank my parents for their support without expecting any return, maybe you still cannot understand my choice at all. As the only child, the pressure I felt is not the requirement of being an excellent person, but more communication with you, which I am not good at. And I always think about the problem whether is my unruly induce our one family into three people. Anyway, all of us need to accept current situation. Maybe I will still on my way alone, your guys also need to enjoy your own life.

There are numerous people I need to thank, and I am so grateful that people I met are so friendly and helpful. With my typing, I heard the knock from my keyboard at a silent night, and remind me the last sentence I wrote in my master thesis, ‘although there is a tough journey in front of, I need to have a try’ and the faith to future. Now, I also need to find my courage to face the following life.

WU YUXIN

September, 2021